Chemo-mechanical Coupling in Nanoporous Palladium-hydrogen

Vom Promotionsausschuss der
Technischen Universität Hamburg
zur Erlangung des akademischen Grades
Doktor-Ingenieurin (Dr.-Ing.)
genehmigte Dissertation

von
Shan Shi

aus
Kaifeng, China

2019

Erstgutachter: Prof. Dr.-Ing. Jörg Weissmüller, Technische Universität Hamburg

Zweitgutachter: Prof. Dr.rer.nat. Roland Würschum, Technische Universität Graz

Vorsitzender: Prof. Dr.-Ing. Otto von Estorff, Technische Universität Hamburg

Tag der mündlichen Prüfung: February 21, 2019

Abstract

This thesis establishes the synthesis of monolithic and uniform nanoporous palladium via a single-step electrochemical dealloying of copper-palladium alloys in sulfuric acid solution. The dealloying procedure produces a hierarchical network structure with two well-defined ligament sizes. An annealing treatment on the hierarchical nanoporous palladium material leads to a classic, monomodal pore- and ligament size distribution. Mechanical responses of hierarchical nanoporous palladium through electrochemically controlled hydrogen sorption are explored. In-situ dilatometry is used to evaluate hydrogen absorption/desorption induced expansion/contraction in nanoporous palladium; in-situ dynamic mechanical analysis is used to measure open-system effective elasticity of nanoporous palladium-hydrogen. It is observed that hydrogen electrosorption in nanoporous palladium results in (1) large reversible strain variations (up to 4%), which are stable for more than 1000 cycles, and (2) large elasticity variations (more than 30% increase in compliance). With respect to these chemo-mechanical coupling in nanoporous palladium-hydrogen, discussions on hydrogen sorption isotherms and composition-strain coupling coefficients demonstrate that the behavior of nanoporous palladium-hydrogen can be quantitatively understood in terms of the established behavior of non-porous palladium-based hydrides and of hydrogen underpotential deposition on planar palladium surfaces. Moreover, the experimentally measured open-system effective elastic parameters of nanoporous palladium-hydrogen are compared to the prediction by Larché-Cahn elasticity theory. The excellent agreement between experiment and prediction gives the most direct verification of Larché-Cahn theory, which theory is regarded as one significant advance in thermodynamics of the 20th century. Overall, in this thesis, a novel strategy is established for fabricating uniform nanoporous palladium, as an alternative to nanoporous gold. The electrochemically tunable mechanical properties of nanoporous palladium-hydrogen enable it as a promising actuation material and as a probe for studying chemo-mechanical coupling.

Acknowledgments

I would like to thank all the people who help, support and encourage me during my PhD studies. Although I might not directly express my gratitude to you in the daily life, what we experienced together and your help as well as your care are deeply in my heart.

First of all, I would like to sincerely thank my supervisor, Prof. Jörg Weissmüller. I am very fortunate to have such an excellent supervisor who loves and is good at imparting knowledge. His patience and trust in me often touched me. His love of scientific research deeply infected me. The discussions with him have taught me a lot and prompted me to supplement my knowledge more effectively afterwards. He taught me how to be a good scientist step by step such as scientific writing, international presentation and so on. He is not only like a bright light that guides me forward but also like a father: gentle, amiable and considerate for the future of the child.

Next, I want to express my great acknowledgements to my unofficial supervisor, Dr. Jürgen Markman. At the beginning of my PhD study and my life in Germany, his great care, detailed introduction and explanation help me adapt to the new environment. His help, care and supports accompany my progress or growth during the whole PhD period. Whenever I meet problems and difficulties from small things in life to scientific researches, he is always ready to help me solve them.

My specical thanks goes to the second reviewer for my thesis, Prof. Roland Würschum from Graz University of Technology. His support helps me complete my doctral examination and his valuable suggestions help me improve my thesis. Additionally, I would like to express my acknowledgements to my colleagues at the Helmholtz-Zentrum Geesthacht and the Institute of Materials Physics and Technology at Hamburg University of Technology. To Tobias Kitzer, Mameka Nadiia, Nam Ngo, Ilya Okulov, Rainer Behn, Zhen Qi, Qibo Deng, Charlotte Kuss, Lukas Lührs, Mark Busch, Benedikt Roschning, Birthe Zandersons, Xinyan Wu, Jie Li, Yijuan Wu, Kaixiong Hu and Ke Wang, thank you for the help during experimental work and/or scientific discussions. I am also thankful to Junjun Shen, Martin Ritter, Jens Timmermann and Farhad Riazi for the instruction and help with the SEM studies, Tobias Krekeler with the TEM measurement as well as Stephanie Koch, Haide Alfort-Springer and Robert Günther with official matters.

Finally, I want to thank my friends and my family. To my close friends in Germany, Anne Schnier, Nadiia Mameka, Oleg Tokariev, Yufen Zhang, Fei Teng, Jiachun Chen, Yiyi Lu, Yan Chen, Xinyan Wu and Peng Xu, you are like my family in Germany. You were always there for me and provided strength to get me through the tough times. I cherish the times and experiences very much. To my parents, thank you for giving me a warm harbor and encouraging me to study abroad and do what I like. To my dear husband, who endured near 4 years of a stressed wife, thanks for always accompanying me, supporting me and encouraging me to not give up.

Contents

List of Figures

Chapter 1

Introduction

1.1 Motivation and background

Nanoporous metals gain growing interests in both fundamental materials science and engineering applications. Considerable efforts have been devoted to the synthesis, structure control, characterization, and application performance improvements. Nanoporous metals can be fabricated into nanoparticles, thin films, foils, wires and monolithic samples. Many nanoporous metals (such as gold, palladium, platinum, silver, copper, aluminum and nickel) have already been fabricated. In the past decade, researchers have shown an increased interest in monolithic nanoporous metals. Monolithic nanoporous metals with structure sizes ranging from 5 to 500 nm have a significantly larger surface-to-volume ratio compared with non-porous metals. The large ratio of surface atoms makes them possess tunable mechanical properties by controlling the surface or interface states. However, the monolithic nanoporous metals which are suitable for nanomechanics studies are still limited to nanoporous gold and gold-based materials. Therefore, it is interesting and important to synthesize a new kind of monolithic nanoporous metal which has a uniform microstructure, an excellent homogeneity and good mechanical behaviors, providing an alternative to nanoporous gold. Palladium, as a model material for hydrogen storage study, is chosen. The hydrogen-storage properties may provide nanoporous palladium many opportunities for functionalization and studying some scientific questions that are difficult to solve by using non-porous metals. This thesis focuses on the interesting chemo-mechanical coupling in nanoporous palladium-hydrogen. For instance, the ultilizations of nanoporous palladium as an actuation material and as a model system for verifying Larché-Cahn elasticity theory are explored. The detailed motivation and background for synthesizing nanoporous palladium and studying chemo-mechanical coupling in nanoporous palladium-hydrogen are given in the following sections.

1.1.1 Dealloying-made nanoporous metals

Dealloying is the selective dissolution of one or more elements from an alloy. [1–3]. Nanoporous (np) metals made by chemical or electrochemical dealloying often show bicontinuous porous structures, large surface-to-volume ratios and tunabe ligament/pore sizes [3–9]. The ligament/pore sizes of nanoporous metals can be tuned from a few nanometers to several hundreds nanometers via a variety of approaches such as adjusting dealloying conditions (such as dealloying potential [10, 11], electrolyte [12] and temperature [13]), and imposing post chemical or electrochemical treatments [14–16] and thermo-annealing [14, 16–21]). For instance, Liu *et al.* found that after imposing several potential cycles (named as electrochemical reduction) on as-dealloyed nanoporous gold (np-Au), the ligament size changes from 15 nm to 45 nm (Figures 1.1a-b) [16]. Moreover, when the same kind of as-dealloyed samples were annealed for 10 min at temperatures from 200 °C to 500 °C, the ligament size became much coarser, from 54 to 548 nm, as shown in Figures 1.1c-f.

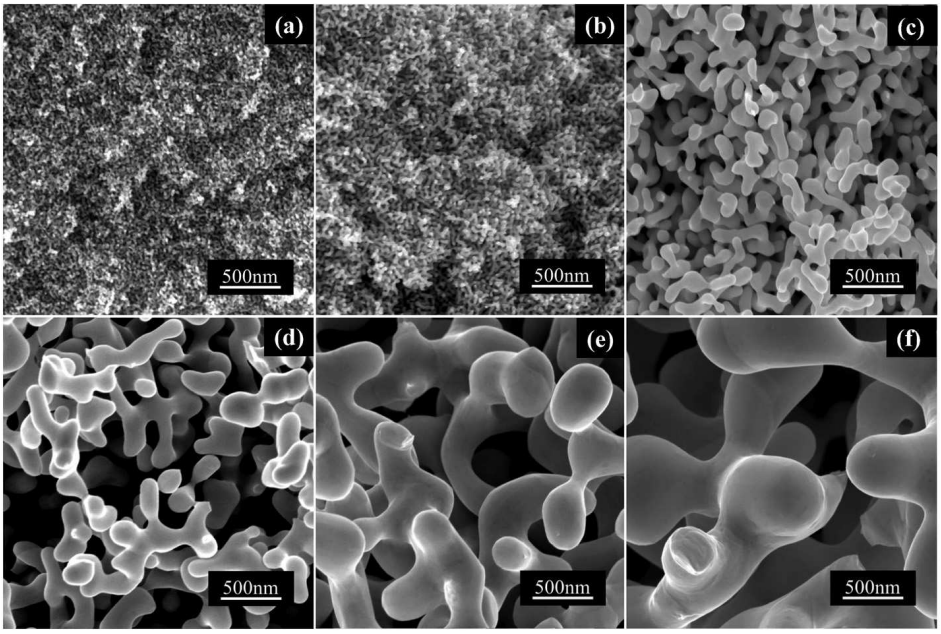

Figure 1.1: SEM images of nanoporous gold (a) at as-dealloyed state, (b) after electrochemically reduction, and after annealing at temperatures of (c) 200 °C, (d) 300 °C, (e) 400 °C, and (f) 500 °C. Reprinted with permission from Ref [16].

Except for above mentioned classic np metal which has one well-defined ligament/pore size, np metal which has a multi-level ligament/pore size distribution (named as hierarchical np metal) also attracts great interests. Recently, a wide range of hierarchical np metals including gold [22–24], platinum [25], palladium [26–28], copper [29], and nickel [30] have already been synthesized. It is known that unimodal np metals are mostly synthesized by single-step dealloying of single-phase alloys, but hierarchical np metals are often synthesized through "single-step dealloying multi-phase alloys" or "multi-step dealloying single-phase alloys" approaches [27, 28, 30, 31], as briefly illustrated in Figure 1.2.

By dealloying-coarsening-dealloying of an $Ag_{90}Au_{10}$ alloy, Qi *et al.* synthesized uniform hierarchical nanoporous gold with two well-defined ligament sizes (Figure 1.3) [23]. However, the multi-step synthesis process is complex and time-consuming. By contrast, the "single-step dealloying multi-phase alloy" method is much more facile, but it often leads to inhomogeneous pores and poor mechanical properties especially in thick samples. This drawback is mainly caused by upper-level pores, which are derived by dissolution of active phase from a precursor alloy. The active phase is formed during solidification processes, therefore, their morphologies like shape and size distributions are difficult to control. For example, Zhang *et al.* synthesized hierarchical nanoporous palladium (np-Pd) via a free corrosion of $Al_{80}Pd_{20}$ (Al + Al_3Pd) master alloys [28]. The preferential dissolution of the active Al phase lead to non-uniform, large pores at the upper hierarchy level and even cracks.

Dealloying-made nanoporous metals, as a class of nanostructured metals, have drawn great attentions in various applications such as catalysis [9, 33–35], sensing [7, 17, 31, 36–38], actuation [28, 39–43], energy storage [9], bioanalytical and biomedical applications [7]. Especially, the hierarchical nanoporous metals have not only large specific surface areas for functionalization but also large transport pathways for fast responses, showing even superior potentials [23, 25, 26, 28, 44]. For instance, hierarchical nanoporous gold bulk samples synthesized by Qi *et al.* have pore sizes of ~ 200 and ~15 nm, showing a faster charge transport rate than unimodal nanoporous gold [23]. Substantially improved catalysis performances have also been observed by using hierarchical nanoporous palladium with two well-defined pore sizes (50 and

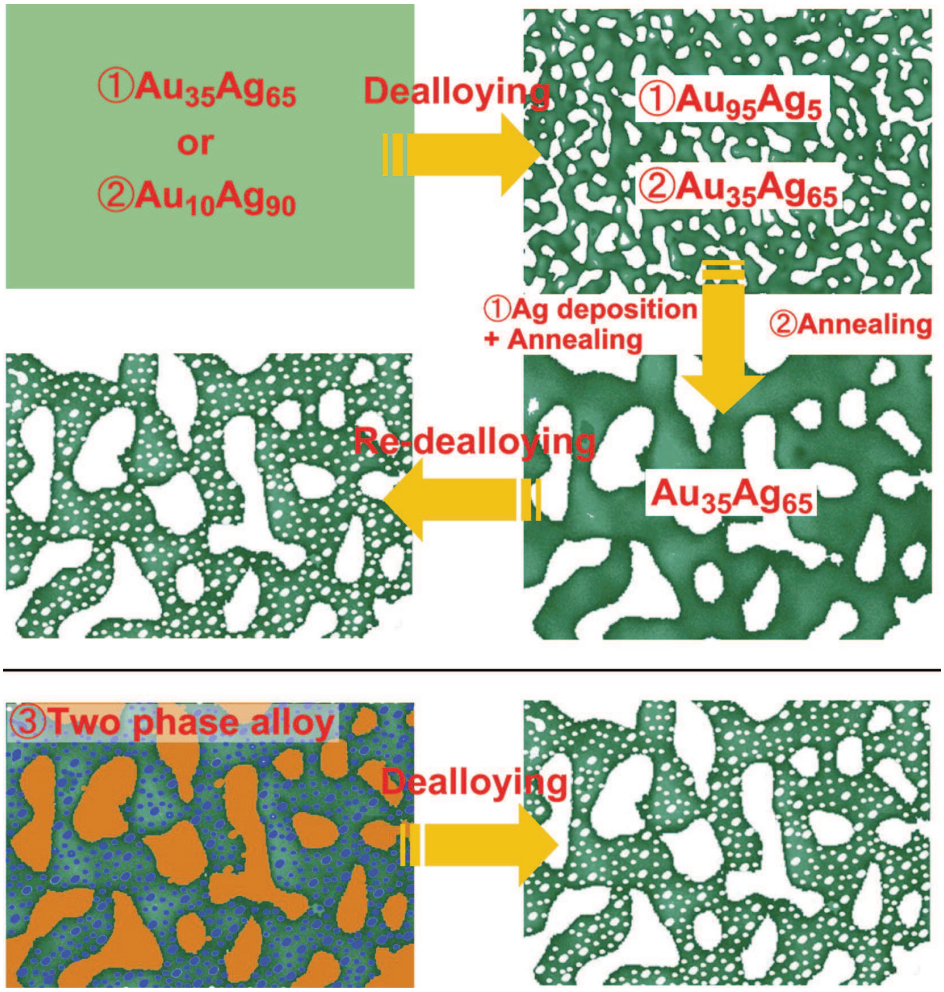

Figure 1.2: Three strategies for fabricating hierarchical nanoporous metals. The scheme is adopted from Ref [32].

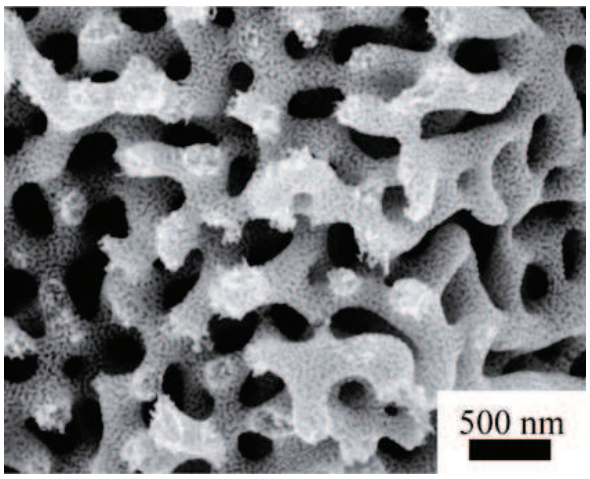

Figure 1.3: Scanning electron micrographs of hierarchical nanoporous gold fabricated out of $Ag_{90}Au_{10}$ via a dealloying (-coarsening)-dealloying method. Reprinted with permission from Ref [23].

10 nm) [22].

Another character of nanoporous metals distinguished from other nanostructured materials is that nanoporous metals can be fabricated in monolithic bodies with dimensions in the range of millimeter or centimeter scale. [45–50]. Apart from the advantages mentioned above, monolithic nanoporous metals show high structural and mechanical stabilities. These advantage enable nanoporous metals being model systems in studying the influences of ligament size and interface state on materials mechanical properties by using conventional macroscale mechanical tests [5, 6, 51–53]. For instance, conventional compression and tension tests have already been carried out on monolithic nanoporous gold to explore the influences of ligament size or surface state on mechanical behaviors [5, 6, 51, 52]. Certainly, the understanding and controlling of mechanical properties of nanoporous metals are of great importance for their functional applications. However, monolithic nanoporous metals that are suitable for nanomechanics studies such as effects of ligament size, solid fraction and connectivity are highly restricted to nanoporous gold and gold-based materials. Liquid metal dealloying has recently developed as an efficient strategy for preparing various porous metals (such as titanium, niobium and stainless steel) [8, 54–56]. However, porous metals synthesized by this method often have larger ligament/pore sizes in the range of a few to several hundreds of micrometers and smaller surface-to-volume ratio in comparison with np metals derived from chemical/electrochemical dealloying in electrolyte. Very recently, another two new routes have been proposed for synthesizing high-quality bulk nanoporous materials. One is using reduction-induced decomposition of silver chloride to fabricate monolithic nanoporous silver by Wang *et al.* [57]. The other is using galvanic replacement reaction of Al_2Mg_3 to synthesize monolithic nanoporous aluminum by Yang *et al.* [58]. Chemical/electrochemical dealloying-made np gold and gold-based materials have remained as the most widely used model system for nanomechanics studies. Therefore, it is interesting to synthesize a new kind of monolithic nanoporous metal which has uniform microstructure, excellent homogeneity and good mechanical behaviors, providing an alternative to nanoporous gold.

1.1.2 Electrochemically driven actuators

Like natural muscle, an electrical actuator can perform reversible mechanical movements when it is triggered by an external electric signal. Electrically driven actuation materials mainly include piezoelectric, ferroelectric, and electrostrictive ceramics [59–61]. However, most of them show small strain amplitudes and high operating voltages. By contrast, electrochemically driven actuators, on the basis of dimension changes induced by reversible species electrosorption or electrons charging, show larger strain and lower operating voltages than electrical actuators. Electrochemical actuation materials mainly include ionic electroactive polymers [62–65], nanostructured carbon materials [66, 67], and nanoporous metals [40, 68, 69]. However, when bringing these materials into practical applications, for example imitating the performance of natural muscles, there are still many challenges. Ions moving in/out of ionic electroactive polymers can lead to large expansion/contraction, but most ionic electroactive polymer actuators have limited lifetime and weak mechanical properties [65]. By contrast, carbon nanomaterials and np metals utilize charge-injection (double-layer charging or surface adsorption/desorption during capacitive or pseudocapacitive processes) induced surface stress to initiate actuation. These materials show significant improvements in aspects of stability, response time and mechanical performance. However, their strain strongly depends on the specific capacitance which is related to the specific surface area and the applied potential range. For carbon nanomaterials, a large length variation of 2% is only achieved with nanographene materials which have 100% surface atoms [67]. For np metals, Jin *et al.* found that a length variation of 0.35% within a potential window of 1.6 V is achieved in a clean np-AuPt alloy with an ultra-small ligament size of 5 nm [40]. Although this strain is much smaller than that of electroactive polymer actuators, np metals with good mechanical properties are attractive,

when considering it may operate under comparatively high stresses and thereby reach high strain energy densities [40, 68, 69].

Different from surface stress, it is known that the interstitial hydrogen (H) insertion in metals or alloys can lead to large lattice strain changes [70]. For example, hydrogen insertion in palladium at room temperature can lead to more than 3% lattice expansion [71]. It has been demonstrated that the lattice or volume expansion of Pd rises linearly with hydrogen fraction (x_{H}, expressed as the molar ratio of hydrogen to metal) in a wide x_{H} range (up to 0.7 at room temperature) [72–74]. This behavior has ever been used as an actuation mechanism in Pd-based thin films and foils for bending movements [70, 75], but these actuators often show a poor reversibility or mechanical stability due to misfit-strains at the developing interfaces during hydrogen loading or hydrogen embrittlement effects.

In 2017, large-stroke, H-assisted actuation with np-Pd materials were realized by Zhang and Steyskal [28, 76, 77]. Zhang *et al.* synthesized bulk np-Pd by free corrosion of two-phase ($PdAl_3$ + Al) alloys in nitric acids [28]. Because the active Al phase formed during solidification often has uncontrollable shape and size distributions, corrosion of the Al phase produces non-uniform pores and even causes cracks. This drawback most probably will influence the mechanical properties of np-Pd and then affect its actuation performances especially when working under stresses. Steyskal *et al.* avoid this drawback by using uniform and homogeneous np-Pd that is synthesized by dealloying a single-phase Pd-Co alloy [77]. This method is firstly reported by Hakamada *et al.* [78, 79]. The homogeneous np-Pd prepared with Hakamada's method is very promising to have better mechanical stabilities compared with the former one, but this speculation has not been demonstrated yet. Actuation behavior of monolithic np-Pd samples with not only homogeneous pore structures but also good mechanical properties remains to be explored.

Hydrogen absorption can be achieved via exposing Pd in a gaseous hydrogen atmosphere with a given pressure or via electrochemically charging Pd electrodes in hydrogen-contain electrolytes with a given potential [80]. At room temperature, Pd-H alloys are known to exist in H-diluted α-Pd-H phase (an interstitial solid solution, $x_{\mathrm{H}} \leq 0.02$), H-concentrated α'-Pd-H phase (a Pd hydride, $x_{\mathrm{H}} \geq 0.6$) and in-between coexisted $\alpha + \alpha'$ mixtures [73]. It is obvious that Pd must go through the $\alpha \leftrightarrow \alpha'$ phase transition in order to achieve large lattice strain variations. Because α-Pd-H phase and α'-Pd-H phase have substantially different lattice parameters, many times of phase transition most probably will cause accumulation of lattice defects and materials' degradation. This speculation has previously been demonstrated with film-type Pd-H actuators, in which poor reversibilities and cracks are observed after a cycling test [75]. Therefore, it remains to probe whether the utilization of high-quality, robust and monolithic nanoporous-palladium may show a difference.

1.1.3 Larché-Cahn open-system elasticity

The interplay between chemistry and mechanics is a very common phenomenon, and the understanding of this interplay can be very crucial for both fundamental materials science and engineering applications. Coupling relationships between stress and a wide range of chemical behaviors (solute solubility, diffusion, chemical potential, phase transition, microstructural instability, catalysis) have been examined and discussed by many researchers [81–84]. Recently, electro-chemo-mechanical coupling, as a branch of chemo-mechanical coupling, also draws great interests due to the developments of in-situ techniques. For instance, the stress-potential coupling in lithiated silicon particles and gold thin films [81, 85], the alteration of electrocatalytic performance by elastically straining host lattices [86–89], and the strain-concentration coupling during hydrogen electrosorption in nanoporous palladium [28, 42, 77, 90] have already been investigated.

One well-known and old example with respect to the interaction between stress and solute solubility is the diffusionless martensite transformation, during which process local chemi-

cal composition is generally regarded invariable but crystal lattice parameters change. This transformation can lead to mechanically elastic distortion of crystal lattice and enhancement of interstitial solubility in hardening steel. For example, in iron-carbon alloys [91], during quenching or rapid cooling, carbon in face-centered cubic austenite is short of time for diffusion or redistribution, resulting in distorted body-centered tetragonal martensite with supersaturated carbon interstitials, therefore leading to enhanced strength and hardness.

The interaction between elastic stress and diffusion has been reported to affect the formation and structure evolution of precipitates in superalloys, making them own good mechanical properties at high-temperature conditions and be good turbine blade or aerospace structural materials [92–94]. For example in nickel-based superalloys, at the beginning of phase separation, the interface free energy between two phases works as the driving force for the diffusion of alloying elements and for precipitate coarsening. With time going on, the elastic strain arises from misfit lattice between the two phases becomes dominant driving force, affecting precipitate size and morphology. Finally, nickel-based superalloy separates into two phases: disordered γ solid solution and and L12-ordered $\gamma\prime$ phase. The $\gamma\prime$ precipitates coherently embed in the γ matrix.

The interaction between stress and diffusion has attracted many interests in energy storage applications such as hydrogen storage in metals and lithium ion batteries. It has been demonstrated that electrochemical insertion of Li or H can lead to host lattice expansion, for example Li insertion can induce up to 300% volume expansion in silicon and H insertion can induce more than 4% lattice expansion in palladium. It has been observed that inhomogeneous distribution of solutes in electrode materials can lead to misfit strain and stress fields, and the stress fields in turn can affect the diffusion and redistribution of solutes [95–98]. This interaction is very crucial for materials' long-term cycling performances, because diffusion-induced strain or local stresses during repeated charging/discharging may lead to host materials' degradation or even deformation.

Solute redistribution in stress gradients is supposed to give rise to an elastic relaxation of solid solution. Vadim Gorsky established considerable investigations on the elastic aftereffect (named "Gorsky-effect") in metal-hydrogen alloys [99, 100]. "Gorsky effect" were explored in torsion experiments with Nb-H springs by Alefeld and Völkl *et al.* [101, 102]. Their experiments suggest that an immediate elastic response to stress jumps is followed by a slow elastic relaxation which brings additional strain that can be reverted when the stress is released. These authors also found that the extra strain from solute redistribution can become very large near the critical point of the miscibility gap. Yet, later studies in the context focused on hydrogen diffusion. The Gorsky-effect measurements are mainly used to determine hydrogen diffusion coefficients from elastic relaxation time [96, 103].

It is found that most chemo-elastic coupling phenomena have been well-documented and particularly explained by specific theories, however, there is still no general or unified theory before the middle of 20th century. It was only until 1973, Francis Larché and John W Cahn established a unified theory by combining solid mechanics and alloy thermochemistry [104]. One central conclusion in the Larché-Cahn theory is that under the assumption of relatively small strain and compositional variations, the conventional closed-system elastic coefficients at fixed composition should be replaced with new open-system elastic constants at constant chemical potential. The open-system elastic constants are very strongly concentration-dependent, because they are related to the interplay of solute concentration and stress at equilibrium. In 2015, Mishin computed both open-system and closed-system elastic coefficients of Al-Ni alloys at 700 K by atomic simulation (semigrand canonical Monte Carlo simulation in combined with shape fluctuation approach) [105]. He focused on Al-Ni alloys with a narrow composition range from 0 to 13.5 atomic percent (at%) Al and observed large differences between open system and closed system in the elastic constants C_{11} and C_{12}. The difference in C_{12} is up to 15% for Al-Ni alloys containing 6 at% Al. His study also predicted that near critical phase

transition points, the variation of elasticity may encompass several orders of magnitude.

A variety of studies in favor of Larché-Cahn theory have been established via theory deduction or numerical modeling on the topic of phase transformation [105–111]. Larché-Cahn theory is also very crucial for the hanging controversial opinions regarding solute-dislocation interaction: the solute-enrichment around dislocation (Cottrell atmosphere) versus solute-induced screening of dislocations (stress-shielding effect) [105, 112–115]. However, so far, there is no direct experimental evidence to prove Larché-Cahn theory. Verifying Larché-Cahn theory from the experimental aspect is certainly essential in advancing its application. Hence, it is remarkably interesting to exploit proper materials and mechanical testing methods, exterminating the key conclusion in Larché-Cahn theory: open-system elastic coefficients.

1.2 Outline of thesis

A brief review on the theoretical background related to the main work of the present thesis is given in Chapter 2. The first section of Chapter 2 mainly summarizes the fundamental dealloying knowledge. The role of two parameters "parting limit" and "critical dealloying potential" in alloy corrosion is described. The development of dealloying mechanism is also briefly described. The background knowledge is very necessary and helpful for a better understanding of structure evolution of nanoporous palladium in the present thesis.

The second section of Chapter 2 focuses on the open-system elasticity theory by Larché-Cahn. It begins with an introduction of solid network concept that is proposed by Larché-Cahn. This concept is critical for subsequent description of strain and definition of open-system and closed-system elastic coefficients in diffusive solids. Followed by that, a deduction of relative compliance difference between open system and closed system in a binary interstitial solid solution is given for the use in subsequent chapters.

Chapter 3 gives the detail of experimental procedures on materials' synthesis and characterization. All setups, electrochemical techniques, and in-situ mechanical testing approaches used in present thesis are described as well.

In Chapter 4, experimental results are written in six sections. The first section focuses on the synthesis of nanoporous palladium such as dealloying parameter determination, structure evolution mechanism and structure control. In the second section, results on electrochemical characterization of nanoporous palladium in sulfuric acid are given. The remaining sections focus on the chemo-mechanical coupling behaviors in nanoporous palladium-hydrogen, such as strain-potential, strain-concentration and strain-elasticity coupling relationships. Based on those coupling relationships, results on hydrogen-assisted large-stroke actuation in nanoporous palladium, and verification of Larché-Cahn open-system elasticity theory are given.

Chapter 5 mainly discusses the underlying mechanism of hierarchical nanoporous structure evolution during dealloying, the impact of surface stress on the hydrogen solubility isotherm in nanoporous palladium, the actuation performances of nanoporous palladium-hydrogen and the experimental verification of Larché-Cahn open-system elasticity.

In Chapter 6, the main findings in the present thesis are briefly summarized. An outlook on future work is also given there.

Chapter 2

Theoretical background

2.1 Fundamentals of dealloying

Dealloying is the selective corrosion of one or more elements from an alloy [1, 2]. The selective corrosion is driven by the chemical potential difference between alloy constituents, therefore it can take place either under open circuit conditions (so-called free corrosion or chemical dealloying) or with assistance of external voltage (so-called electrochemical dealloying). Recently, dealloying is widely used to to synthesize bicontinuous nanoporous metals. For example, nanoporous gold can be fabricated by naturally dissolving silver from a silver-gold alloy in nitric acids or by selectively dissolving silver from a silver-gold alloy in perchloric acids under an electrode potential of 0.75 V (versus standard hydrogen electrode, vs SHE) [116]. In the past decades, considerable efforts have been devoted to understand the dealloying process and the underlying formation mechanism for bicontinuous nanoporous metals.

2.1.1 Parting limit

In 1919, Tammann introduce the term "parting limit" [117]. In a binary alloy, it is defined as the lower limit of the more active component fraction for the accomplishment of bulk dealloying under a specific environment. If the content of less noble component is below parting limit, selective dissolution of less noble metal will be terminated or passivated due to the enriched layer of more noble metals along the solid/electrolyte interface, no matter how large the applied potential is. Under that condition, pits or porous structures are formed only at or near the outer surface instead of throughout the entire bulk body.

Historically, many researchers have attempted to determine and explain the parting limit by means of experiments and computation. The earlier theory on the parting limit is related to the geometrical site percolation threshold of alloy lattice. This viewpoint is supported by some binary alloy systems in which the two components have a large chemical potential difference. For example, Sieradzki *et al.* found that the experimentally measured sharp parting limits in zinc-copper alloys and zinc-aluminum alloys are very close to corresponding site percolation threshold in their FCC lattices [1, 118]. When the two components in an alloy system do not have a large chemical potential difference, the experimental dealloying parting limit and the site percolation threshold can be quite different, for example in the silver-gold alloy system, the experimental dealloying parting limit is approximately 55 at% silver, but the site percolation threshold is approximately 19 at% silver.

In 1989, Sieradzki *et al.* proposed a layer-by-layer selective dissolution mechanism based on the high density percolation theory [118]. Monte Carlo simulations of dealloying including dissolution of less noble elements and diffusion of more noble elements in two-dimensional binary alloy lattices demonstrate that: (1) When the dissolution of less noble elements take place even at high coordinated sites (such as terrace), the resulting parting limit is close

to threshold observed in zinc-copper type alloys or site percolation threshold. (2) when the dissolution only occurs at relatively low coordinated sites (excluding terrace-site), the resulting parting limit is close to dealloying threshold that observed in silver-gold type alloys. Additionally, the diffusion behavior of noble metal can also affect the computed parting limit. However, this two-dimensional layer-by-layer dealloying mechanism is then believed incorrect because dealloying requires selective dissolution of less noble constituents at terrace-sites even in silver-gold type alloys. Afterwards, MESOSIM Kinetic Monte Carlo simulations, which is used by Erlebacher in describing the three dimensional pore structure evolution during dealloying, also predict the parting limit in the silver-gold system [2, 119]. Assuming dissolution of less noble elements is not allowed when coordination number of silver atom along electrolyte interface is more than nine and no surface diffusion activities of noble metals, Kinetic Monte Carlo simulations give rise to a parting limit of 58.4 at% silver for the silver-gold system, which value is very close to the experimental parting limit (55 at%) and the high-density site percolation threshold (60 at%) that obtained under the same assumption without considering the identity of binary alloys. Even taking the surface diffusion of gold atoms into account, the parting limit estimated by Kinetic Monte Carlo simulation shows no big differences.

2.1.2 Critical dealloying potential

Critical dealloying potential denotes the lowest potential for bulk dealloying. Even though the atomic fraction of more active component in a binary alloy precursor greatly exceeds parting limit, bulk dealloying still can not take place or complete if the applied potential is below critical dealloying potential.

It is generally believed that bulk dealloying process is related to the balance between selective dissolution of less noble components (surface roughening), and surface diffusion of more noble components (surface smoothing). Below the critical potential, the surface dissolution is relatively slow and surface smoothing effect is dominant, therefore, passivation will be caused by the enrichment of more noble elements at surface. Above critical potential, the dominant effect is fast dissolution induced surface roughening, which enables the underlying un-dealloyed materials to expose to electrolyte for further etching. However, the value of critical dealloying potential closely relates to the master alloys, electrolytes and temperature. For instance, the critical dealloying potential is observed to increase with the increasing content of more noble element in silver-gold master alloys [120]. Even the chemical composition of master alloys is fixed, the choice of electrolyte solutions can also significantly influence the critical dealloying potential [121].

In experiments, the critical dealloying potential is often estimated on the basis of the variation of dissolution rate with potential during bulk dealloying process via a potentiodynamic polarization strategy [121]. Figure 2.1 shows an exemplary polarization curve of a binary alloy. It can be divided into three regions: the passivation region (below critical dealloying potential), the selective dissolution region (above critical dealloying potential), and the in-between critical dealloying potential-inclusive region. In practice, bulk dealloying is usually carried out at potentials greater than the critical dealloying potential. Empirically, the critical dealloying potential is determined as the potential value at a current density of $1.0\,\mathrm{mA/cm^2}$ under the condition of a slow scan rate of $1\,\mathrm{mV/s}$, which is proposed by Sieradzki *et al.* based on their systematic investigations on selective dissolution of silver-gold alloys in $HClO_4$ solutions [121, 122]. This approach has been widely accepted in lateral studies. It is also employed in the present thesis, see Section 4.1.1.

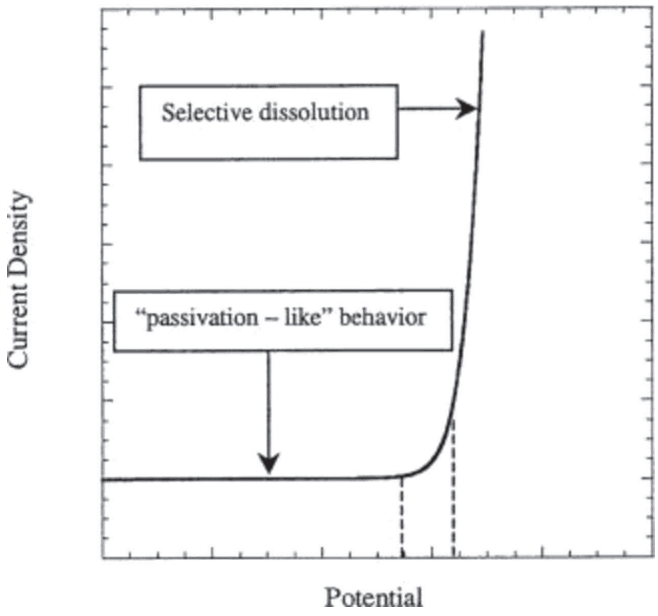

Figure 2.1: Schema of an exemplary polarization curve for one binary alloy. Reprinted with permission from Ref [121].

2.1.3 Dealloying mechanisms

The understanding of dealloying processes is crucial in the general corrosion science like stress corrosion cracking related questions and in the fabrication of nanoporous metals. In literature, various mechanisms or models have been proposed to explain the selective dissolution process of more active element from a binary alloy and/or to explain the formation of three dimensional nanoporous network, such as dissolution-redeposition mechanism [123], volume diffusion mechanism [124], surface disordering and reordering concept [125, 126], percolation theory [1], and terrace-site dissolution model [2, 127].

Dissolution-redeposition mechanism

Dissolution-redeposition mechanism was proposed in 1922 by Abrams [123]. In this mechanism, both less noble and more noble components are dissolved into electrolyte solution, but ions of more noble element in the solution can redeposit on the metal surface. This mechanism is mostly used in explaining the dezincification behavior, which is a widely known corrosion failure when brass is exposed to chloride-contain solutions. During dealloying process zinc and copper in the brass are simultaneously dissolved in the electrolyte and then copper ions (Cu^{2+}) re-precipitate at copper surface forming a sponge with poor mechanical properties. However, this mechanism shows obvious limitations when explaining the nanoporous structure evolution in more general dealloying systems. For example, in alloy systems containing much more noble elements (like gold and platinum), the generally applied potential that aims to selectively leach less noble components is often not high enough to oxidize more noble components.

Volume diffusion mechanism

Volume diffusion mechanism [128] was initially considered inoperative because of the low interdiffusivities of most metal atoms at room temperature. The possibility of this mechanism was proposed by Pickering and Wagner in 1967 with consideration of the volume diffusion

via divacancy [124]. In this mechanism, only less noble metals is dissolved and then produces excess vacancies along and underneath the alloy/electrolyte interface. The supersaturated vacancies will improve the inter-diffusivity of alloy, therefore the enhanced transport of less noble atoms from the lattice to the alloy/electrolyte interface then enables the continuous ionization and dissolution. However, the diffusivity of monovacancies is so low at room temperature that the observed high dissolution rate or current density can only be explained by the divacancy diffusion.

Surface diffusion mechanism

Surface disordering and reordering concept Surface disordering and reordering via surface diffusion was proposed by Forty and Durkin through investigating the island-channel morphologies of silver-gold alloys in nitric acids under different conditions [125]. In this model, less noble metal atoms along the alloy/electrolyte interface are preferential dissolved, leading to a disordered distribution of more noble metal adatoms and vacancies at the surface. The migration of residual noble metal adatoms tends to form islands, and therefore exposes a fresh alloy layer to acids leading to further dissolution of less noble metals, migration of noble metal atoms and growth of noble metal islands. Later on, Forty and Rowlands also used this concept to account for the formation of surface pits and corrosion tunnels in noble metal alloys [126].

Percolation concept Sieradzki *et al.* developed the surface diffusion mechanism by incorporating percolation theory [1]. Monte Carlo simulations of selective dissolution in binary alloy systems without considering the nature of alloy and electrolyte was performed on a lattice that is randomly filled with two elements.The simulation assumes the dissolution of less noble metal atoms and the surface diffusion of more noble metal atoms take place layer-by-layer as the number of their nearest neighbours reaches a specified valve. This type of computation gives consistent results with experimental observations in the aspect of sharp dealloying threshold (parting limit), formation of porous structure, and coarsening phenomena. Yet, some aspects like critical dealloying potential and dissolution of terrace-site atoms were not well-solved at that moment.

Terrace-site dissolution model In 2001, Erlebacher proposed a significantly advanced model which considers the dissolution of high-coordinated terrace-site atoms and the formation of terrace vacancies [2, 127]. Modified kinetic Monte Carlo code is used to simulate both dynamical nanoporous morphology evolution process and kinetic dissolution behaviors of one defined silver-gold alloy system. The simulation results agree very well with experimental dealloying observations in the aspect of three-dimensional nanoporous microstructure, critical dealloying potential, and length scale between ligaments.

The main idea of this model is briefly illustrated in Figure 2.2. As the applied electrochemical potentials is above critical dealloying potential, dealloying process starts with the dissolution of silver atoms from low-coordinated sites (step edge) and then from high-coordinated sites (terrace), as shown in Figure 2.2a. The formation of terrace vacancies is supposed to be rate-limiting step. The gold adatoms left behind tend to agglomerate into clusters or islands due to the rapid surface diffusion behavior of noble gold atoms along the solid/electrolyte interface. Remarkably, the dissolution of terrace-site silver atoms will produce terrace vacancies and terrace vacancy clusters (Figure 2.2b), which then leads to generation of new low-coordinated silver atoms neighboring these terrace vacancies and then the dissolution of these silver atoms. As long as the surface is not fully passivated by gold clusters, the dissolution of less noble metal will continue in un-dealloyed parts in the same way. With the continuing dissolution of the less noble metal, the surface area increases and the noble metal becomes less sufficient to passivate the surface. Therefore, undercutting and bifurcation of ligaments will take place (Figure 2.2c-d). Finally, a bicontinuous porous structure with pore size (distance between ligaments) close to the distance between those initial

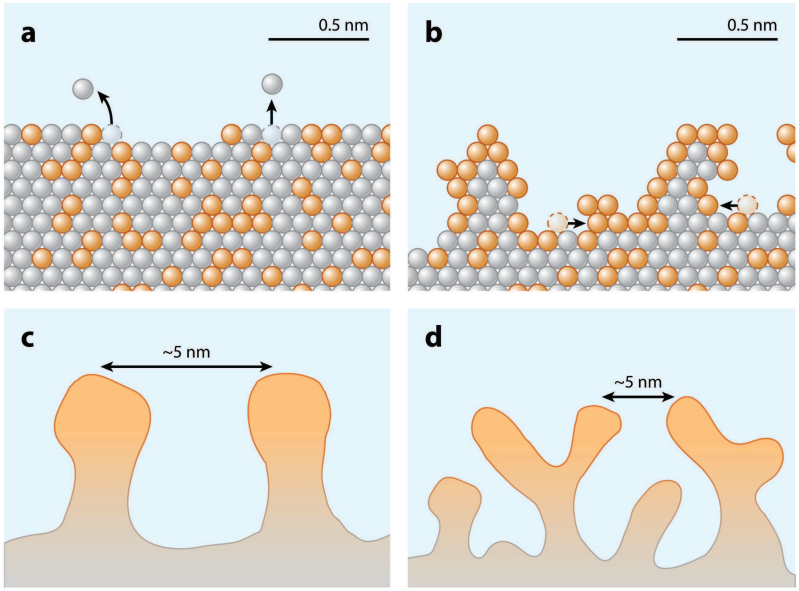

Figure 2.2: A working model for porosity evolution during dealloying one silver-gold alloy. Silver: gray color; gold: orange color. Reprinted with permission from Ref [127].

formed "islands" in Figure 2.2a-b will form throughout the entire dealloying body.

2.2 Larché-Cahn open-system elasticity theory

This section mainly reviews the thermochemical equilibrium in mechanically stressed solid solution and open-system coefficients proposed in the paper titled "A linear theory of thermochemical equilibrium of solids under stress" by Francis Larché and John W Cahn [104].

2.2.1 Main concepts and definitions

Concept of solid network

In the thermomechanical description of solid solution under stress, the concept of solid framework or network was introduced by Larché and Cahn in 1973 [104]. The network denotes the immobile site of a diffusive solid and can be elastically strained by diffusion of mobile species or by mechanical stresses. A good example is Gibbs "solids which absorb fluids", where the solid does not diffuse, but it can reversibly strained by the diffusion of fluid components or by external pressure.

The definition of network is very helpful in the description of displacement and strain for a diffusing solid. In continuum mechanics sense, the displacement of the network is regarded as the displacement of a mechanically stressed solid. The reference state for describing displacements or strain can be arbitrarily chosen. It can be at any fixed hydrostatic stresses and at any constant chemical composition. With attention to a solid solution, the matrix lattice itself is served as network which can be strained by unrestricted diffusion of mobile interstitial or substitutional species, and by applying mechanical stress.

Definition of closed-system and open-system elastic coefficients

In closed system, the elastic strain (ε_{ij}) caused by a mechanical stress (σ_{kl}) is a function of chemical composition. In the linear elastic region and at constant composition, according to

Hooke's Law, closed-system compliance coefficient (S_{ijkl}) is defined by

$$\varepsilon_{ij} = S_{ijkl}\sigma_{kl}\,. \tag{2.1}$$

In open system, local composition of mobile components is variable. Apart from the mechanical stress σ_{ij}, the small fluctuation of composition gives rise to additional strain contribution. Therefore, open-system strain (ε^*_{ij}) is introduced to describe the total strain for a mechanical stressed, diffusive solid solution. By contrast, ε^*_{ij} is defined at constant chemical (or diffusional) potential instead of at constant chemical composition. According to modified Hooke's law at constant chemical (or diffusional) potential, open-system compliance coefficients (S^*_{ijkl}) are defined by

$$\varepsilon^*_{ij} = S^*_{ijkl}\sigma_{kl}\,. \tag{2.2}$$

2.2.2 Open-system elasticity in a binary interstitial solid solution

The detailed deviation of open-system elastic coefficients for binary and multicomponent solids has been made by Larché -Cahn in Ref [104, 129]. This section focuses on the deviation in a simpler case: for a binary interstitial solid solution under uniaxial stress and at constant temperature.

Basic thermodynamic statements

Because the temperature is regarded invariable and simple one-dimensional stress/strain is considered, the Helmholtz free energy density (f) of a binary interstitial solid solution and the differential form of f are expressed as

$$f = f(\varepsilon, x)\,, \tag{2.3}$$

$$\mathrm{d}f = \sigma\mathrm{d}\varepsilon + \rho_0\mu\mathrm{d}x\,, \tag{2.4}$$

with ε - strain, x - the atomic fraction of solute, σ - stress, ρ_0 - volumetric lattice site density at reference state and μ - chemical potential of solute. For convenience, the state of solid under zero stress is taken as the reference state. The variable set (ε, x) in equation 2.4 is changed into (σ, x) by a Legendre transformation. It gives

$$\mathrm{d}(f - \sigma\varepsilon) = -\varepsilon\mathrm{d}\sigma + \rho_0\mu\mathrm{d}x\,. \tag{2.5}$$

By differentiating equation 2.5 twice with respect to σ and x, it gives the following Maxwell relation

$$\frac{\partial\mu}{\partial\sigma}|_x = -\rho_0^{-1}\frac{\partial\varepsilon}{\partial x}|_\sigma\,. \tag{2.6}$$

Compliance differences between open system and closed system

Four variables (stress, strain, composition, chemical potential) are used to describe the state of a binary interstitial solid solution in three conditions: reference state, state 1 and state 2. The reference state has zero stress, zero strain, a solute fraction of x_0, and a solute chemical potential of μ_0. The states 1 and 2 are formed after applying a uniaxial stress (σ) on a solid at the reference state in closed system and open system, respectively. The values of four variables at the three states are shown in Figure 2.3.

From reference state to state 1, the solute fraction keeps constant, so Hooke's law is valid. The strain (ε) caused by σ can be written by

$$\varepsilon = S\sigma\,, \tag{2.7}$$

where S is the closed-system compliance coefficient.

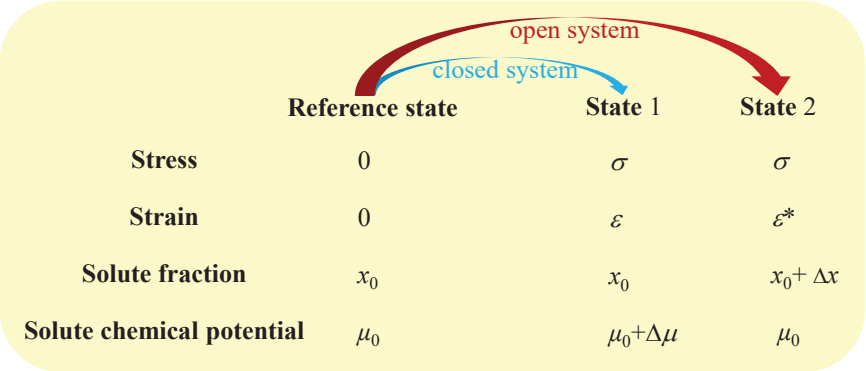

Figure 2.3: Illustration of how four variables (stress, strain, composition and chemical potential) vary during applying a mechanical stress on a solid in closed system and open system. In closed system, it changes from reference state to state 1. In open system, it changes from reference state to state 2.

From reference state to state 2, the solute chemical potential keeps constant, so the composition variation can be written by

$$\mathrm{d}x = \frac{\partial x}{\partial \sigma}|_{\mu}\mathrm{d}\sigma\,. \tag{2.8}$$

Making a mathematical conversion $\frac{\partial x}{\partial \sigma}|_{\mu} = -\frac{\partial x}{\partial \mu}|_{\sigma}\frac{\partial \mu}{\partial \sigma}|_{x}$ and using the Maxwell relation equation 2.6, equation 2.8 becomes

$$\mathrm{d}x = \rho_0^{-1}\frac{\partial x}{\partial \mu}|_{\sigma}\frac{\partial \varepsilon}{\partial x}|_{\sigma}\mathrm{d}\sigma = \chi\eta\mathrm{d}\sigma\,, \tag{2.9}$$

where $\chi = \rho_0^{-1}\frac{\partial x}{\partial \mu}|_{\sigma}$ is the solute susceptibility and $\eta = \frac{\partial \varepsilon}{\partial x}|_{\sigma}$ is the concentration-strain coefficient.

From state 1 to state 2, the stress is the same, the strain and solute fraction variation can be linked via the strain-concentration coefficient by

$$\mathrm{d}(\varepsilon^* - \varepsilon) = \frac{\partial \varepsilon}{\partial x}|_{\sigma}\mathrm{d}x = \eta\mathrm{d}x\,. \tag{2.10}$$

According to equation 2.2, the open-system strain relating to the open-system compliance coefficient, S^*, becomes

$$\varepsilon^* = S^*\sigma\,. \tag{2.11}$$

From equations 2.9, 2.10, 2.11 and 2.7, the difference between open- and closed-system compliance coefficients $(S^* - S)$ is deduced

$$S^* - S = \chi\eta^2\,. \tag{2.12}$$

Isotropic approximation

In the polycrystalline, most metals or alloys are considered as isotropic materials. The difference between open- and closed-system compliance coefficients under uniaxial stress in equation 2.12, $S^* - S = \chi\eta^2$, is valid in isotropic materials. In isotropic materials, the open-system Young's modulus $(Y^* = 1/S^*)$ is related with closed-system Young's modulus $(Y = 1/S)$ via

$$Y^* = \frac{Y}{1 + \chi\eta^2 Y}\,. \tag{2.13}$$

The relative compliance difference between open system and closed system $(\Delta s = (S^* - S)/S)$ is expressed as

$$\Delta s = \chi\eta^2 Y\,. \tag{2.14}$$

Chapter 3

Materials preparation and method

3.1 Electrochemical cells

Two three-electrode chemical cells were used for all electrochemical experiments in this thesis. Figure 3.1a shows a double-jacketed cell with a relatively large capacity of 200 mL. This cell was used in dealloying, electrochemical reduction, and in-situ dilatometry experiments. The temperature of solution in the cell was controlled by a refrigerated bath circulator (Haake A 28, Thermo Fisher Scientific) via circulating water through the vacuum jacket. The other type is a single-wall cell which has a relatively small capacity of 10 mL, as shown in Figure 3.1b. This cell was used in in-situ dynamic mechanical analysis (DMA) experiments for the sake of limited space of the DMA sample holder.

Both cells were made of quartz, resistant to many chemicals such as aqueous solutions of H_2SO_4, HNO_3 and HCl that were used in current thesis. Sulfuric acids with concentrations of 0.1-1.0 M were prepared by diluting high-concentrated H_2SO_4 with different amount of ultrapure water (Ultra Clear TWF, Siemens). The high-concentrated sulfuric acid with a lower purity (95-98 wt%, PanReac AppliChem) was preferred for sample synthesis processes and the high-concentrated sulfuric acid with a higher purity (96 wt%, Suprapur, Merck Millipore) was preferred for electrochemo-mechanical coupling measurements.

Regardless of the volume, three electrodes were inserted in each cell during electrochemical experiments: (1) A working electrode (WE), where reactions of interest take place such as corrosion of Cu from an Cu-Pd alloy during dealloying. (2) A reference electrode (RE), against which the electric potential of WE is established. For the big cell in Figure 3.1a, a commercial Ag/AgCl/3 M KCl (RE, Sigma-Aldrich) was used. For the small cell in Figure 3.1b, a pseudo Ag/AgCl electrode [120] was used due to its compatible size with the cell. Before using, RE was calibrated against a standard hydrogen electrode (SHE, Gaskatel) at room temperature in the electrolyte that was going to be used for synthesis or analysis. (3) A counter electrode (CE), which is used to flow electric current from/to WE. In dealloying experiments, a CuPd alloy was used as WE and Cu wire was used as CE. In the other electrochemical experiments, nanoporous Pd was used as WE and a piece of carbon fiber cloth was used as CE. A potentiostat (PGSTAT302N, Metrohm) was used to apply potential between WE and CE, and record current response and charge transfer at the same time.

3.2 Electrochemical methods

3.2.1 Constant potential

Constant potential is a technique that applies an invariable potential on the working electrode. This technique was mainly used in dealloying experiments. Figure 3.2a shows a potential-time procedure employed during dealloying $Cu_{85}Pd_{15}$ alloys in 1.0 M H_2SO_4 aqueous solutions.

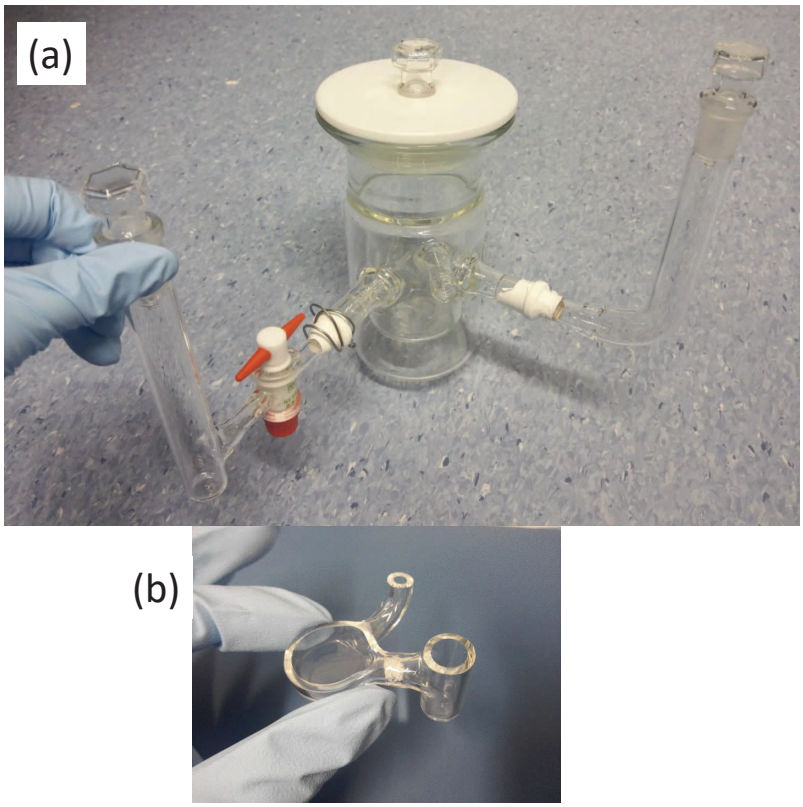

Figure 3.1: Photos of three-electrode chemical cells. (a) A double-jacketed cell (200 mL capacity). (b) A single-wall cell (10 mL capacity).

Corresponding current and charge transfer versus time are presented in Figure 3.2b and 3.2c, respectively. The applied potential is above critical dealloying potential. On the working electrode side, Cu from master alloy is continuously oxidized into Cu^{2+} and then dissolves into the electrolyte; on the counter electrode side, copper deposition ($Cu^{2+} \rightarrow Cu$) and hydrogen evolution take place. During these processes, current flows through the circuit and charge accumulates. With the consumption of Cu from the master alloy, the value of current decreases and the total electric charge increases. When current approaches to zero, it indicates the completion of corrosion process.

3.2.2 Potential step

Potential step is a technique that applies a sequence of above-mentioned constant potential procedures. In this thesis, the potential step method was utilized to enable hydrogen absorption/desorption reach a near-equilibrium state, see Section 4.3. An example of such potential step procedure is shown in Figure 3.3. Potentials are switched between 0.06 and 0.38 V for hydrogen absorption and desorption, respectively (Figure 3.3a). Figure 3.3b shows the corresponding current response during hydrogen electrosorption processes.

3.2.3 Potential sweep

Potential sweep (or voltammetry) studies the current variation in response to applied potentials. In this thesis, two stationary techniques: linear sweep voltammetry and cyclic voltammetry were employed. In both techniques, potential values varied linearly with time. The absolute value of the slope of potential-time graph was defined as the scan rate. For example, the scan rates in Figure 3.4 and Figure 3.5 are 1 and 10 mV/s, respectively.

Linear Sweep Voltammetry is a technique where the potential is swept linearly from

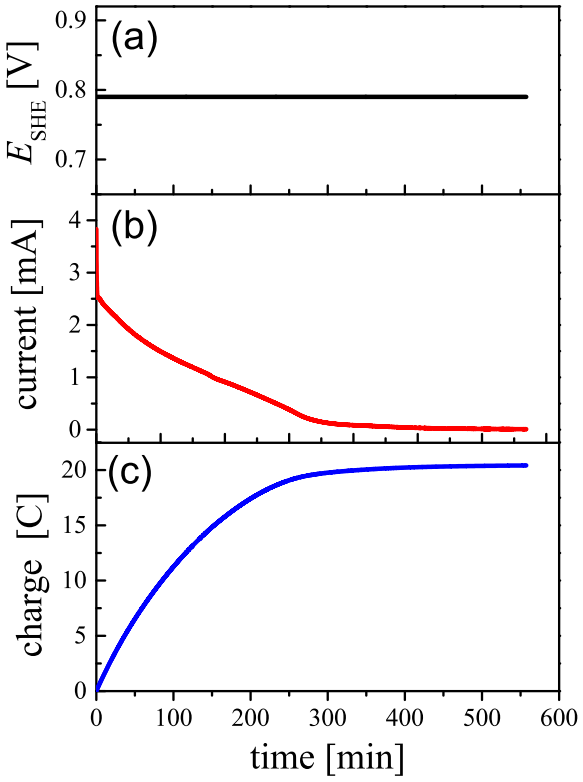

Figure 3.2: The application of constant potential technique in dealloying a $Cu_{85}Pd_{15}$ alloy in 1.0 M H_2SO_4. (a) Electrode potential (E_{SHE}), (b) current and (c) charge versus time.

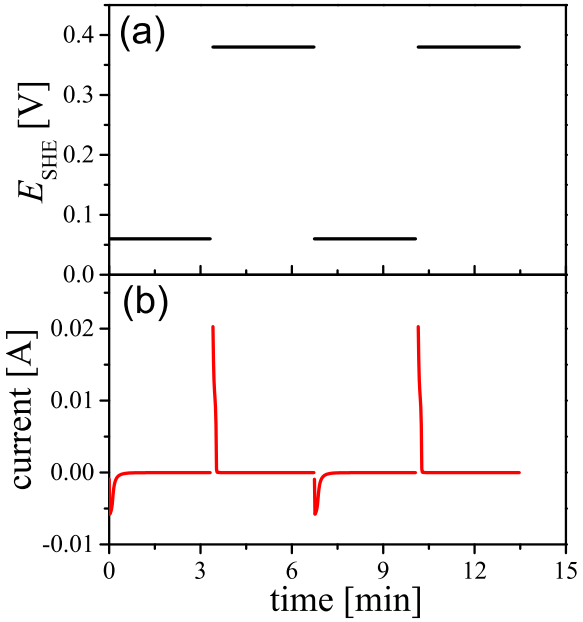

Figure 3.3: A potential step procedure for exploring hydrogen sorption in np-Pd. (a) Potential (E_{SHE}) and (b) current versus time.

the lower limit to the upper limit in a potential range of interest, as shown in Figure 3.4. In this thesis, this technique was used to measure polarization curves of pure Cu, pure Pd and Cu-Pd alloys in different environments. Their polarization plots were further analyzed to estimate proper dealloying conditions for synthesizing np-Pd. For instance, when potential was linearly swept on $Cu_{85}Pd_{15}$ in 1.0 M H_2SO_4 at a scan rate of 1 mV/s at room temperature, the variation of current density (j, defined as current per sample's original geometric area) in response to potential could be obtained. The logarithmic plot of the absolute value of current density as a function of potential is shown in Figure 3.4b, which can be used to estimate the critical dealloying potential on the basis of Sieradzki's strategy (see Section 2.1.2).

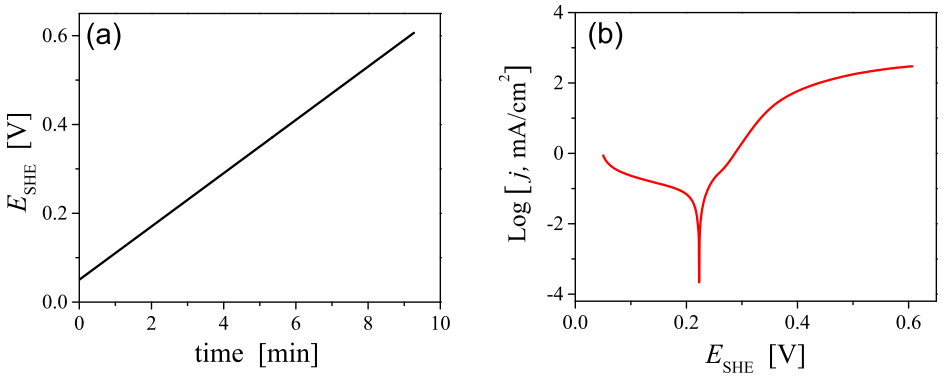

Figure 3.4: Typical linear sweep voltammetry of Cu in 1.0 M H_2SO_4 at a scan rate of 1 mV/s at room temperature. (a) Electrode potential (E_{SHE}) versus time. (b) Logarithm of current density (log j) versus potential.

Cyclic Voltammetry (CV) is a technique where the potential is swept between two potential values at a fixed rate and then swept back from the end-point to the starting point. In this thesis, the CV technique was mainly used in (1) electrochemical reduction of np-Pd and np-Pd-Au, (2) determination of electrochemical active surface area of np-Pd, and (3) control of hydrogen electrosorption reactions during in-situ chemo-mechanical measurements. Figure 3.5 shows a typical cyclic voltammogram of np-Pd in 1.0 M H_2SO_4 measured at a scan rate of 10 mV/s at room temperature.

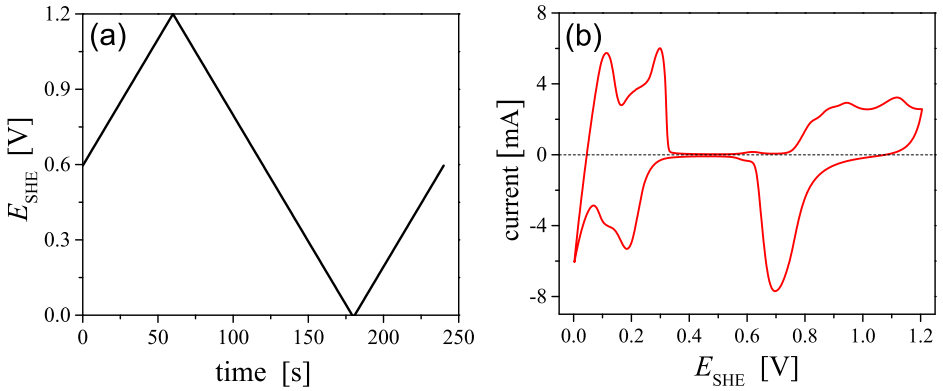

Figure 3.5: Typical cyclic voltammogram of np-Pd in 1.0 M H_2SO_4 recorded at a scan rate of 10 mV/s at room temperature. (a) Potential (E_{SHE}) versus time. (b) Current versus potential.

3.3 Materials preparation

3.3.1 Master alloy

The Cu-Pd binary alloy system was chosen as the objective master alloy to synthesize np-Pd by electrochemical dealloying due to two main reasons: (1) Cu and Pd can form a continuous series of solid solutions in the whole composition range [130], facilitating the formation of a homogeneous single-phase alloy. (2) The big equilibrium metal/metal ion potential difference (more than 0.5 V) between Cu and Pd enables the possibility of dissolution of only Cu.

Ingots of single-phase $Cu_{75}Pd_{25}$, $Cu_{80}Pd_{20}$ and $Cu_{85}Pd_{15}$ alloys were prepared by alloying Cu wires (99.99%, Alfa Aesar) and Pd wires (99.95%, Heraeus Metals) through repeated melting/solidification inside a compact arc melter (MAM-1, Edmund Bühler) under argon atmosphere. During the process, every ingot around 2.5 g in total mass was turned around for at least 20 times to ensure a well distribution of elements. The obtained ingot was named as as-cast sample. Some of the as-cast ingots were vacuum-sealed in quartz tubes for homogenization at 800-900 °C for 5 days followed by quenching in water; some of the as-cast ingots were directly used in the as-cast state. Each of these two variants were cold-rolled by using a manual rolling mill (Dohrmann 726W) and then cut into cuboids, around $1\times1\times1\,mm^3$ in size by using a diamond wire saw (Model 3032, Well Diamond Wire Saw). Afterwards, the obtained cuboids were cleaned in an ultrasonic cleaner, using acetone and ethanol as cleaning solvents. The cleaning time in each solvent was 10 minutes. Finally, the samples were dried in a fume hood at room temperature, being ready for dealloying without any further annealing treatments [42].

Ingots of $Cu_{85}Pd_{12.5}Au_{2.5}$ master alloys were prepared from Cu (99.99%, Alfa Aesar), Pd (99.95%, Heraeus Metals) and Au wires (99.99%, Sigma-Aldrich) by repeated melting/solidification in an arc melter. The ingots were directly cold-rolled into 1.1 mm-thick plates and then cut into cuboids ~$1.1\times0.9\times0.9\,mm^3$ in size without any further homogenization and annealing.

3.3.2 Electrochemical dealloying

Manoporous palladium-based materials were prepared by electrochemical dealloying copper-palladium-based master alloys. The dealloying process was carried out in the relatively big three-electrode chemical cell (Figure 3.1a) containing 1.0 M H_2SO_4 aqueous electrolyte. The temperature of electrolyte was controlled by using a refrigerated bath circulator. The three-electrode setup used a Cu wire as CE, an Ag/AgCl/3 M KCl as RE and a master alloy as WE. Selective dissolution of less noble metal Cu and reconstruction of more noble elements were driven by externally applied electrode potentials. The electrode potential, E, was held constant at a defined value until the current fell to 10 μA. Afterwards, the obtained np sample (named as as-dealloyed sample) was cleaned with ultrapure, deionized water (Ultra-Clear TWF, Siemens) for 2-5 hours.

3.3.3 Electrochemical reduction

Electrochemical reduction is typically used to further remove residual less noble metals via applying several CV cycles on as-dealloyed nanoporous metals. For example, Mameka reported that electrochemical dealloying of $Ag_{75}Au_{25}$ in 1.0 M $HClO_4$ produced as-dealloyed np-Au samples containing 15 at% residual Ag. After imposing 15 cycles potential sweep between 0 and 1.5 V at a scan rate of 5 mV/s on these as-dealloyed np-Au samples, the residual Ag was significantly reduced down to 3 at% [53].

In this thesis, an electrochemical reduction was imposed on as-dealloyed np-Pd in the form of 20 potential cycles between 0 and 1.2 V at a scan rate of 10 mV/s at room temperature in order to minimize residual Cu. This experiment used fresh 1.0 M H_2SO_4 as electrolyte

and carbon fiber cloth (1200-1750 m^2/g, Kynol) as CE. Sample cleaning was carried out by immersing electrochemically reduced np-Pd samples in ultrapure, deionized water (Ultra-Clear TWF, Siemens) for 6 hours and in ethanol (≥99.5%) for another 6 hours. Afterwards, samples were dried for 1 day in argon atmosphere. To distinguish from as-dealloyed np-Pd, the sample after electrochemical reduction was named as as-prepared np-Pd.

3.3.4 Post thermal treatment

Thermal annealing was used in tuning the structure size of nanoporous palladium. As-prepared np-Pd samples were annealed under vacuum for 5 minutes in a furnace (MILA-5000, ULVAC). The operating vacuum pressure is in the range of $1 - 3 \times 10^{-6}$ mbar.

3.4 Materials characterization

3.4.1 Scanning electron microscopy

Scanning electron microscopy (SEM) was used to characterize the microstructure of nanoporous palladium-based samples. Zeiss Supra VP 55 SEM with in-lens detector was used at an accelerating voltage of 10-20 kV and at a working distance of 4 mm. For much higher resolution, FEI Helios NanoLab G3 SEM was used. The measurements were operated wiht an immersion lens, 2-5 kV accelerating voltage and 2 mm working distance. In order to check the morphologies in the sample center part, the sample was cutted through with a scalpel. The sample of interest was glued on an aluminum stub by using a silver paint. It was then dried and stored in a fume hood before SEM measurements. The morphologies for both outer surface and fracture surface of monolithic nanoporous samples were investigated with SEM.

3.4.2 X-ray energy dispersive spectroscopy

Energy Dispersive X-ray Spectroscopy (EDX) is a quantitative X-ray microanalytical technique to investigate chemical composition distribution. X-ray signals emitted from interaction between electrons beam and the atoms in the sample can be collected by energy-dispersive detector and display as a spectrum of intensity versus X-ray energy. The energies of characteristic X-rays can be used to identify the constituent elements of the analyzed sample; the intensities of characteristic X-ray peaks can be analyzed quantify the content of each element. In order to quantify the amount and distribution of residual Cu in np-Pd samples, Zeiss Supra VP 55 SEM and FEI Helios NanoLab G3 SEM with an energy-dispersive detector (Oxford X-Max 20 SDD) were used. With Zeiss Supra VP 55 SEM, a 15 kV accelerating voltage and a 8 mm working distance were used. When using FEI Helios NanoLab G3 SEM, EDX measurements were carried out at an accelerating voltage of 15 kV and at a working distance of 4 mm. Spectra for series of spots from the edge to the center on the fracture surface were analyzed in order to check the homogeneity of chemical composition throughout the entire sample.

3.4.3 Nitrogen adsorption/desorption isotherm

Nitrogen adsorption/desorption in np-Pd was done at 77 K by using an automated gas sorption analyzer (Autosorb iQ, Quantachrome). Before nitrogen adsorption/desorption, samples were degassed at 393 K for 2 hours to remove surface contaminants and adsorbed species. Such low temperature was used in order to avoid coarsening that may occur during degassing. The pore size information was obtained by analyzing the nitrogen adsorption isotherms.

3.4.4 Testing machine

Plastic deformation was performed on dry np-Pd samples with a height of 1.12 mm in the air by using a Zwick Z010 TN testing device. The compression was carried out on a np-Pd sample at a constant engineering strain rate of $10^{-4}\,s^{-1}$, which was controlled by a software named "testXpert II". The strain was precisely recorded by a laser speckle extensometer (Zwick laserXtens).

3.5 Electrochemo-mechanical coupling measurements

3.5.1 In-situ dilatometry

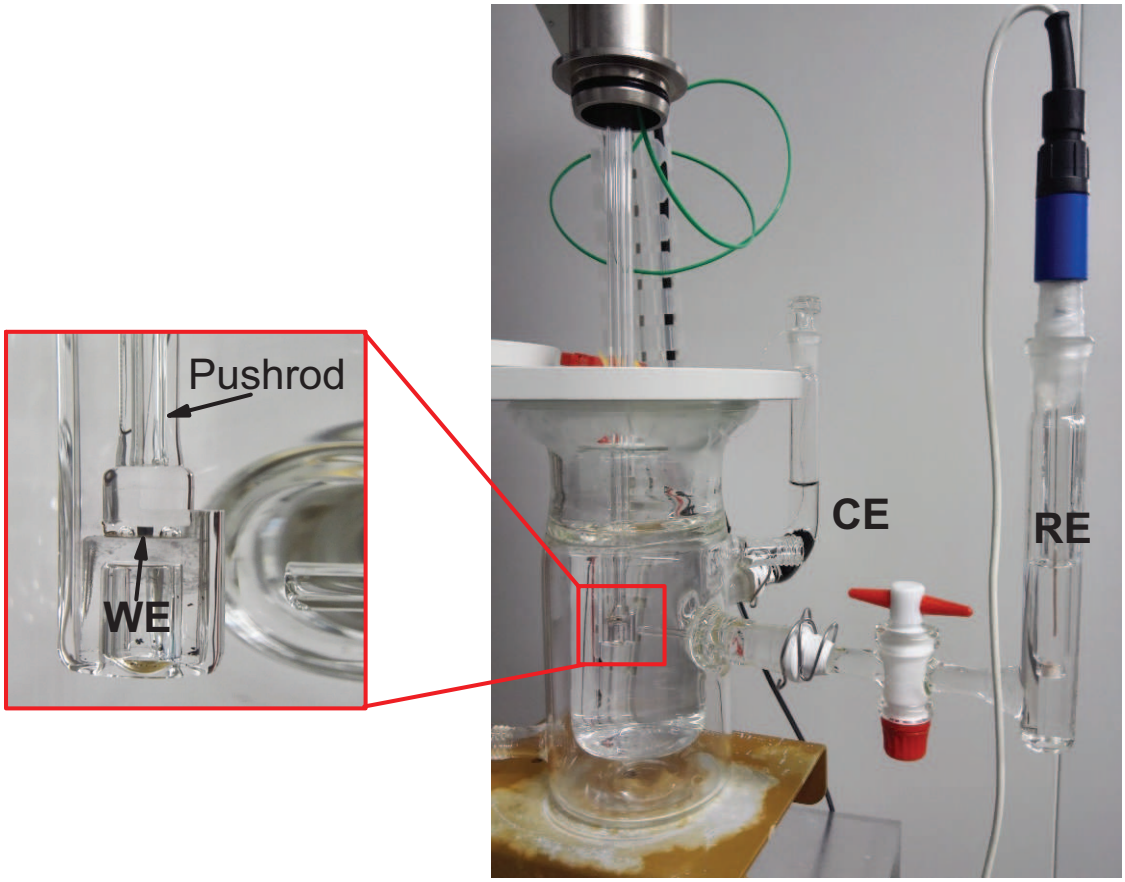

Figure 3.6: In-situ dilatometer setup: a three-electrode chemical cell filled with electrolyte is mounted inside a dilatometer. Enlarged graph of the pushrod is shown on the left. WE: working electrode; CE: counter electrode; RE: reference electrode.

Figure 3.6 shows the photos of an in-situ dilatometer setup. It is constructed by a vertical dilatometer (Linseis L75V), together with a three-electrode chemical cell. The three-electrode chemical cell is filled with 1.0 M H_2SO_4, in which electrochemical reactions take place. A np-Pd sample working as WE under the pushrod of the dilatometer is positioned near the luggin capillary of the three-electrode chemical cell, in order to minimize ohmic potential drop from electrolyte between RE and WE. These three electrodes are connected to a potentiostat which is not shown in the graph. As is shown in the enlarged graph (left), np-Pd is positioned on a gold foil or plate and pressed by the pushrod. Because the upper end of the pushrod is well connected with a displacement sensor, the length of sample is able to be recorded.

In this thesis, a 150 mN force corresponding to an effective compressive stress of about 0.15 MPa was applied on the sample during in-situ dilatometry measurements. Using in-situ dilatometer setup, samples' length variations during dealloying or hydrogen electrochemical adsorption/desorption processes were explored, see Section 4.1.2 and Section 4.3. As shown in Figure 3.7, when imposing potential steps between 0.38 and -0.075 V on np-Pd, cyclic hydrogen absorption/desorption processes lead to cyclic expansion/contraction.

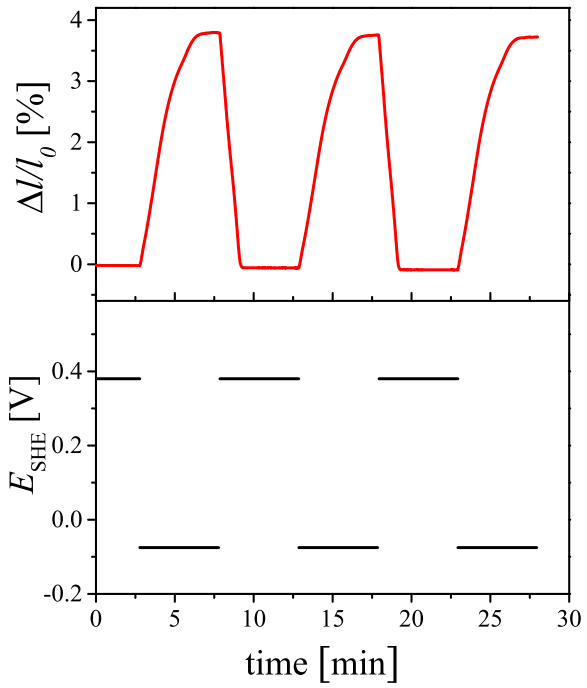

Figure 3.7: Relative length change ($\Delta l/l_0$, red) and electrode potential (E_{SHE}, black) versus time.

3.5.2 In-situ dynamic mechanical analysis

In-situ dynamic mechanical analysis (DMA) was employed to quantify the variation of elastic parameters of np-Pd or np-Pd-Au samples in response to bulk hydrogen fraction (x_{H}, defined as the atomic ratio between interstitial hydrogen and host metals). The validity of effective Young's modulus measured by in-situ DMA has been verified with nanoporous gold by comparing to the results obtained from conventional compression tests [53].

As illustrated in Figure 3.8a, the in-situ DMA is constructed with a tiny electrode chemical cell and a dynamic mechanical analyzer of DMA/SDTA861e (Mettler Toledo). Here, WE is the np-Pd sample inside the tiny three-electrode electrochemical cell; RE is a pseudo Ag/AgCl electrode [120]; CE is a piece of carbon fiber cloth. The electrolyte is 1.0 M H_2SO_4 aqueous solution. A potentiostat is used to apply cyclic potentials and/or potential jumps on np-Pd electrode in order to control hydrogen absorption/desorption processes and hydrogen fraction in np-Pd. H-induced relative length change ($\Delta l/l_0$), loss modulus ($Y^{\mathrm{eff}}_{\mathrm{loss}}$) and effective Young's modulus (Y^{eff}) changes are recorded by DMA, as shown in Figure 3.8b.

In the measurements, the upper black clamp together with the quartz-made push rod were fixed; the other part under the sample was movable and connected to the oscillator of DMA. Therefore, the loading direction was from bottom to up. During tests, the force applied on the sample was a sum of a static force and a sinusoidal dynamic force. The experiments were performed on bulk samples of np-Pd (size: ~$1.1 \times 0.85 \times 0.85\,\mathrm{mm}^3$) and np-Pd-Au (size: ~$1.1{\times}0.9{\times}0.9\,\mathrm{mm}^3$). For np-Pd, the mechanical measurements used a dynamic strain amplitudes (peak-to-peak) in the range of 0.2-0.8% with an oscillation frequency in the

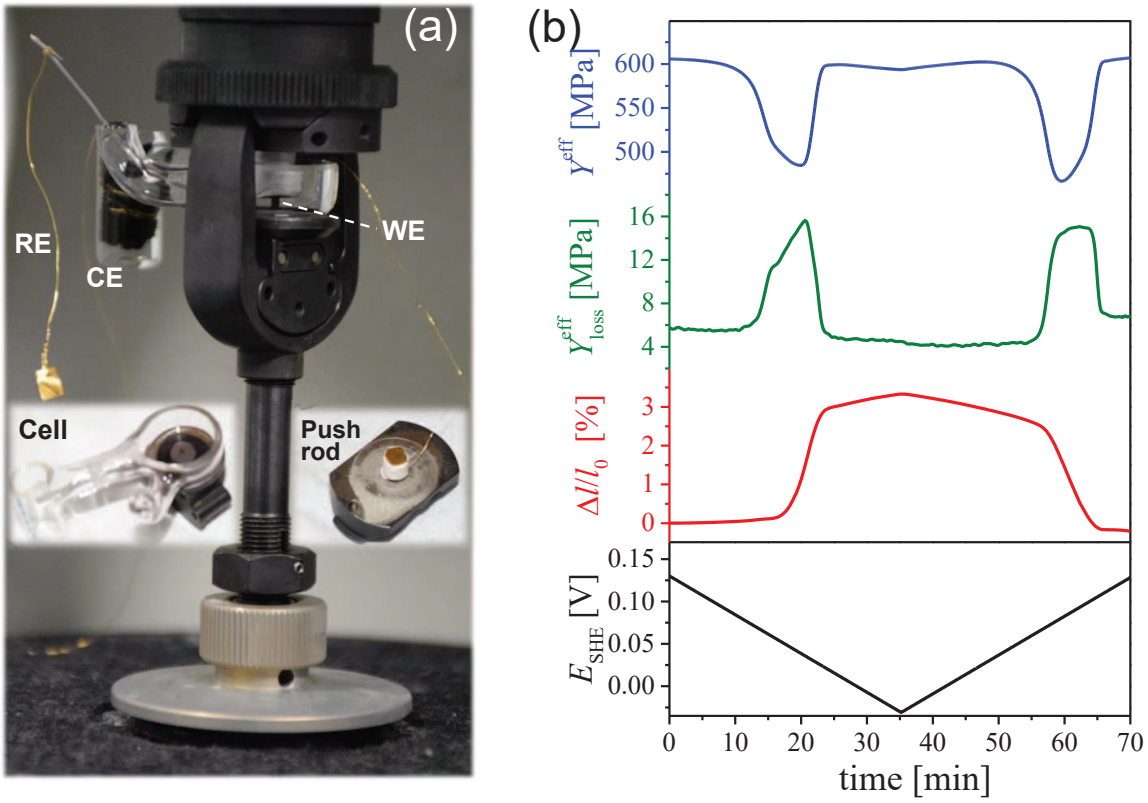

Figure 3.8: In-situ dynamic mechanical analysis (DMA) on np-Pd. (a) Experimental setup: a three-electrode chemical cell with electrolyte mounted in a DMA. WE: working electrode; CE: counter electrode; RE: reference electrode. (b) Effective Young's modulus (Y^{eff}, blue), loss modulus ($Y^{\text{eff}}_{\text{loss}}$, dark green), relative length change ($\Delta l/l_0$, red) and potential (E_{SHE}, black) versus time.

range of 1-100 Hz and a static force of 2-5 N. For np-Pd-Au, the mechanical measurements used a dynamic strain amplitude (peak-to-peak) in the range of 0.3-0.4% with an oscillation frequency of 1 Hz or 3 Hz, and a static force of 9-11 N.

Chapter 4

Results

4.1 Synthesis of nanoporous palladium

4.1.1 Electrochemical behavior of copper-palladium alloys

As mentioned in the theoretical background section, in order to fabricate nanoporous metals, it is necessary to carefully consider the balance between the corrosion rate of more active metals and the surface diffusion rate of more noble metals. It has been demonstrated that the balance can be adjusted by varying master alloy or dealloying environments. For example, parameters including the chemical composition of master alloy, electrolyte type and concentration, dealloying temperature as well as externally applied potential value can affect dealloying processes and final microstructures [131]. In this section, influences of many dealloying parameters on the corrosion behaviors of pure Cu, pure Pd, and Pd-Cu alloys are explored by analyzing their polarization curves. The pure metal samples for polarization tests were cylinders, usually 2-3 mm long and 1 mm in diameter. The alloy samples for polarization tests are typically 1 mm-sized cubes.

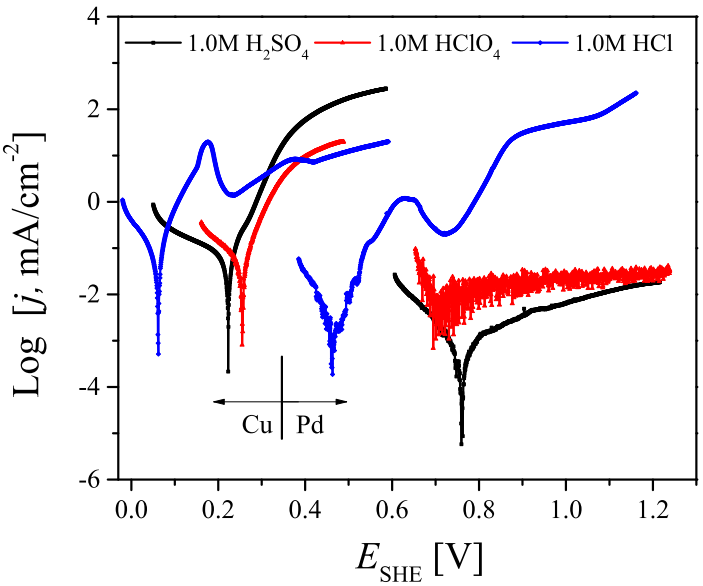

Figure 4.1: Polarization curves for pure Cu and Pd obtained in different acids at 25 °C. j stands for current density.

Figure 4.1 shows the polarization plots for Cu and Pd in 1.0 M H_2SO_4, 1.0 M $HClO_4$ and 1.0 M HCl solutions, respectively. It shows that Cu begins to corrode at a much lower

potential and has a higher corrosion current density than Pd, indicating that Cu is much more electrochemically active than Pd in these three kinds of acids at room temperature. The difference between Cu and Pd in the free corrosion potential is from 0.4 to 0.6 V. This large potential difference favors the choice of a dealloying potential that allows the dissolution of only copper. When the corrosion rate of Cu is much larger than that of Pd, dissolution of a small amount of Pd is also acceptable provided that the remaining amount of Pd is much enough to construct a bicontinuous porous network. Although these three acids have the same concentration, it is apparent that Cu corrosion in H_2SO_4 shows the largest current density but Pd corrosion in the electrolyte shows the lowest current density. This observation implies that the maximum current density difference, in other words, the largest corrosion rate difference between Cu and Pd occurs in H_2SO_4. Therefore, H_2SO_4 is chosen as the default electrolyte in subsequent studies.

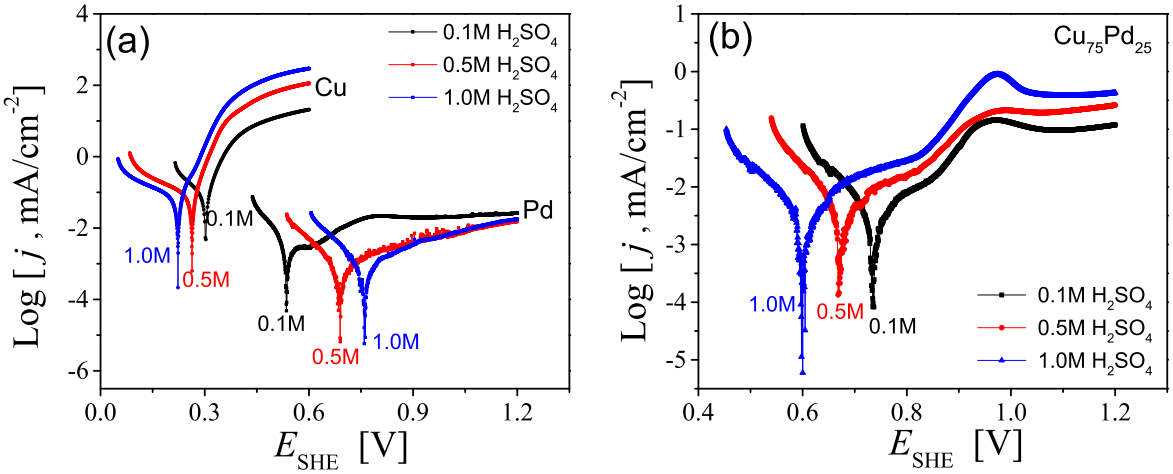

Figure 4.2: Polarization curves for (a) Cu, Pd and (b) $Cu_{75}Pd_{25}$ in 0.1, 0.5 and 1.0 M H_2SO_4 electrolytes at 25 °C .

Figure 4.2a shows the polarization curves for pure Cu and Pd in 0.1, 0.5 and 1.0 M H_2SO_4 aqueous solutions. As the concentration of H_2SO_4 increases, the corrosion potential of Cu decreases, indicating that Cu becomes more active. Figure 4.2a also shows that as the concentration of H_2SO_4 increases, the current density for Cu corrosion at the same potential increases, indicating the corrosion rate of Cu accelerates. By contrast, the variation of the corrosion behavior of Pd with acid concentrations show an opposite trend. Apparently, in the investigated potential range (less than 1.2 V), the current density from Pd dissolution is much smaller than that from Cu dissolution at the same potential. Pd exhibits several orders of magnitude slower corrosion rate than Cu.

Figure 4.2b shows the polarization curves for $Cu_{75}Pd_{25}$ in 0.1, 0.5 and 1.0 M H_2SO_4 aqueous solutions, respectively. The influences of acid concentration on the corrosion rate and corrosion potential of Pd are similar to that of pure Cu. Empirically, for completely dealloying a bulk sample and then obtaining a bicontinuous and uniform np sample especially with homogeneous composition distribution, the current density from less noble metal corrosion should be over one critical value, otherwise it will lead to passivation or partially dealloyed sample. According to the investigations on Ag-Au alloys in $HClO_4$ electrolyte by Sieradzki *et al.*, the critical potential is defined as the potential value at a current density of 1.0 mA/cm^2 in corresponding polarization plot, above which value continuous dealloying of bulk samples can proceed [121, 122]. Figure 4.2b shows that even the maximum value of corrosion current density of $Cu_{75}Pd_{25}$ in 1.0 M H_2SO_4 electrolyte is smaller than 1.0 mA/cm^2, indicating the difficulty of completely dealloying bulk $Cu_{75}Pd_{25}$ samples in such conditions. Because of

that, $Cu_{85}Pd_{15}$ alloy with a higher Cu content than $Cu_{75}Pd_{25}$ expecting a faster corrosion is explored.

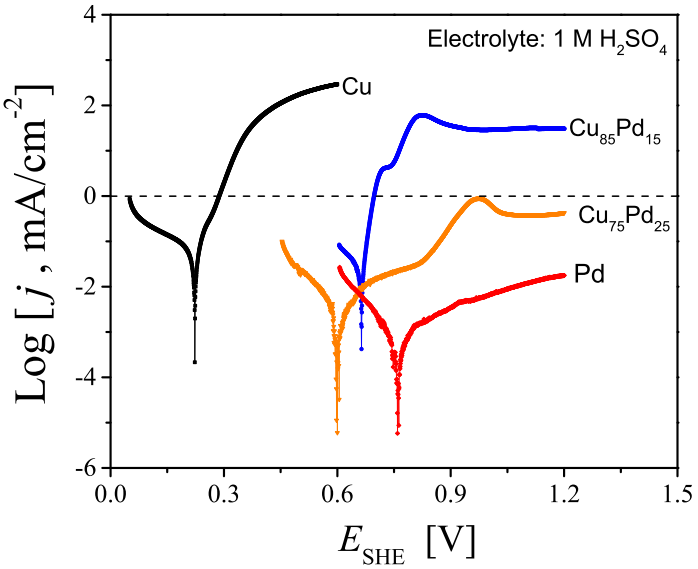

Figure 4.3: Polarization curves for Cu, Pd, $Cu_{75}Pd_{25}$, and $Cu_{85}Pd_{15}$ in 1.0 M H_2SO_4 at 25 °C.

Figure 4.3 shows the polarization curve for $Cu_{85}Pd_{15}$ in 1.0 M H_2SO_4. Polarization curves for pure Cu, pure Pd and $Cu_{75}Pd_{25}$ alloy obtained in the same condition are also presented for comparison. It shows that the polarization curve of $Cu_{85}Pd_{15}$ alloy is similar to that of $Cu_{75}Pd_{25}$. The corrosion behaviors of both alloys appear between the corrosion behaviors of two pure metals, but it is obvious that chemical composition of master alloys can affect their corrosion behavior to some extent. As shown in Figure 4.3, $Cu_{85}Pd_{15}$ alloy with a higher copper content shows much larger value in the maximum current density. This behavior suggests that an $Cu_{85}Pd_{15}$ alloy has a faster corrosion rate than an $Cu_{75}Pd_{25}$ alloy. Moreover, when the applied potential is larger than 0.7 V vs. SHE, the current density for the $Cu_{85}Pd_{15}$ alloy exceeds 1.0 mA/cm^2, which suggests the possibility of completely dealloying of $Cu_{85}Pd_{15}$ bulk samples.

Figure 4.4 shows the polarization curves for $Cu_{85}Pd_{15}$ in 1.0 M H_2SO_4 at 25, 40 and 60 °C. Influences of temperature on the corrosion rate are obvious. The critical dealloying potential is shifted to more negative potential value as dealloying temperature increases. Moreover, the maximum current density increases nearly ten times as temperature increases from 25 to 60 °C, indicating that the maximum dissolution rate of copper also significantly increases with rising temperature.

4.1.2 Dealloying copper-palladium alloys in sulfric acid

Influence of dealloying potential

It was reported that dealloying potential could influence the evolution of porous structure, total volume shrinkage and dealloying efficiency, which might then affect the mechanical behaviors of products [10, 11, 132]. Therefore, a series of dealloying potentials were explored for dealloying $Cu_{85}Pd_{15}$ in 1.0 M H_2SO_4 at 60 °C. It was found that when dealloying potential was $<$770 mV, the dealloying process was extremely slow and even aborted due to passivation, leading to incompletely dealloyed samples. When dealloying potential was greater than $>$820 mV, the dealloying process was rapidly accomplished the as-dealloyed samples showed discontinuities in the microstructure and sometimes even broke into parts. Therefore, the

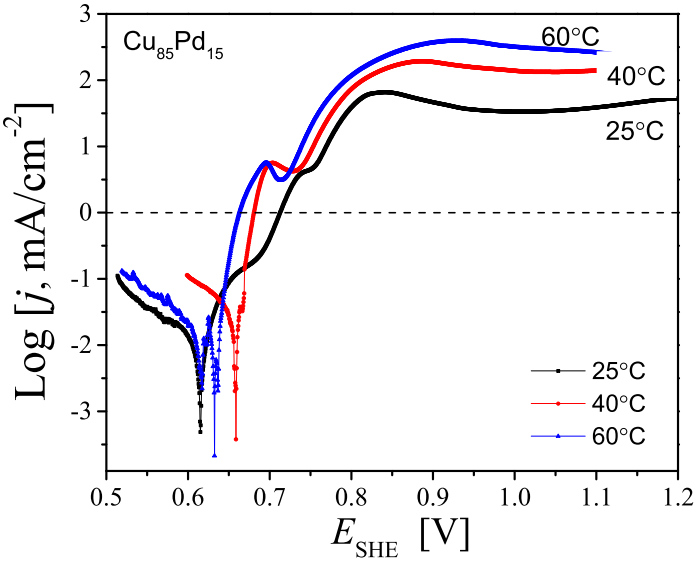

Figure 4.4: Polarization plots for $Cu_{85}Pd_{15}$ in 1.0 M H_2SO_4 at temperatures of 25, 40 and 60 °C.

further investigations were focused on the potentials in-between. The samples' dimension changes and corrosion behaviors during dealloying for several dealloying potentials in the range of 780 to 820 mV were investigated separately by in-situ dilatometry.

Figure 4.5a displays the variation of relative length change $\Delta l/l_0$ with time for various dealloying potentials. Insert diagram shows the total relative length change as a function of dealloying potential. It seems that the length shrinkage increases gradually with the rising dealloying potential. The length shrinkage is within 1%, if the dealloying potential is below 790 mV. When the potential increases to 818 mV, sample shows more than 3% shrinkage. This large shrinkage may explain the abundant cracks in the as-dealloyed samples that were obtained at dealloying potentials above 820 mV.

Current transients during the whole dealloying procedure for various potentials are presented in Figure 4.5b. The integral of current over time gives rise to the total charge (Q_{corr}) caused by corrosion of copper. Based on Faraday's law, the charge and the amount of corroded copper (n_{corr}) can be linked via

$$Q_{\mathrm{corr}} = z n_{\mathrm{corr}} F, \tag{4.1}$$

where z denotes number of the electron transfer in one unit chemical reaction (here it means the Cu corrosion process) and F is Faraday constant. On the basis of Pourbiax diagram of the Cu-O-H system at 25 °C [133], Cu is oxidized into Cu^{2+}, so z is 2 in this case. Therefore, the amount of corroded Cu can be calculated by $n_{\mathrm{corr}} = Q_{\mathrm{corr}}/(2F)$. The amount of Cu ($n_0$) in the master alloy was calculated based on the data: mass of master alloy batch and atomic fraction of Cu (85%). Then the corrosion percentage, ν, of Cu was estimated by the atomic ratio between dissolved Cu and total Cu in the master alloy via n_{corr}/n_0. The calculated results for various potentials are displayed in Figure 4.5c. Interestingly, it is observed that the Cu corrosion percentages for samples synthesized at various dealloying potentials are very close, ν = 97.0±2.0%. From that, an average chemical composition of 14.0±8.0 at% Cu and 86.0±8.0 at% Pd is then estimated for as-dealloyed samples. EDX measurements on the finally as-prepared samples indicate that their chemical compositions are 5.5±2.0 at%. There is only ±2 at% variation between different samples for various potentials. It suggests that dealloying potential shows negligible influences on amount of copper residue in as-prepared samples.

According to equation 4.1, the theoretical charge that is required to completely remove Cu from $Cu_{85}Pd_{15}$ master alloy is $Q_{\mathrm{theo}} = 2n_0F$. To determine the impact of dealloying

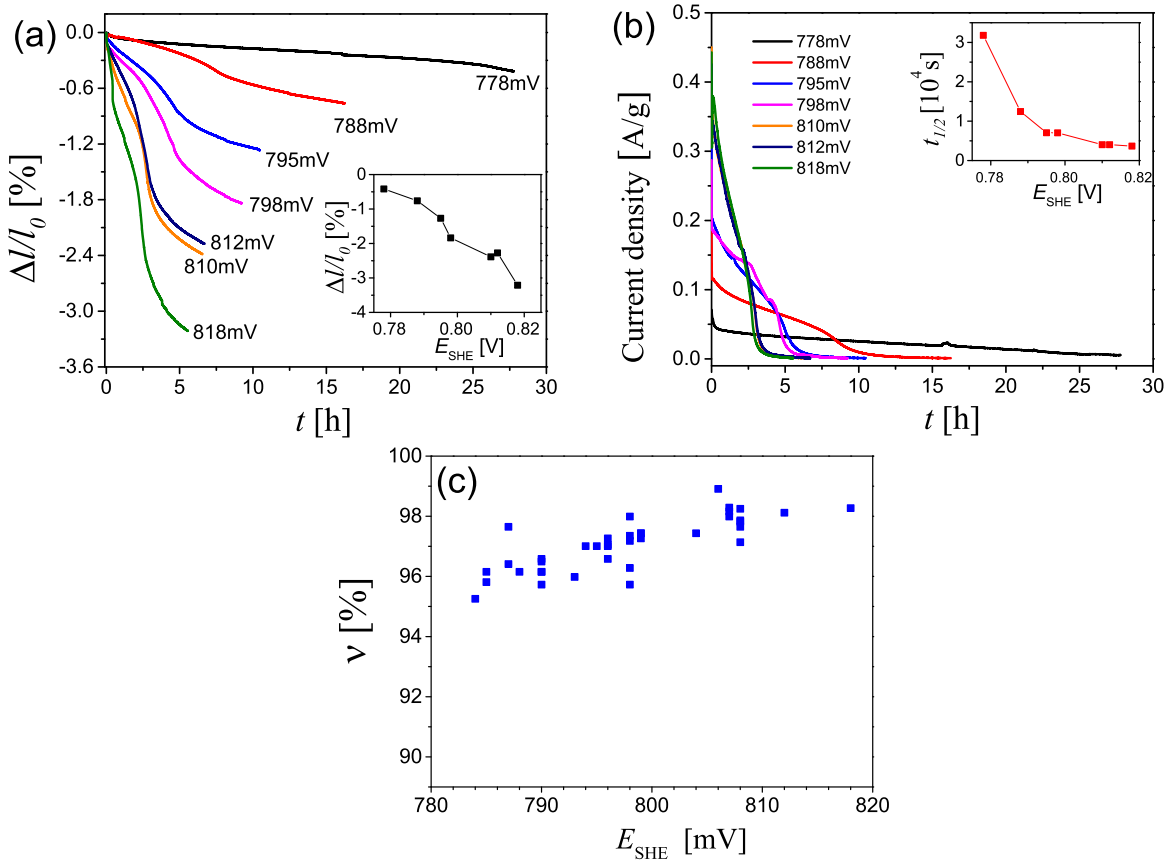

Figure 4.5: Influences of electrode potential on the dealloying of $Cu_{85}Pd_{15}$ in 1.0 M H_2SO_4 at 60 °C. (a) The relative length variation ($\Delta l/l_0$) with time (t), inset: length shrinkage versus dealloying potential (E_{SHE}). (b) The specific current transient with time, inset: half-time ($t_{1/2}$) versus dealloying potential, (c) Cu corrosion percentage (ν) versus dealloying potential.

potential on the corrosion speed, the time to reach $\frac{1}{2}Q_{\text{theo}}$ is named as half-time ($t_{1/2}$). Insert of Figure 4.5b shows the $t_{1/2} - E$ diagram. It is apparent that the half-time decreases with rising dealloying potential. In view of the reasonable dealloying duration around 16 hours and the relatively small length shrinkage (<1%), 790 mV is determined as the typical dealloying potential in subsequent study if it is not specially pointed out.

Influence of dealloying temperature

The as-prepared np-Pd samples were obtained by electrochemical dealloying $Cu_{85}Pd_{15}$ in 1.0 M H_2SO_4 at various temperatures and followed by an electrochemical reduction treatment. Three dealloying temperatures of 25, 60 and 80 °C were investigated. The resulting morphologies of as-prepared samples are displayed in Figure 4.6. Uniform and hierarchical nanoporous structures are observed in the products obtained at these three dealloying temperatures.

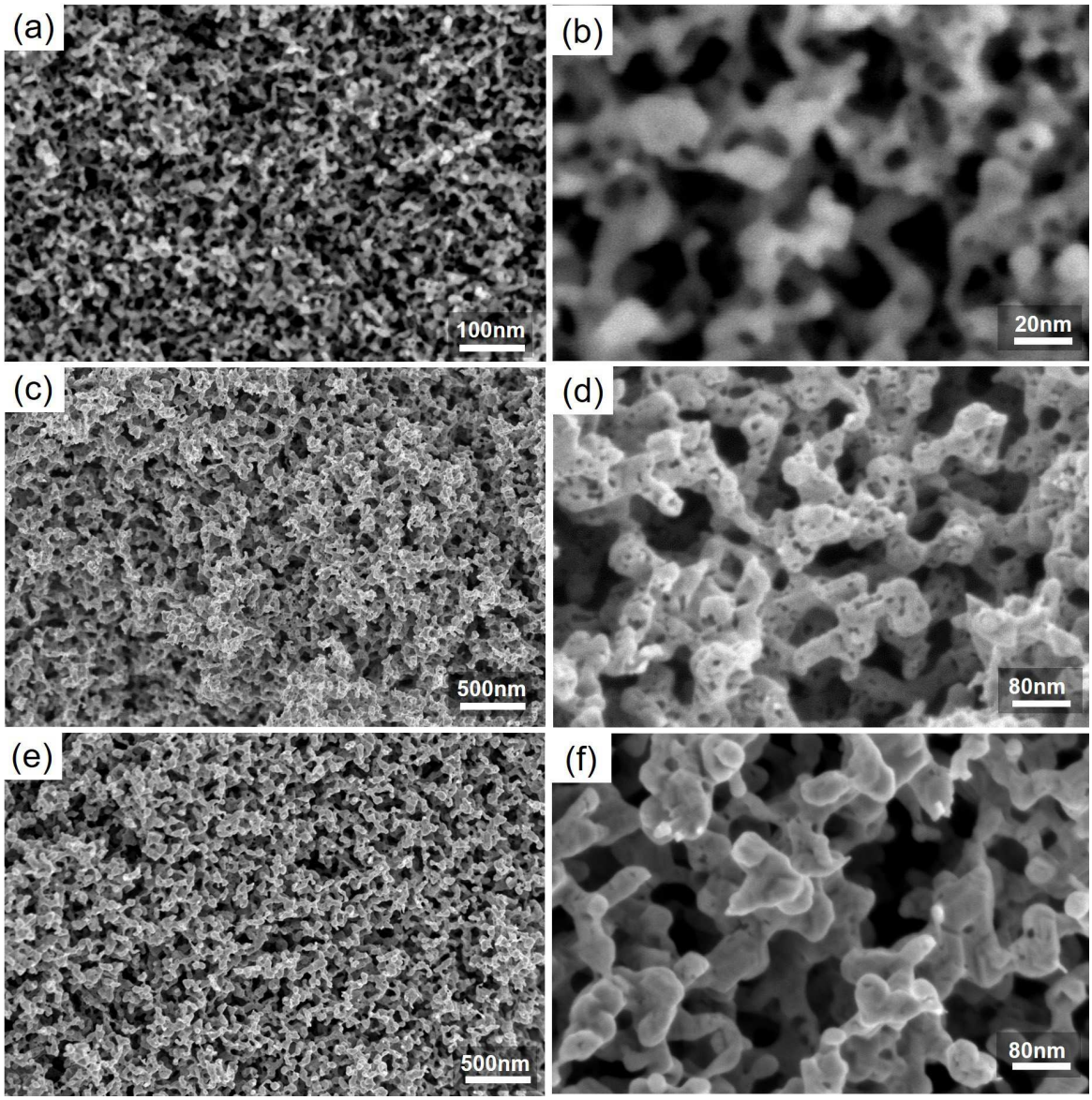

Figure 4.6: Fracture surface morphologies of np-Pd obtained by dealloying $Cu_{85}Pd_{15}$ in 1.0 M H_2SO_4 at temperatures of (a-b) 25 °C, (c-d) 60 °C, and (e-f) 80 °C.

Figures 4.6a-b show that dealloying at the lowest temperature 25 °C gives rise to the

finest structure. Figure 4.6a indicates that the diameter of upper-level ligaments are mostly 10-20 nm. As is shown in the higher magnification image (Figure 4.6b), the low-level pores inside upper-level ligaments are mostly smaller than 5 nm in diameter. The morphologies of np-Pd sample obtained at 60 °C are displayed in Figures 4.6c-d. The ligaments at the upper and lower hierarchy level are doubled in the comparison to that formed at 25 °C. The morphologies of np-Pd obtained at the highest temperature 80 °C are displayed in Figures 4.6e-f. In comparison with samples obtained at 60 °C in Figures 4.6c-d, np-Pd obtained at 80 °C shows slightly increased upper-level ligament size at (Figure 4.6e); the lower-level ligament obviously coarsens and the density of lower-level pores inside upper-level ligaments significantly decreases (Figure 4.6f).

Influence of master alloy composition

The influence of alloy composition on the microstructure of dealloying-made np-Pd materials was explored with three master alloys: $Cu_{85}Pd_{15}$, $Cu_{80}Pd_{20}$ and $Cu_{75}Pd_{25}$. It was found that $Cu_{75}Pd_{25}$ could not be completely dealloyed in 1.0 M H_2SO_4 at 60 °C. Therefore, as-prepared np-Pd samples were obtained by electrochemical dealloying of $Cu_{85}Pd_{15}$ with a potential of 0.79 V and $Cu_{80}Pd_{20}$ master alloys with a potential of 0.835 V, respectively, in 1.0 M H_2SO_4 at 60 °C followed by an electrochemical reduction treatment. EDX analysis on these as-prepared np-Pd samples shows that both samples have a similar Cu content, 5.0 ± 1.5 at%. The resulting morphologies of as-prepared samples based on $Cu_{85}Pd_{15}$ and $Cu_{80}Pd_{20}$ are displayed in Figure 4.7. It is observed that both $Cu_{85}Pd_{15}$ and $Cu_{80}Pd_{20}$ yield uniform, hierarchical nanoporous structures, but at the low hierarchy level, the np-Pd material based on $Cu_{80}Pd_{20}$ shows a lower porosity than the one based on $Cu_{85}Pd_{15}$. Additionally, np-Pd based on the $Cu_{80}Pd_{20}$ master alloy shows a denser structure and a higher Pd fraction than the np-Pd materials based on $Cu_{85}Pd_{15}$ master alloy.

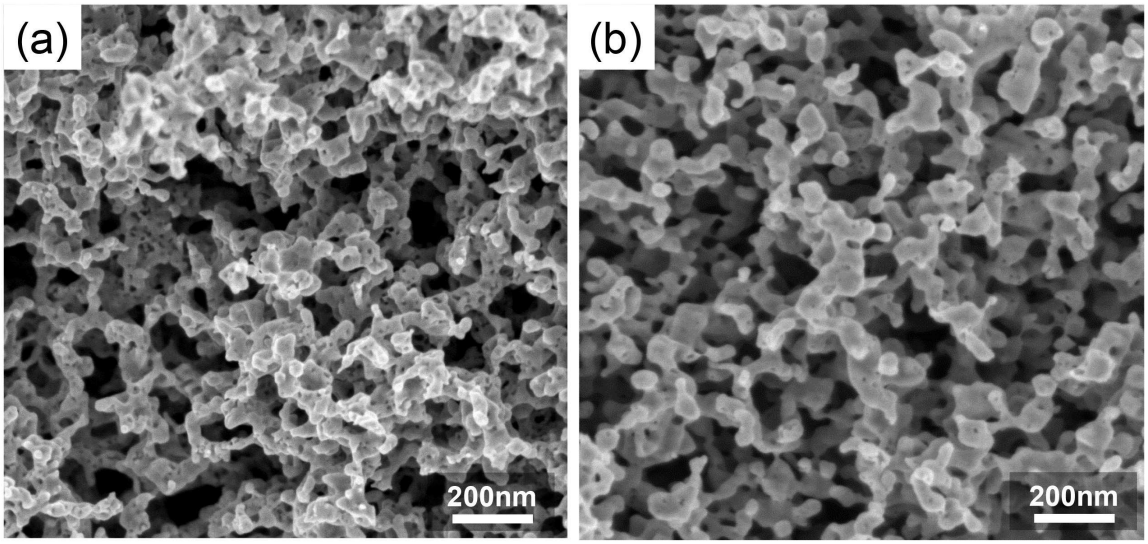

Figure 4.7: Fracture surface morphologies of np-Pd obtained by dealloying (a) $Cu_{85}Pd_{15}$ and (b) $Cu_{80}Pd_{20}$ in 1.0 M H_2SO_4 at 60°C.

4.1.3 Properties of hierarchical nanoporous palladium

This section mainly focuses on two kinds of np samples: (1) as-dealloyed np-Pd samples which were prepared out of $Cu_{85}Pd_{15}$ alloy in 1.0 M H_2SO_4 at 60 °C via applying a constant potential of 790 mV and (2) as-prepared np-Pd samples which were obtained by imposing an electrochemical reduction on as-dealloyed samples in 1.0 M H_2SO_4 at 25 °C.

Morphology and chemical composition

Quantitative EDX spectroscopy analysis was performed on both as-dealloyed and as-prepared np-Pd samples. At least four samples for each variable and four positions in each sample are analyzed to calculate the average residual Cu atomic fraction values for as-dealloyed and as-prepared np-Pd. The as-dealloyed np-Pd samples have an average residual Cu atomic fraction of 13.0±2.0% and the as-prepared np-Pd samples have an average residual Cu atomic fraction of 5.5±1.0 at%.

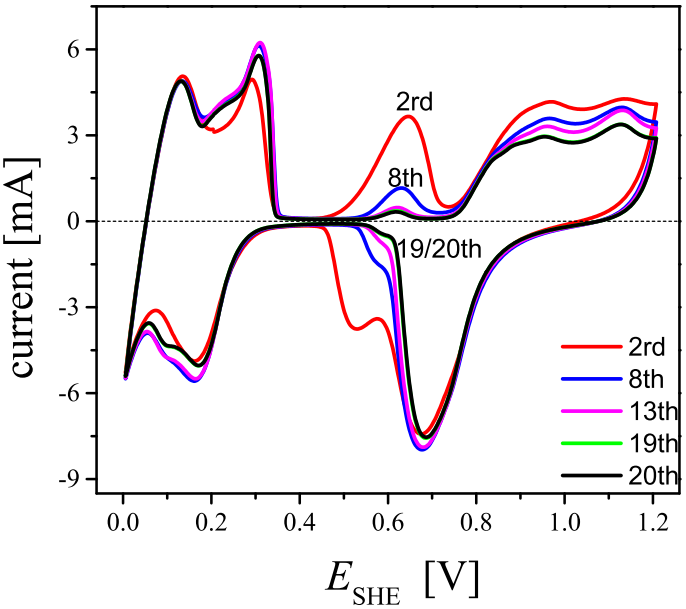

Figure 4.8: Cyclic voltammograms during an electrochemical reduction of as-dealloyed np-Pd in 1.0 M H_2SO_4 at a scan rate of 10 mV/s at 25 °C .

Figure 4.8 presents CV curves selected from the electrochemical reduction process. The most apparent observation is the gradually reduced redox peak near 0.6 V with increasing cycles. Because this redox peak is supposed to be caused by the dissolution/redeposition of Cu [134–136], it further indicates the efficient decrease of Cu content by electrochemical reduction, consistent with the chemical composition results for as-dealloyed and as-prepared np-Pd determined by EDX.

The overviews on the outer surface and fracture surface of np-Pd are shown in Figure 4.9a and b, respectively. Remarkably, no macroscopic cracks are observed throughout the mm-sized sample. Higher-magnification SEM images of the fracture surface in Figures 4.9c-d show a uniform and bicontinuous hierarchical nanoporous network, which is quite different from classic one-step dealloying-made nanoporous structure. For example, one-step dealloying-made np gold typically has a porous structure with one well-defined ligament size distribution [3, 137]. By contrast, two well-defined ligament sizes are observed in the as-prepared np-Pd samples. By measuring the smallest diameter of one ligament and randomly selecting more than 20 ligaments in Figure 4.9c for average. The upper-level ligament size is determined to be 35±5 nm. The diameters of lower-level ligaments are mostly smaller than 10 nm by measuring the size of ligaments within 10 randomly selected upper-level ligaments. The morphologies in Figures 4.9c-d are very representative throughout the entire sample. The good reproducibility was confirmed by using different master alloy batches. Moreover, it was found that there was no big difference in the microstructure whether using as-cast or homogenized master alloys.

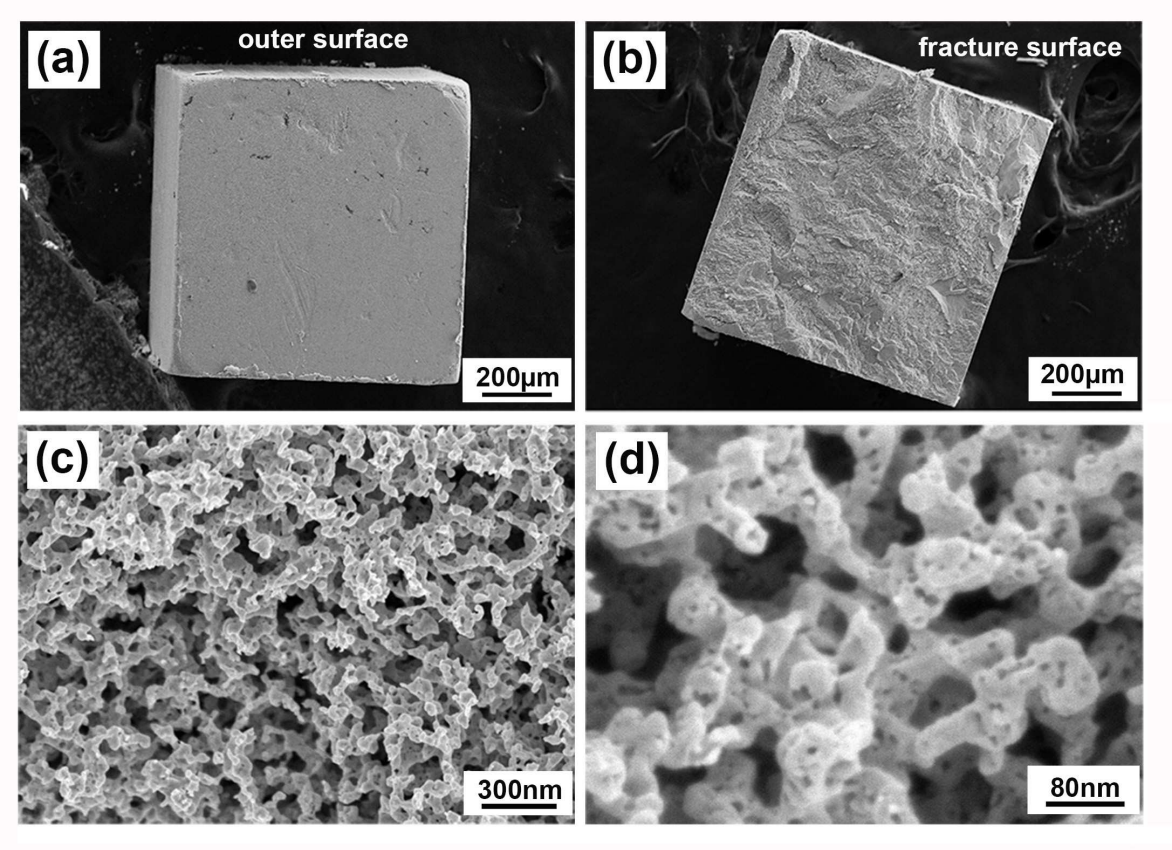

Figure 4.9: Scanning electron micrographs of np-Pd samples. (a) Overview of outer surface. (b) Overview of fracture surface. (c-d) Local view of fracture surface at different magnifications.

Pore size distribution

The entire volume of porous materials is a sum of solid and pores. Porosity of np-Pd is defined as the volume fraction of the entire body that is occupied by the pore space. By contrast, solid fraction (φ) is the volume fraction of the entire body that is taken up by solid part. By measuring the mass (m) and the entire volume of the monolithic body (V), the mean mass density of np-Pd sample, $\rho = m/V = 2.0 \pm 0.1\,\mathrm{g/cm^3}$ is determined by measuring several samples. The mass density of solid phase $Pd_{95}Cu_5$ is predicted by using a general rule of mixtures and using the mass density values from massive Pd and Cu. Therefore, the solid fraction which equals to relative density, $\varphi = 0.168 \pm 0.009$, is estimated from mass density of the np body divided by the mass density of solid phase.

Figure 4.10 shows the average pore size distribution of np-Pd samples obtained by analyzing their nitrogen sorption isotherms. It shows that lower-level pore size is in the range of 2-8 nm, in excellent agreement with SEM characterization in Figure 4.9d. The pore size at upper-level is too large to be analyzed with this approach.

High deformability

Figure 4.11 shows one compression curve of a dry np-Pd sample at room temperature. No failure is observed in the sample even after more than 30% plastic deformation. Here, engineering strain is determined via dividing the length change by the original length; engineering stress is determined via dividing the measured force by the original cross-sectional area. Inserts of Figure 4.11 show photos of np-Pd before and after compression, showing no macroscopical cracks. The outstanding plastic deformability of np-Pd is believed to highly relate to its uniform and homogeneous structure as well as the absence of cracks.

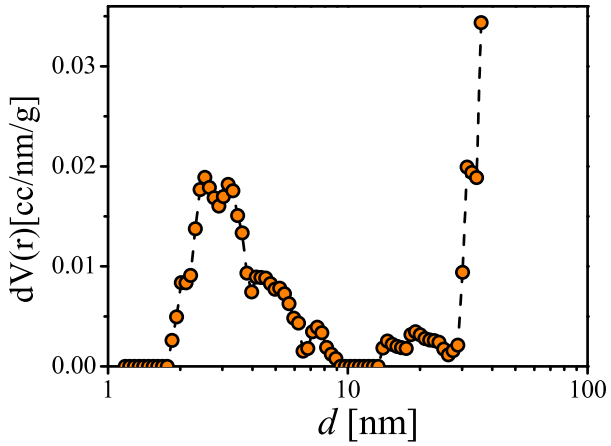

Figure 4.10: Pore size distribution in np-Pd. $\mathrm{d}V(r)$: pore volume fraction; d: pore diameter.

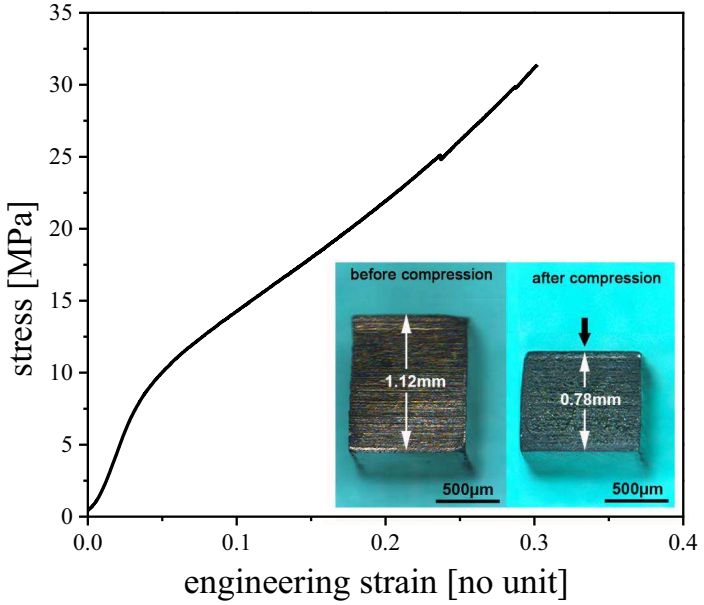

Figure 4.11: Stress-strain curve for np-Pd. Inset: photos before and after compression.

4.1.4 Structure evolution during dealloying

In order to find out the evolution mechanism for hierarchical np-Pd, dealloying was carried out on $Cu_{85}Pd_{15}$ in 1.0 M H_2SO_4 at 60 °C at a constant potential of 790 mV. The theoretical charge (Q_{theo}) required to completely remove Cu from $Cu_{85}Pd_{15}$ master alloy was calculated with the same method in Section 4.1.2. Partially dealloyed sample was obtained by terminating the dealloying process as charge transfer attained $\frac{2}{3}Q_{theo}$.

Figure 4.12a shows an overview of cross-sectional fracture surface of the partially dealloyed sample. The fracture surface is obtained by directly cleaving the sample from the middle across its center. Four representative positions from center to edge, named as P1, P2, P3 and P4 (labeled in Figure 4.12a), are selected for the higher magnification SEM and EDX analysis. The values of chemical composition for P1-P4 measured by EDX are displayed in the form of atomic percent of Cu in Figures 4.12b-h. It is seen that from the center region (P1) to the region near outer surface (P4), the amount of residual Cu gradually decreases from 50 to 8 at%. The chemical composition gradient from the region P1 to P4 is very apparent because the real or local leaching time increases gradually from position P4 to P1.

SEM image for the central region at a higher magnification is presented in Figure 4.12b. It shows that although a large fraction of residual Cu exists in the innermost region, the sample exhibits apparent nanoporous structure. The pores appear in two distinctly different types. One type of pores make up the space between interconnecting ligaments (type-II) and the other type of pores looks like small circular holes inside the ligaments (type-I). The same two types of pores are also very obviously seen in the images for the other three positions P2-P4 experiencing longer corrosion.

Figure 4.12b shows at P1 that type-I pore and solid strut have similar diameters (equal to the ligament sizes); the size of type-II pores is much bigger than solid struts. By contrast, at the most near outer surface region P4 undergoing the largest corrosion duration, a hierarchical nanoporous structure with two well-defined structure sizes is observed (Figures 4.12g-h), which is similar to the completely dealloyed sample's morphology (Figures 4.9a-b). The content of residual Cu at P4 is also comparable to a completely dealloyed sample. The morphologies at regions between P1 and P4 are also presented in Figures 4.12c-d for position P2 and in Figures 4.12e-f for position P3. Combine the microstructure at P1-P4, it indicates an increasing trend in the pore size of type-II pores with increasing real leaching time. Not only much larger type-II pores but also fewer type-I pores are observed at P4 in comparison to P3. This phenomenon is attributed to the coarsening effect induced by surface diffusion of Pd accompanying the whole dealloying process.

4.1.5 Structure coarsening by post thermo-annealing

Thermal annealing was performed on the as-prepared np-Pd samples that were obtained by dealloying $Cu_{85}Pd_{15}$ in 1.0 M H_2SO_4 at 60 °C. The annealing treatments were carried out at a high-vacuum atmosphere at three temperatures: 200, 300 and 400 °C, and all for 5 minutes. Figure 4.13 shows the fracture surface morphologies of annealed samples at three temperatures. It shows that the annealing treatments efficiently reduce the hierarchy, leading to a unimodal porous structure. With the same annealing duration, the structure size coarsens with increasing temperature. As the annealing temperature increases from 200 to 400 °C, the final ligament sizes of annealed samples increase from 80 to 270 nm. At an intermediate temperature 300 °C, the ligament size is around 120 nm.

Alternatively, using the electron beam heat from SEM, structure change of np-Pd during the coarsening process was inspected. The experiments were carried out in FEI Helios NanoLab G3 SEM in a high-vacuum condition. The accelerating power was 2 kV and 25 pA. The working distance was 1.9mm. Figures 4.14a-b show the SEM images of np-Pd before and after 12.5 min SEM beam heating. The heated region is marked by orange dash rectangular,

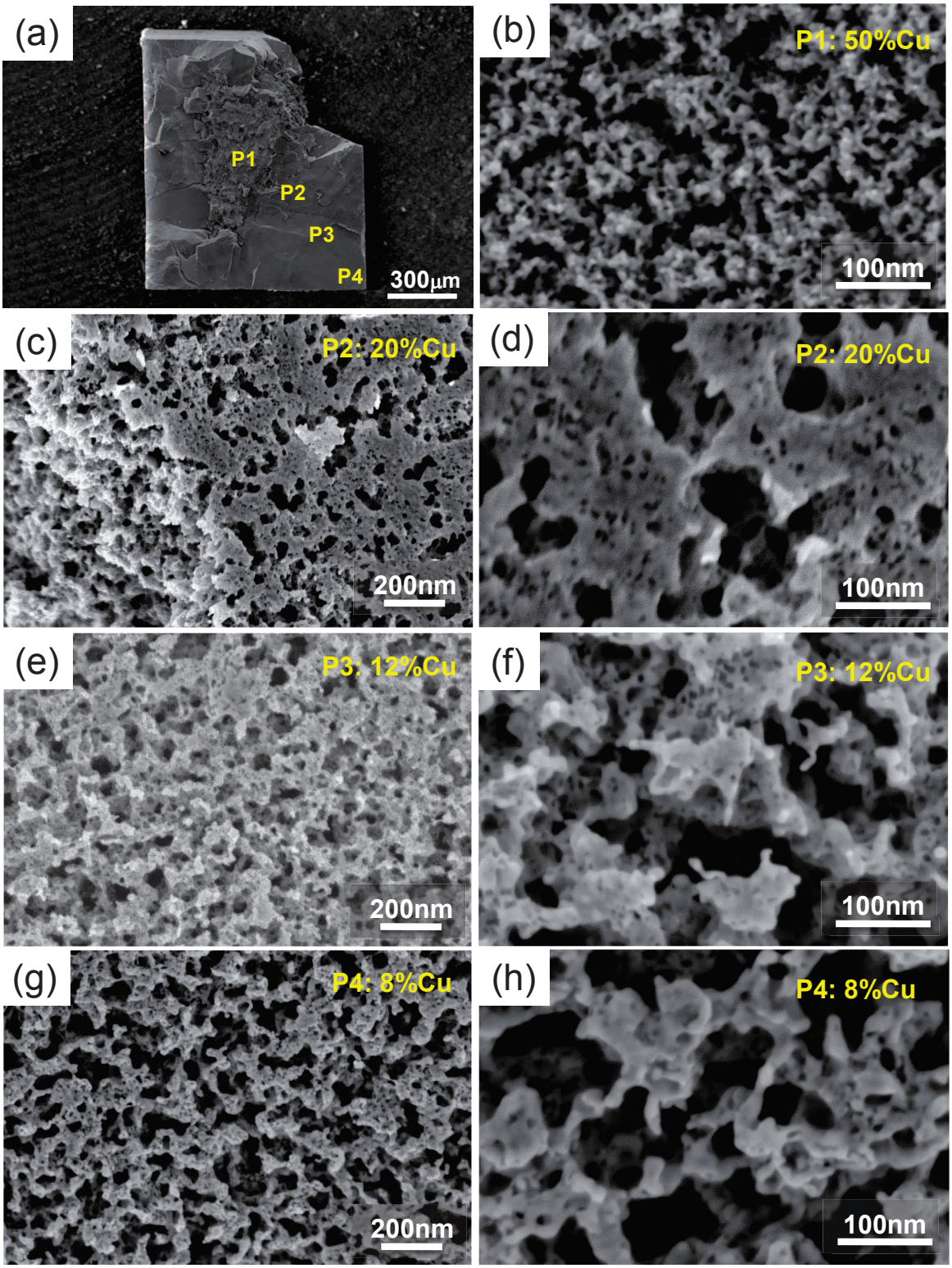

Figure 4.12: Cross-sectional analysis of a partially-dealloyed sample obtained by incompletely dealloying $Cu_{85}Pd_{15}$ master alloy in 1.0 M H_2SO_4 at 60 °C. (a) SEM images of fracture surface. (b-h) SEM images for four representative positions from Figure 4.12a. P1-4: from center to edge.

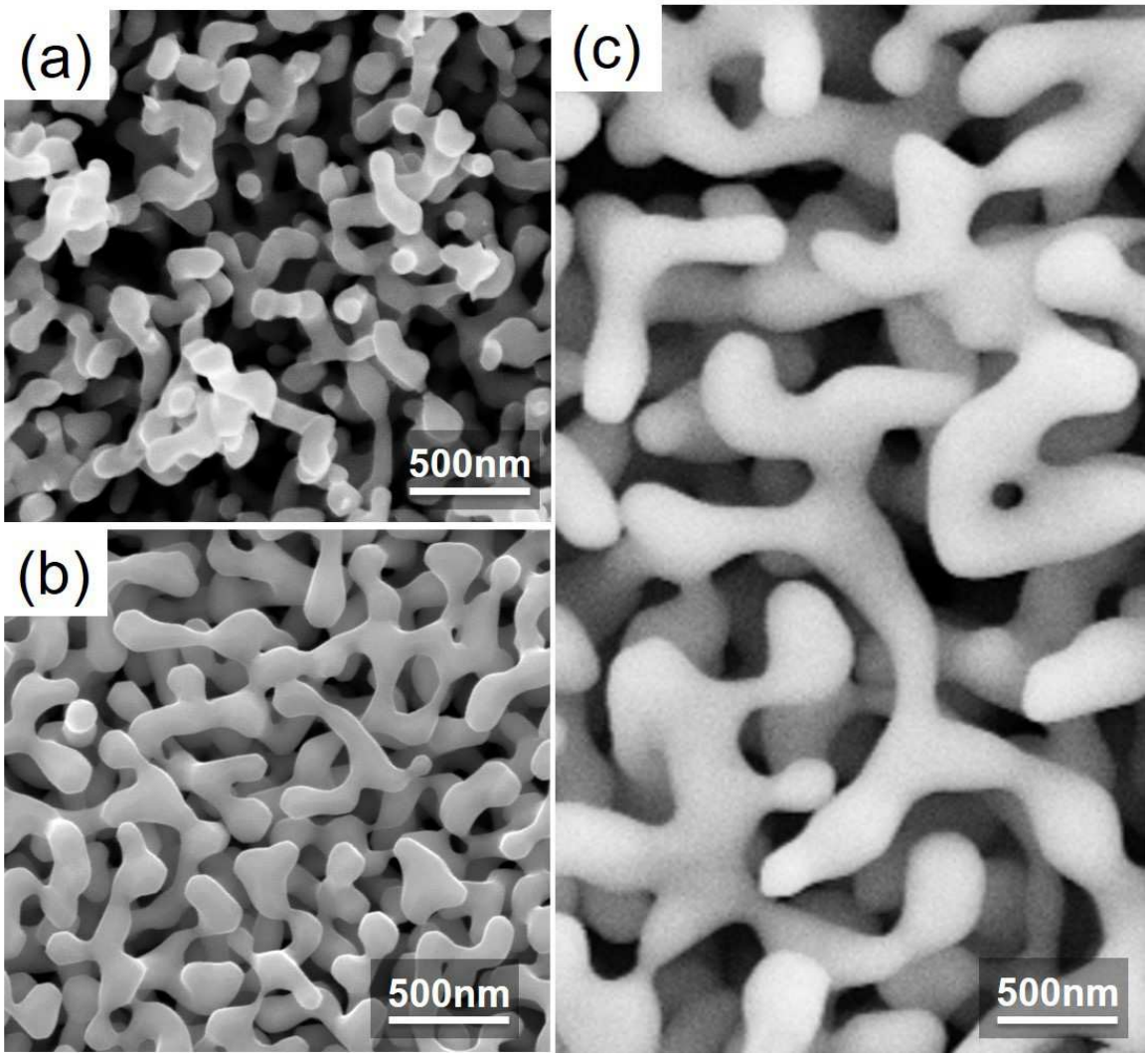

Figure 4.13: SEM images of np-Pd samples annealed at temperatures of (a) 200 °C, (b) 300 °C, (c) 400 °C for 5 min.

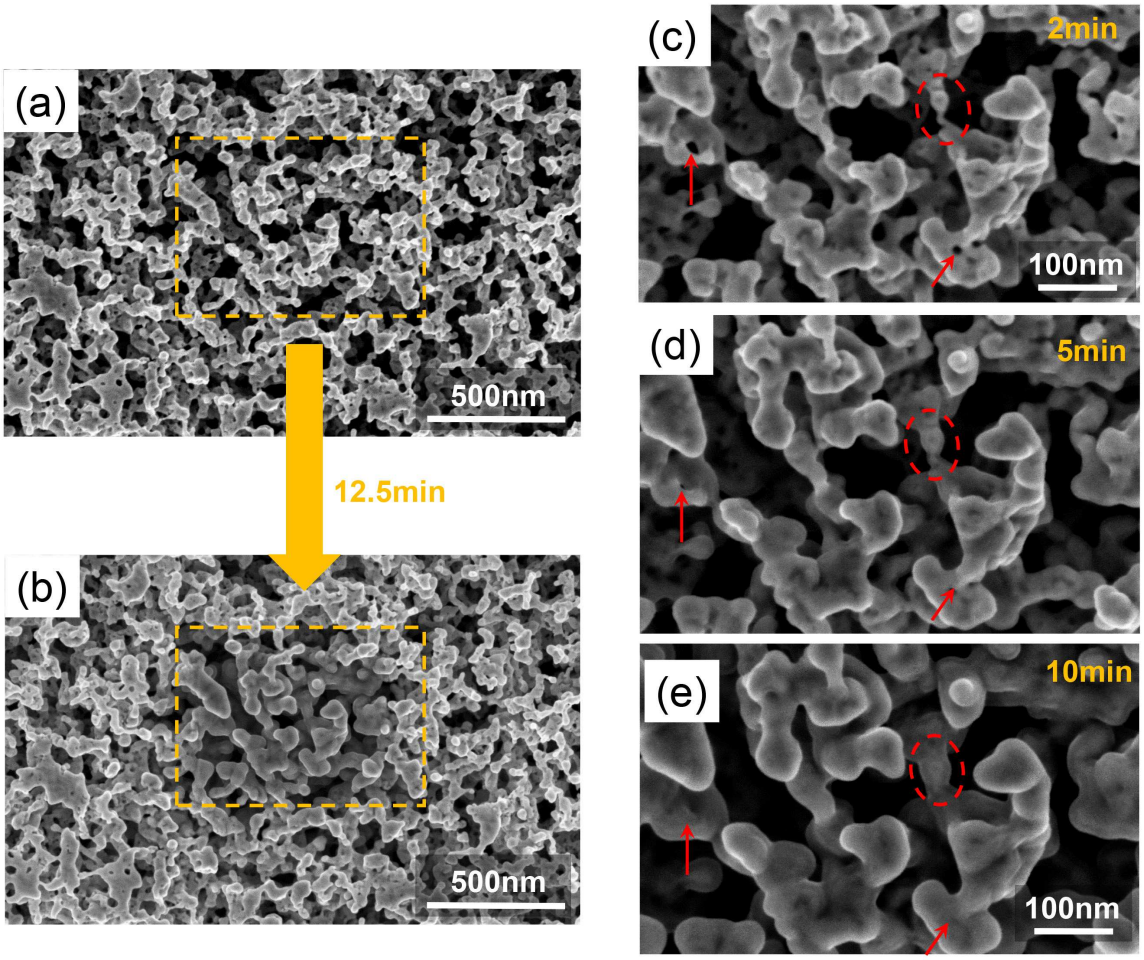

Figure 4.14: Morphology variation of hierarchical nanoporous palladium that was locally heated by SEM electron beam. (a) Starting material. (b) Sample locally heated for 12.5 min (heated area is marked with dot square). High resolution images of the same sample with heating durations of (c) 2 min, (d) 5 min and (e) 10 min.

indicating that in such short heating duration the fine hierarchical porous structure becomes much coarser and transforms into an monomodal porous structure. The morphologies for the same region undergoing different beam heating durations are displayed in Figures 4.14c-e. It is observed that as the heating time gradually increases from 2 to 10 min, the lower-level pores (marked by red arrows) gradually vanish and necks of ligaments (marked by red dash ellipse) gradually grow. The finally resulting monomodal porous structure is consistent with the results from thermal annealing in Figure 4.13.

4.2 Electrochemical characterization of nanoporous palladium

Cyclic voltammetry (CV) was applied on a bulk sample of as-prepared hierarchical nanoporous palladium that was fabricated by dealloying $Cu_{85}Pd_{15}$ alloy at 790 mV in 1.0 M H_2SO_4 at 60 °C. The details about this method were already described in Chapter 3. A further electrochemical reduction treatment ensures that as-prepared np samples contain 5 at% residues. Some properties like microstructure can be found in Section 4.1.3. If not specially pointed out, this kind of sample is always used in subsequent studies.

4.2.1 Electrochemical behavior of nanoporous palladium in sulfuric acid

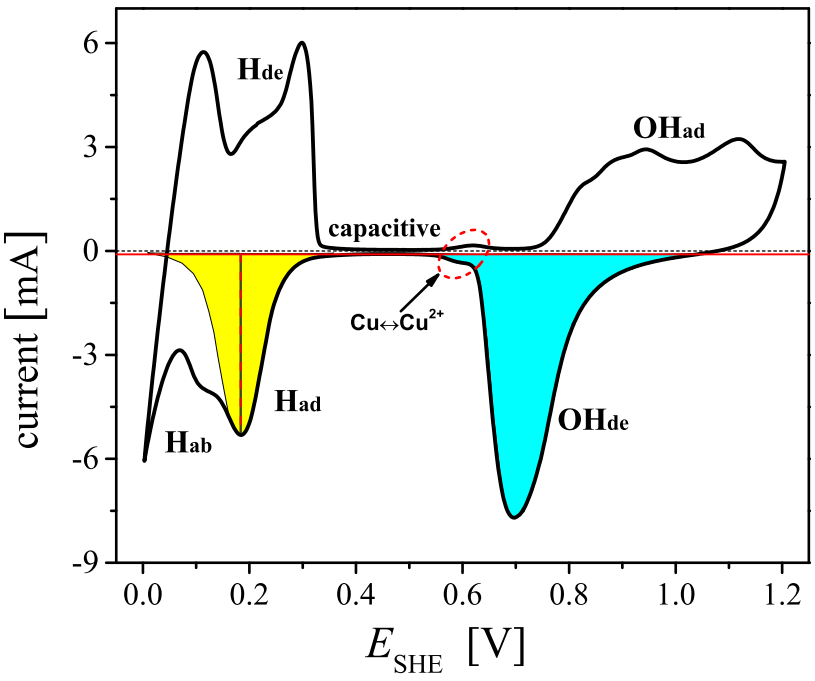

Figure 4.15: Cyclic voltammogram of np-Pd in 1.0 M H_2SO_4 aqueous solution at a scan rate of 10 mV/s at room temperature. H_{ad}: H adsorption, H_{ab}: H absorption, H_{de}: H desorption, OH_{ad}: OH adsorption, OH_{de}: OH desorption, $Cu \leftrightarrow Cu^{2+}$: Cu dissolution/redeposition. Yellow region: H absorption peak that predicted by mirroring the half part of UPD peak from more positive voltage to more negative voltage, blue region: Pd oxide reduction peak, black dashed horizontal line: zero current line, red solid horizontal line: capacitive current line (cathodic).

The CV measurements of np-Pd were carried out in 1.0 M H_2SO_4 electrolyte at room temperature. The potential window is 0-1.2 V. The potential scan rate is 10 mV/s. The resulting CV diagram is presented in Figure 4.15. The appearance is similar to the classic CV curve of nanostructured Pd materials in acids except the extra redox peaks at ~0.6 V, which are marked with a red dash ellipse in Figure 4.15. Similar extra redox peaks have already been observed elsewhere in the CV diagrams of np-PdCu alloys in acids [134–136]. Based on those analy-

sis, extra redox peaks near 0.6 V are supposed to be caused by Cu dissolution/redeposition. This explanation is also supported by the observations during electrochemical reduction of as-dealloyed sample in Figure 4.8: cyclic CV treatments gradually reduce the strength of the extra redox peaks near 0.6 V, leading to reduction of the Cu residue.

For convenience, CV diagram within the investigated potential window is roughly divided into three regions based on the main electrochemical reactions: hydrogen electrosorption at the low potential side, oxygen species adsorption/desorption at the positive side and in-between capacitive charging/discharging, as marked in Figure 4.15. In the hydrogen sorption regime, the cathodic peak at 0.18 V is caused by hydrogen surface adsorption (also called underpotential deposition, UPD); the cathodic peaks near 0.1 V and at more negative potentials are due to hydrogen bulk absorption; all the anodic peaks below 0.34 V correspond to desorption of hydrogen.

4.2.2 Determination of electrochemically active surface area

As described in Ref [138], there are several methods to measure materials' real surface in electrochemistry. For example, capacitance ratio method is popularly used for nanoporous Au; hydrogen adsorption from solution is mostly used for some transition metals. For palladium, capacitance ratio method is not a good choice because the pure capacitive region is too narrow to be separated from other reactions. Hydrogen adsorption approach is also seldom used because of the overlap between H surface adsorption peak and bulk absorption peak. Instead, oxygen adsorption from solution strategy is more often used for Pd. In this thesis, the later two methods were both used to determine electrochemically active surface area (A_{EASA}) of np-Pd electrodes.

In the oxygen species sorption regime, the electrochemical CV measurements in the current potential window (0-1.2 V) and scan rate (10 mV/s) generally oxidize only the monolayer of Pd electrode [136, 139]. Therefore, the cathodic peak near 0.7 V in Figure 4.15 caused by reduction of monolayer Pd oxide was used for determining electrochemically active surface area according to the following equation:

$$A_{\mathrm{EASA}} = Q/420[\mu\mathrm{C/cm^2}], \tag{4.2}$$

where $420[\mu\mathrm{C/cm^2}]$ is the charge for reducing PdO monolayer per unit area Pd [136, 139] and Q denotes charge associated with reducing Pd oxide monolayer on the electrode. Q is determined by current integration over time or potential:

$$Q = \int_0^t idt = 1/v \int_0^{vt} idE, \tag{4.3}$$

where $v = \frac{\mathrm{d}E}{\mathrm{d}t}$ denotes the potential scan rate. Here, it is 10 mV/s. Because the contribution by electric double layer needs to be subtracted in the calculation of charge integral for the Pd oxide reduction peak, the charge is calculated via dividing the area (blue region in the CV diagram) under the Pd oxide reduction peak by the scan rate. By carrying out tests on four samples, the average charge associated with the Pd oxide reduction peak normalized to the volume of solid phase is determined to be $737\,\mathrm{C/cm^3}$. A_{EASA} normalized by the volume of solid phase gives the surface-to-volume ratio $\alpha = 0.176\,/\mathrm{nm}$. A_{EASA} normalized by the mass of solid phase gives the mass-specific surface area $14.7\,\mathrm{m^2/g}$.

Similar to above estimation via oxygen adsorption strategy, hydrogen UPD near 0.18 V in Figure 4.15 is also analyzed. However, due to the overlap between UPD peak and bulk absorption peak, the UPD peak is separated by mirroring the half part of UPD peak from more positive voltage to more negative voltage. Using the same method for calculating charge for Pd oxide reduction, the area under that peak (yellow region in Figure 4.15) per scan rate is then used to estimate the charge caused by H UPD. This charge divided by sample's solid

volume yields 372 C/cm^3, which value is close to half of the volumetric charge associated with the Pd oxide reduction peak. Considering the two electrons are involved in the unit Pd oxide reduction reaction and one electron is involved in the unit H UPD reaction, the two approaches show consistent results.

4.3 Hydrogen-induced strain variation in nanoporous palladium

In this section, in-situ dilatometry measurements were carried out on bulk samples of hierarchical nanoporous palladium in 1.0 M H_2SO_4 at room temperature. The study concentrated on the hydrogen electrosorption region.

4.3.1 Coupling between strain and electrode potential

The potential step technique was used to enable hydrogen absorption/desorption processes to reach equilibrium. Guided by the results in Figure 4.15, a hydrogen-free state was achieved by equilibrating the sample at an arbitrary potential (E_c) in the capacitive region. Different potential-time programs were used for studying hydrogen ad/absorption and desorption branches. As shown in Figure 4.16a, a hydrogen absorption branch is explored by equilibrating sample at one potential of interest and then completely removing hydrogen always at E_c = 380 mV. Corresponding relative length change shows that during repeated potential cycles between -75 mV and E_c, sample shows cyclic expansion/contraction behaviors. Here, strain amplitude at the potential of interest is defined relative to hydrogen-free state E_c = 380 mV. For example, the strain amplitude for saturated absorption of hydrogen at -75 mV is 3.95%, as marked in Figure 4.16a. In the exploration of the hydrogen desorption branch, sample is always saturated with hydrogen at a very negative potential -75 mV before equilibrating sample at the potential of interest and E_c = 380 mV, as shown in Figure 4.16b. Similar to the strategy used for defining strain amplitude for desorption branch, strain amplitude at the potential of interest in the desorption branch is also defined relative to hydrogen-free state E_c = 380 mV, as marked in Figure 4.16b.

Figure 4.16c summarizes the strain amplitudes as a function of interested potentials in the range of 20-120 mV for both hydrogen absorption and desorption branches. In the absorption branch (solid line), strain amplitude shows a sharp increase from 47 to 42 mV. It indicates that the $\alpha \rightarrow \alpha'$ phase transition occurs in this narrow potential range. In the desorption branch (dot line), the inverse transition ($\alpha' \rightarrow \alpha$) takes place also in a narrow potential range, but this potential range is 5 mV more positive than the potential range for phase transition in the adsorption branch. This observation implies that a small hysteresis existed between hydrogen absorption and desorption. Inset schematic diagrams in Figure 4.16c illustrate that np-Pd expands when uptaking hydrogen and contracts when releasing.

To evaluate the kinetics of hydrogen adsorption/absorption activities at different potentials, half-time ($t_{1/2}$) is also used here. Different from the determination method used in evaluating corrosion rate (Figure 4.5b), here $t_{1/2}$ is determined as time required to reach half of the maximum strain during ad/absorption processes. As shown in Figure 4.17a, when H absorption takes place at the potential of -75 mV, the half-time is determined to be $t_{1/2}$ = 75 s. The values of $t_{1/2}$ for different potentials are summarized in Figure 4.17b. Within H UPD and H-diluted α regimes, $t_{1/2}$ is less than 10 s. By contrast, the valve of $t_{1/2}$ near phase transition increases up to more than 1000 s, which is two orders of magnitude larger than the values for H UPD and α-Pd-H phase regimes. It indicates that the kinetics for $\alpha' \rightarrow \alpha$ phase transition is extremely slow. At more negative potentials, the value of $t_{1/2}$ is observed to decrease with decreasing potentials which may due to the higher driving force for hydrogen absorption at more negative potentials, consistent with the examinations using Pd thin layers [140].

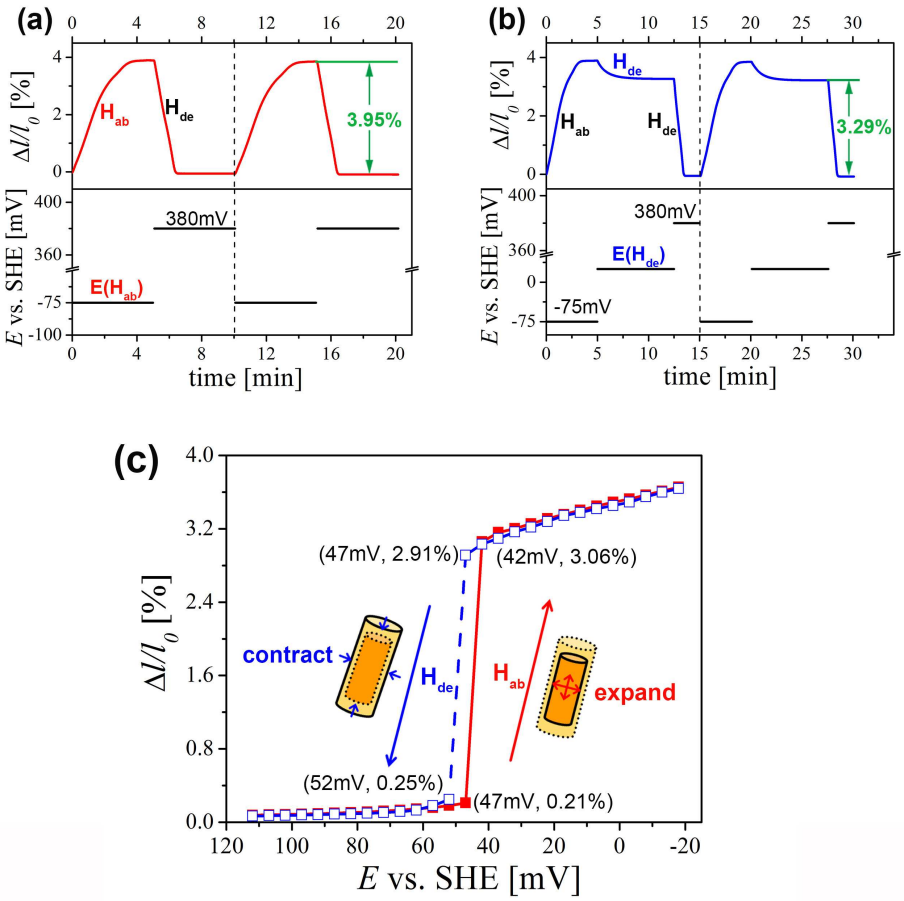

Figure 4.16: Potential- (E-) time programs together with resulting relative length variation ($\Delta l/l_0$) for studying hydrogen (a) *absorption* and (b) *desorption* branches. (c) Strain amplitude as a function of potential during hydrogen adsorption (red) and desorption (blue) branches. Inset in Figure 4.16c illustrates the expansion/contraction of one Pd ligament during absorption/desorption processes.

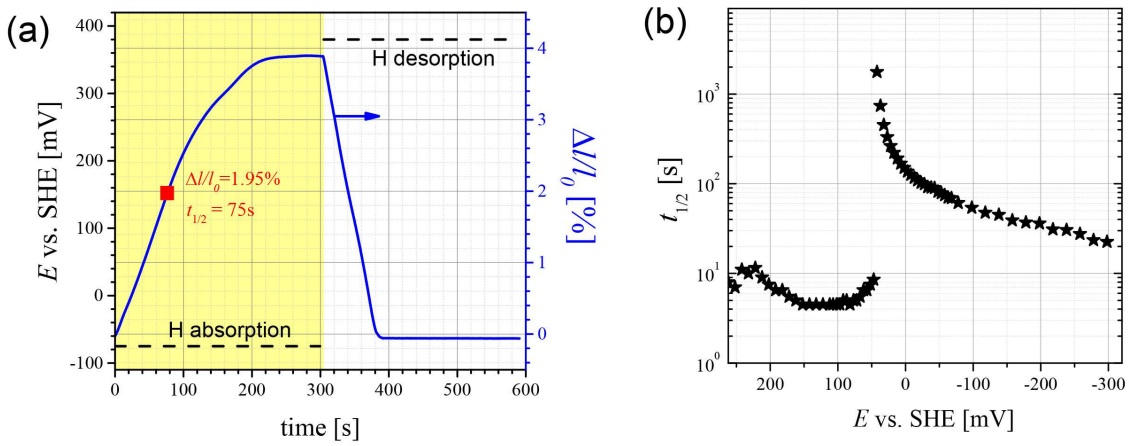

Figure 4.17: (a) Exemplary strain/potential- ($\Delta l/l_0/E$-) time protocol for determining half-time ($t_{1/2}$), (b) Summary of half time for hydrogen ad-/absorption at different potentials.

4.3.2 Coupling between strain and hydrogen fraction

On account of the low hysteresis during hydrogen absorption/desorption processes (Figure 4.16c), subsequent attention is on the hydrogen absorption branch. The protocol for investigating H absorption branch in Figure 4.16a is also employed in this section.

Determination of hydrogen fraction from charge

In this thesis, hydrogen fraction is defined as the molar ratio between hydrogen and metals. The number of metals (Pd and Cu) in mole for as-prepared np-Pd sample is calculated from its mass per the molar mass of solid phase $Pd_{95}Cu_5$. The molar mass of $Pd_{95}Cu_5$ is roughly predicted by using a general rule of mixtures and using molecular masses of constituent elements.

According to Faraday's law of electrolysis, the number of hydrogen (n_{H}) in mole can be calculated from accumulated charge (Q_H) during H electrosorption process via $n_H = Q_H/\mathrm{F}$. However, the charge obtained by current integration can be inaccurate especially at very negative potentials when hydrogen evolution occurs and generates current. This influence is minimized in the desorption run, therefore, the integration of current from the desorption process is preferable to that from absorption processes in subsequent studies.

Determination of the onset of hydrogen underpotential deposition

Note that the hydrogen-free potential 380 mV is in the capacitive region. The current used for charge integral in the desorption run is actually contributed by two parts: capacitive charging and hydrogen desorption. Therefore, it is meaningful to determine the onset potential (E_0) of hydrogen adsorption or H UPD for the estimation of net hydrogen fraction.

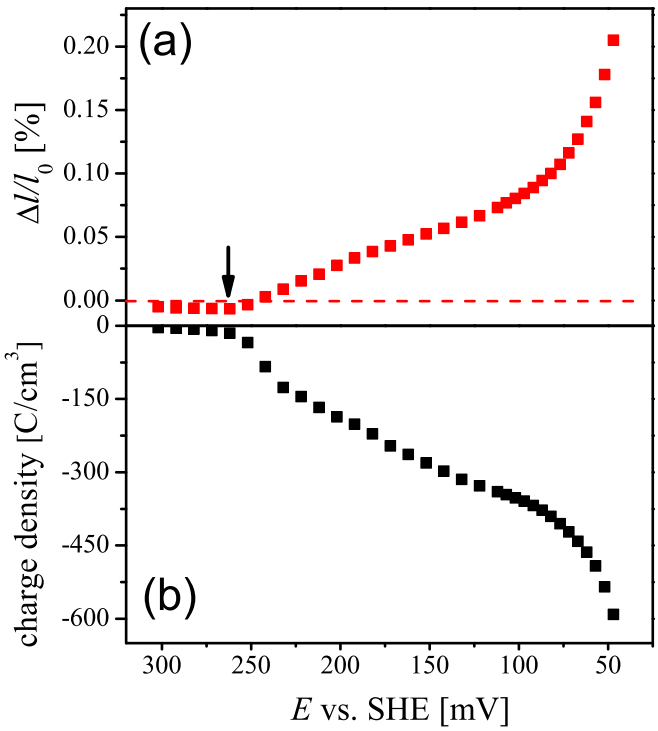

Figure 4.18: (a) Strain amplitude ($\Delta l/l_0$) versus electrode potential (E), (b) Integrated charge density (charge per sample volume) versus electrode potential. Arrow symbolizes the onset potential of hydrogen adsorption, E_0.

Figure 4.18 shows the strain amplitude and charge density in response to electrode potential within the hydrogen-diluted regime. Both the strain amplitude and charge density at each potential in the diagram are determined relative to the equilibrated state at E_c = 380 mV. The scale of horizontal axis in the Figure starts from the most positive potential where the sample contains H. Starting from most positive potential in the capacitive regime, the strain amplitude is observed to slightly decrease with decreasing potential until 262 mV. At potential below 262 mV, strain amplitude increases with negative-going potentials denoting the onset of H UPD and then bulk absorption at more negative potentials. The charge, which is calculated by integrating current over time per volume, is displayed in Figure 4.18b. It almost mirrors the trend of strain amplitude in Figure 4.18a, especially much deeper slope potentials <262 mV. Therefore, E_0 = 262 mV is determined as the onset potential of H UPD. The state of the sample equilibrated at E_0 = 262 mV is set as the lower limit of the net hydrogen fraction, $x_{\mathrm{H}}^{\mathrm{net}} = 0$. Note that the net hydrogen fraction $x_{\mathrm{H}}^{\mathrm{net}}$ includes UPD H on the surface and absorbed H in the bulk.

Hydrogen solubility

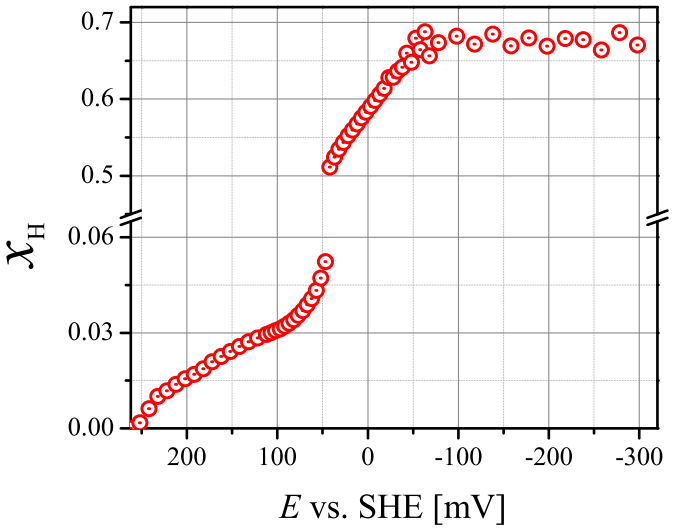

Figure 4.19: Net hydrogen fraction ($x_{\mathrm{H}}^{\mathrm{net}}$) versus electrode potential (E). Note a scale break on the vertical axis.

Figure 4.19 shows the net hydrogen fraction for samples equilibrated at different potentials. It is observed that hydrogen fraction firstly increases with decreasing potential and reaches to the maximum value $x_{\mathrm{H}}^{\mathrm{net}} = 0.67 \pm 0.01$ at -53 mV. As potential further decreases, $x_{\mathrm{H}}^{\mathrm{net}}$ maintains at the maximum value due to the saturation of hydrogen absorption. Consistent with the observation in Figure 4.16c, the phase transition from α to α' is also clearly resolved here from the sharp jump of hydrogen fraction in the narrow potential window E = 47−42 mV. In the α phase regime, the H solubility reaches $x_{\mathrm{H}}^{\mathrm{net}} = 0.052$ (a sum of UPD H and absorbed H) at E = 47 mV.

Strain-concentration coupling coefficients

The coupling between composition and strain is quantified by the strain-concentration coefficient, $\eta = l_0^{-1}\partial l/\partial x_{\mathrm{H}}^{\mathrm{net}}$. In order to assess the values of η, strain amplitudes for the sample equilibrated at different potentials are taken relative to the state at E_0. The resulting strain amplitude and corresponding hydrogen net fraction are summarized in Figure 4.20. It is

apparent that the strain-concentration slopes at very low hydrogen fractions and at high hydrogen fractions are different. This is nothing surprised. Different electrocapillary coupling coefficients between H UPD on the surface and H absorption in the subsurface have already been reported by Viswanath *et al.* [90]. Therefore, strain-concentration data for the surface adsorption region and bulk absorption region is straight-line fitted separately. With respect to bulk absorption, the fitted result for the data including α and α' is displayed by a red line with a slope of $\eta = 0.0616 \pm 0.0001$. The dilute α part is enlarged and shown as an inset, in which the experiment data also shows good agreement with the fitted line. This agreement demonstrates a constant strain-concentration coefficient for the whole composition range in the bulk absorption regime.

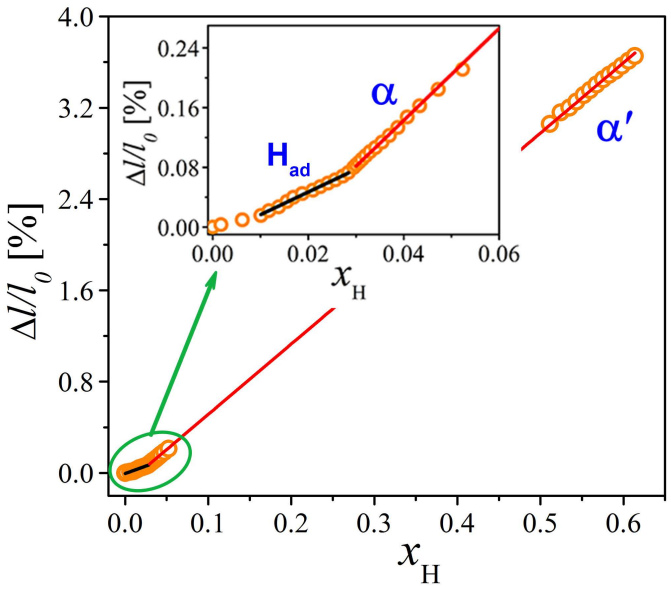

Figure 4.20: Equilibrium strain ($\Delta l/l_0$) as a function of net hydrogen fraction (x_H^{net}). Black and red lines denote linear fitted curves for data in the surface adsorption regime and in the bulk absorption regime, respectively.

The same kind of evaluation is done separately with six samples, yielding an average value $\eta = 0.060 \pm 0.002$. The good agreement with literature results $\eta = 0.063 \pm 0.003$ from Ref [72, 90] validates the accuracy of the in-situ dilatometry. Apart from the bulk absorption regime, a linear fitting is also done in the H UPD regime excluding data at the most positive potentials in order to avoid contributions from capacitive charging. The results are displayed in Figure 4.20, exhibiting a smaller slope $\eta = 0.0303 \pm 0.0006$. This denotes H surface adsorption has a smaller strain-concentration coefficient than H bulk absorption.

Determination of the onset of hydrogen bulk absorption

The different strain-concentration coefficients for surface adsorption and bulk absorption are in turn used as one basis for separating H UPD and H-diluted α phase. In the inset of Figure 4.20, the two fit lines for surface adsorption and bulk absorption intersect at $E = 0.13\,\mathrm{V}$ and $x_H^{net} = 0.029$, which correspond to the onset potential of H bulk absorption and total amount of H UPD contribution.

4.3.3 Hydrogen-assisted actuation with nanoporous palladium

Hydrogen-induced reversible strain variation with np-Pd was used as the actuation mechanism. In-situ dilatometer setup was used for characterizing actuation performances. Guided

by the results from Figure 4.16 and Figure 4.17, absorption of H was carried out at a very negative potential aiming for a large stroke and a fast response; desorption of H was realized by equilibrating sample at a potential selected from the capacitive regime.

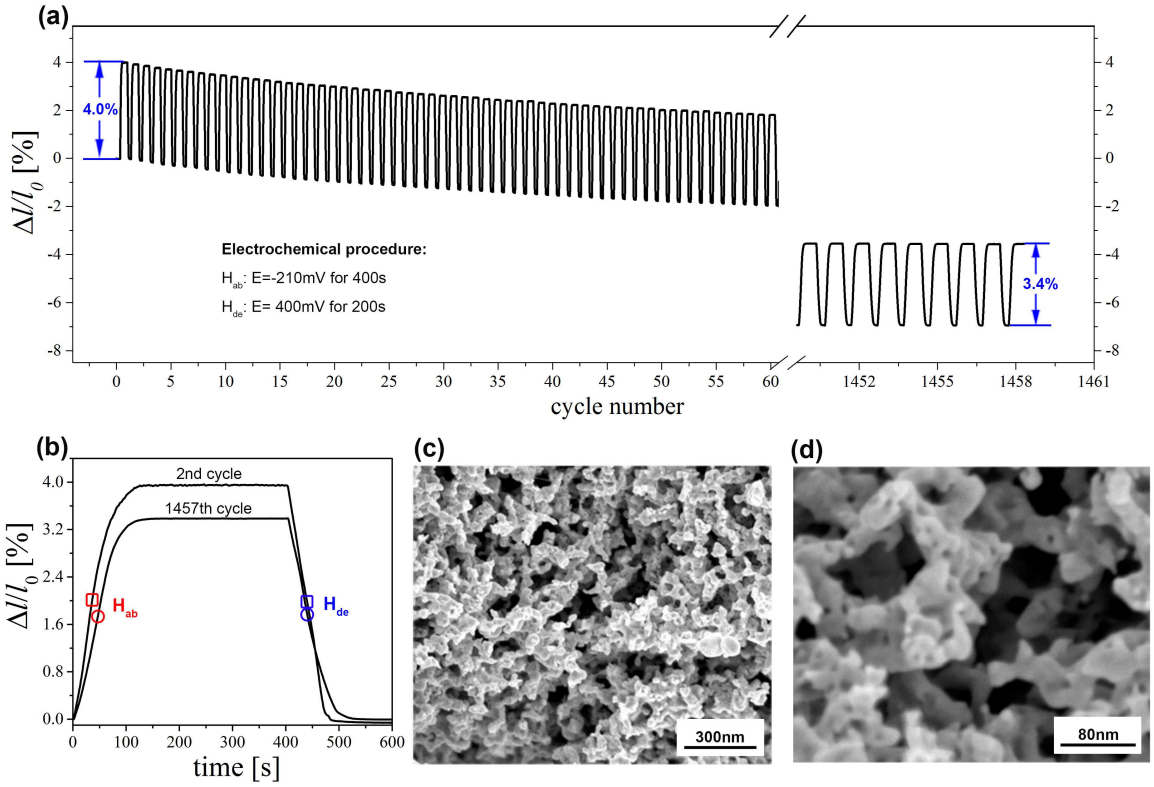

Figure 4.21: Evaluation of hydrogen-assisted actuation with np-Pd in 1.0 M H_2SO_4. (a) Strain variation ($\Delta l/l_0$) during long-term repeated absorption/desorption cycles by alternately switching potential between -210 mV for 400 s and 400 mV for 200 s, (b) Strain-time curves for the 2nd and 1457th cycles (open symbols highlighted on the curves denote half-time), (c-d) SEM images of np-Pd after the long-term cycling test in Figure 4.21(a).

Hydrogen absorption/desorption in np-Pd were repeatedly cycled via switching potential alternatively between -210 mV (duration: 400 s) and 400 mV (duration: 200 s). The test was carried out in 1.0 M H_2SO_4 at room temperature. More than 1000 cycles were applied during 10 days. Corresponding strain variation with time was monitored by in-situ dilatometer. As is shown in Figure 4.21a, at the beginning of the long-term test, the strain amplitude is as high as 4.0% (peak-to-peak). At the end of the test, the strain amplitude still remains 3.4%. It is also observed that np-Pd gradually shrinks during the entire test. The contraction is more significant at the early stage and becomes less obvious at the latter cycles. In total, an irreversible shrinkage of 7.0% is observed at the end of the test.

The strain variation and half-time for the 2nd and 1457th cycles are displayed in Figure 4.21b. It is seen that the half-time for hydrogen absorption and desorption in the second cycle is 36 and 41 s, respectively. No significant change in half-time is observed after more than 1000 cycles. In order to characterize the stability of the sample, the microstructure after the above long-term test was analyzed. Figures 4.21c-d show the fracture surface morphologies of np-Pd before and after the test . Slight differences such as decrease of the amount of pores and increase of ligament size at the lower hierarchy level are observed between the long-term cycled sample and the as-prepared sample (Figures 4.9c-d). The ligament size at the upper hierarchy level still remains around 35 nm.

4.4 Hydrogen-induced elasticity variation in nanoporous palladium

The studies in this section used the same type of np-Pd and electrolyte as the studies in Sections 4.2 and 4.3, but the interest was restricted to hydrogen bulk absorption/desorption processes. In-situ dilatometer setup was preferred in Section 4.4.1 for obtaining potential-composition isotherms of the palladium-hydrogen system and in-situ DMA setup was preferred in Section 4.4.2 for studying the variation of the elastic properties of np-Pd-H with hydrogen fraction.

Setting reference state Distinguished from the net hydrogen fraction ($x_{\mathrm{H}}^{\mathrm{net}}$), the interstitial hydrogen fraction excluding the UPD H is denoted as x_{H}. The value of x_{H} is estimated from hydrogen-induced strain variation, taking the average strain-concentration coefficient (η = 0.06) that is determined in Section 4.3.2. The equilibrated state at the onset potential of bulk absorption (E = 0.13 V), where np-Pd is saturated with UPD H layer at the surface but has zero hydrogen in the bulk, is chose as the reference state for x_{H} = 0 and for Young's modulus normalization.

4.4.1 Hydrogen solubility isotherms and solute susceptibility

Apart from the potential step strategy in Figure 4.16, low-scan rate cyclic voltammetry is also one good strategy to study hydrogen sorption near equilibrium. Figure 4.22 summarizes electrode potential versus absorbed hydrogen fraction obtained with these two strategies. Results from the cyclic voltammetry approach at three different scan rates and from the potential step approach are indicated by legends (0.03 mV/s: black; 0.015 mV/s: red; 0.005 mV/s: blue; potential step: dark green). The potential step approach affords more time for hydrogen sorption at a given potential to reach equilibrium state. All curves show obvious phase transition plateau and hysteresis, but the hysteresis gradually reduces with decreasing potential scan rates. Superimposed curves are observed at different scan rates within hydrogen-diluted α phase region. This is mainly due to the fast equilibration in the H-diluted region, which is also supported by the short half-time for hydrogen absorption within the α-H-Pd regime (see Section 4.3.1).

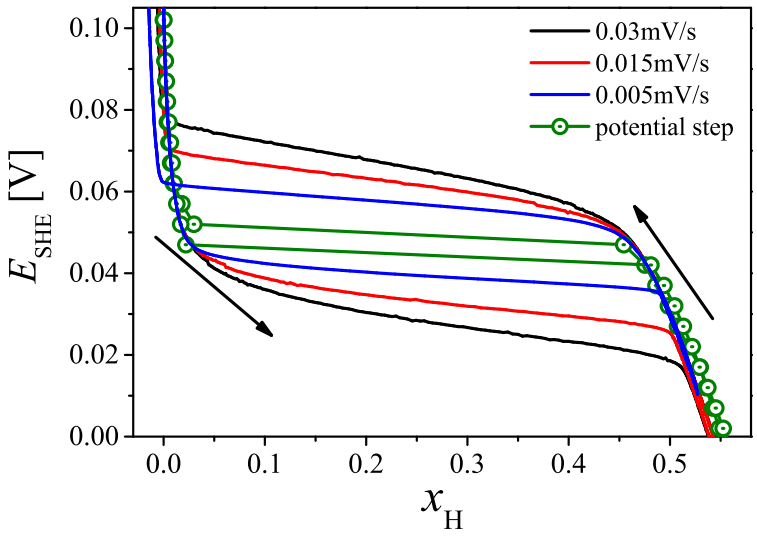

Figure 4.22: Electrode potential- (E_{SHE}-) composition (x_{H}) isotherms of hydrogen in np-Pd at 298 K.

The data from the lowest scan rate 0.005 mV/s in Figure 4.22 is used for estimating

chemical potential, μ_H, and solute susceptibility, χ, according to the following equations:

$$\mu_H = -FE_{SHE}\,, \tag{4.4}$$

$$\chi = \frac{1}{\rho_0}\frac{dx_H}{d\mu_H}|_{Stress} \tag{4.5}$$

with E_{SHE} - electrode potential (versus SHE),x_H - hydrogen fraction and ρ_0 - atomic number density of $Pd_{95}Cu_5$. The calculation for μ_H and χ is restricted to the hydrogen-diluted α phase regime, because the inhomogeneity caused by phase transition limited the evaluation in H more concentrated regimes. Chemical potential as a function of hydrogen fraction is presented in Figure 4.23a. It shows that the chemical potential increases with hydrogen fraction and reaches to μ_H = -5 kJ/mol at x_H = 0.02. Also shown in Figure 4.23a is a well fit curve (red line) obtained via 6th order polynomial fitting μ_H against ln(x_H). This fitted μ_H-x_H curve is then used to estimate χ according to Equation 4.5. Solute susceptibility (χ) as a function of hydrogen fraction is displayed in Figure 4.23b. It shows that χ also increases with hydrogen fraction within the H-diluted region and reaches to χ = 100 TPa^{-1} at x_H = 0.02.

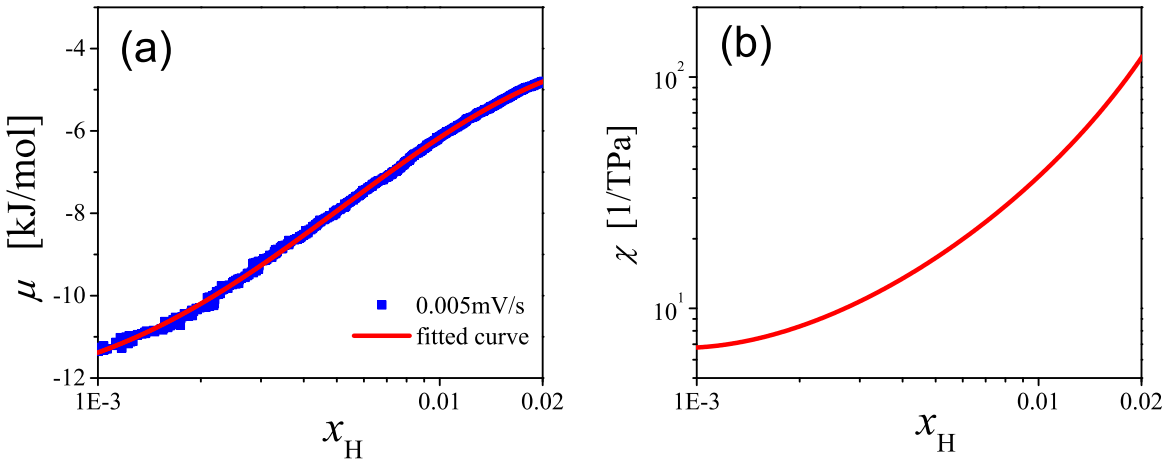

Figure 4.23: (a) Chemical potential (μ_H) versus bulk hydrogen fraction (x_H) within the H-diluted regime (x_H <0.2). (b) Solute susceptibility parameter (χ) as a function of x_H in the H-diluted region.

4.4.2 Open-system elasticity measured by in-situ dynamic mechanical analysis

In-situ dynamic mechanical analysis (DMA) set-up was used to analyze the variation of mechanical properties of np-Pd during hydrogen electrochemical absorption/desorption processes. During imposing cyclic potentials (between 0.12 and 0.02 V) on np-Pd, cyclic variations of relative length change ($\Delta l/l_0$, red), effective Young's modulus (Y^{eff}, blue) and loss modulus (Y^{eff}_{loss}, green) were recorded by in-situ DMA.

Figure 4.24 shows the mechanical responses during one potential cycle at a scan rate of 0.1 mV/s. The two-phase coexisted regions during both absorption and desorption branches are shaded. In the whole range, the value of Y^{eff}_{loss} is much smaller than that of Y^{eff}. In the hydrogen absorption run, as the applied potential sweeps from 0.12 to 0.02 V, the relative length change of np-Pd sample gradually increases with time due to a continuous hydrogen absorption reaction. In the subsequently reverse potential scan, the length gradually returns to the initial value due to the desorption of hydrogen. This length variation with electrode potential is consistent with the previous observation by using in-situ dilatometer setup in Section 4.3.

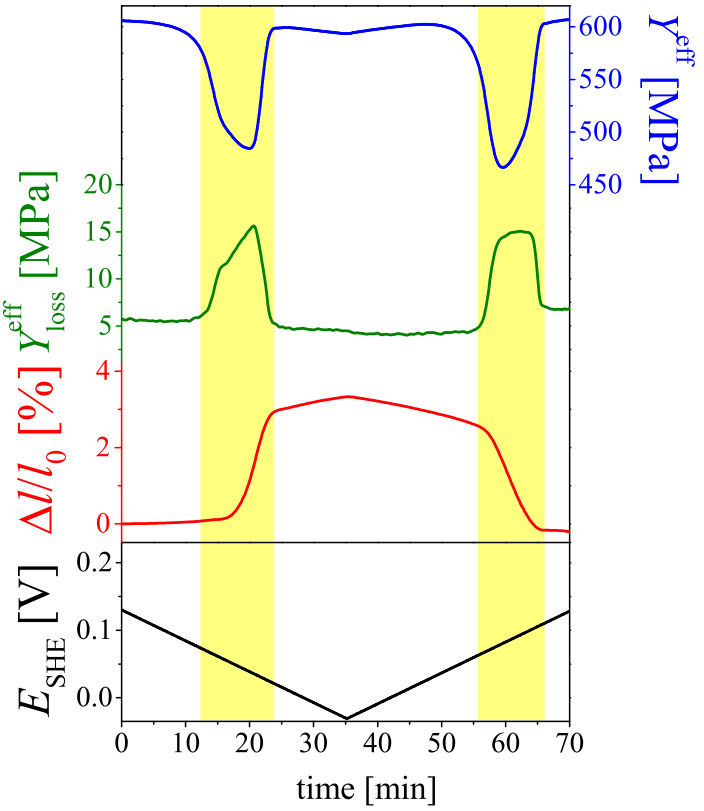

Figure 4.24: Variation of relative length change ($\Delta l/l_0$), effective Young's modulus (Y^{eff}) and loss modulus ($Y^{\text{eff}}_{\text{loss}}$) with time during one potential cycle between 0.12 and 0.02 V at a scan rate of 0.1 mV/s. Frequency of dynamic strain: 1 Hz. Yellow region: the two-phase coexisted regime.

Influence of dynamic strain amplitude

Figure 4.25 shows the influences of dynamic strain amplitude (ε_{dy}) on loss modulus ($Y^{\text{eff}}_{\text{loss}}$), effective Young's modulus (Y^{eff}), and relative hydrogen fraction (Δx_{H}) during six CV cycles. The dynamic strain peak-to-peak amplitude is 0.4% in the first 2 cycles, 0.6% in the middle 2 cycles and 0.8% in the last 2 cycles. Figure 4.25 indicates that in the investigated potential range, all the variations of loss modulus, Young's modulus and hydrogen fraction are independent on the dynamic strain amplitude.

Influence of frequency of dynamic strain

The influences of frequency of dynamic strain on effective Young's modulus and loss factor were explored with np-Pd containing different hydrogen fractions. The H fraction in np-Pd was adjusted by holding samples at various potentials. Three potential values were selected as representatives. Hydrogen absorption at these potentials lead to two α phases with different hydrogen fractions and one α' phase with substantially larger hydrogen fraction. Figure 4.26a shows that different Young's modulus values are observed in np-Pd equilibrated at different absorption potentials. In the range of 0.1 to 100 Hz, it is found that the variations of Y^{eff} with frequency are less than 1.4%, irrespective of x_{H}. Figure 4.26b shows the influence of frequency of dynamic strain on loss factor ($\tan\,\delta = Y^{\text{eff}}_{\text{loss}}/Y^{\text{eff}}$, corresponds to the ratio between loss modulus and effective Young's modulus), of np-Pd-H that have different hydrogen fractions and dry np-Pd that contains no hydrogen. In the whole frequency range, the loss factors of dry np-Pd are very low, less than 1.5%. For np-Pd-H, in the frequency range of 0.1 to 10 Hz, the loss factors are similar to that of np-Pd, irrespective of hydrogen fraction, but when the frequency is more than 10 Hz, the loss factors of all these np-Pd-H materials increase with

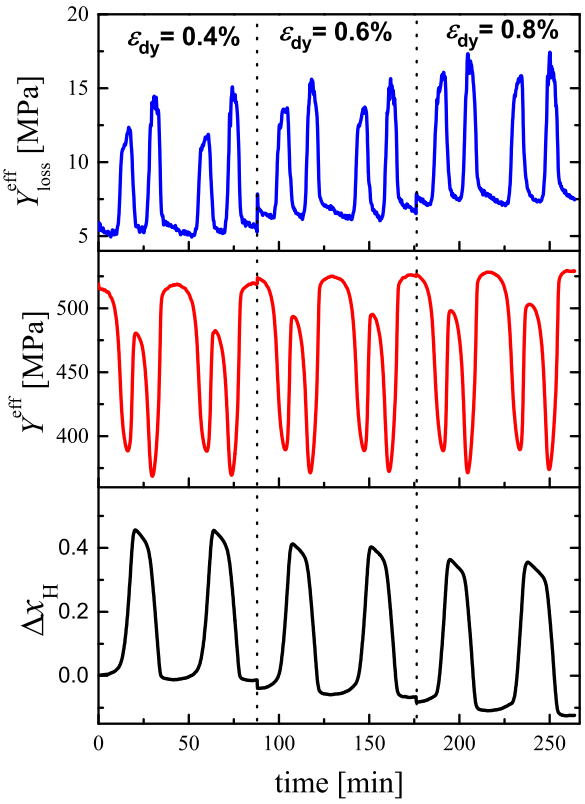

Figure 4.25: Influences of dynamic strain amplitude (ε_{dy}) on loss modulus (Y^{eff}_{loss}), Young's modulus (Y^{eff}), relative hydrogen fraction (Δx_H) during six potential cycles at a scan rate of 0.1 mV/s. Frequency of dynamic strain: 3 Hz.

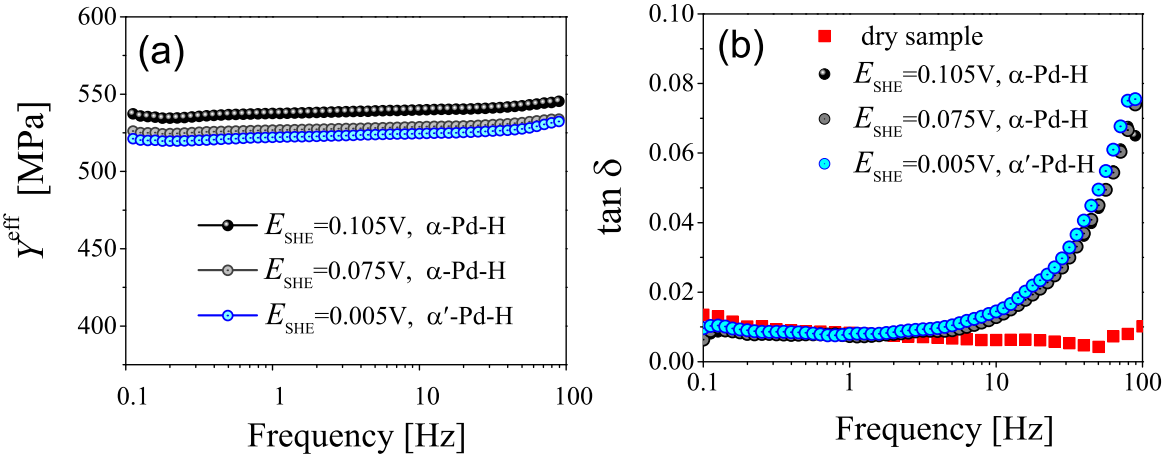

Figure 4.26: Influences of frequency of dynamic strain on (a) effective Young's modulus (Y^{eff}) and (b) loss factor (tan δ, corresponds to the ratio between loss modulus and effective Young's modulus) of np-Pd at different electrode potentials (E_{SHE}) in electrolyte. Also shown in (b) is the influence of frequency of dynamic strain on tan δ of dry np-Pd in air.

increasing frequency.

Influence of potential scan rate

With the same strategy displayed in Figure 4.24, the influence of potential scan rate on H-induced elasticity was also explored. Young's modulus normalized to the reference state ((here reference state is at $E = 0.13\,\mathrm{V}$, $Y^{\mathrm{eff}}/Y_0^{\mathrm{eff}}$) is plotted against interstitial hydrogen fraction (x_{H}), as shown in Figure 4.27a. It is seen that normalized Young's modulus varies with hydrogen fraction, independent on the scan rate (0.2 mV/s: black; 0.1 mV/s: red; 0.03 mV/s: blue). In the hydrogen absorption run, as hydrogen fraction increases, normalized Young's modulus shows a sharp drop in the narrow hydrogen-diluted region and becomes stiff again when running into hydrogen-concentrated region. In the desorption run, the variation of $Y^{\mathrm{eff}}/Y_0^{\mathrm{eff}}$ with x_{H} exhibits the same overall trend. Yet, in the middle region, the $(Y^{\mathrm{eff}}/Y_0^{\mathrm{eff}})$-$x_{\mathrm{H}}$ curve appears quantitatively different between the absorption run and desorption run. Remarkably, hydrogen absorption results in over 20% decrease in the Young's modulus. Additionally, the closed graph implies that the elastic behavior can return to initial state after one entire absorption/desorption cycle.

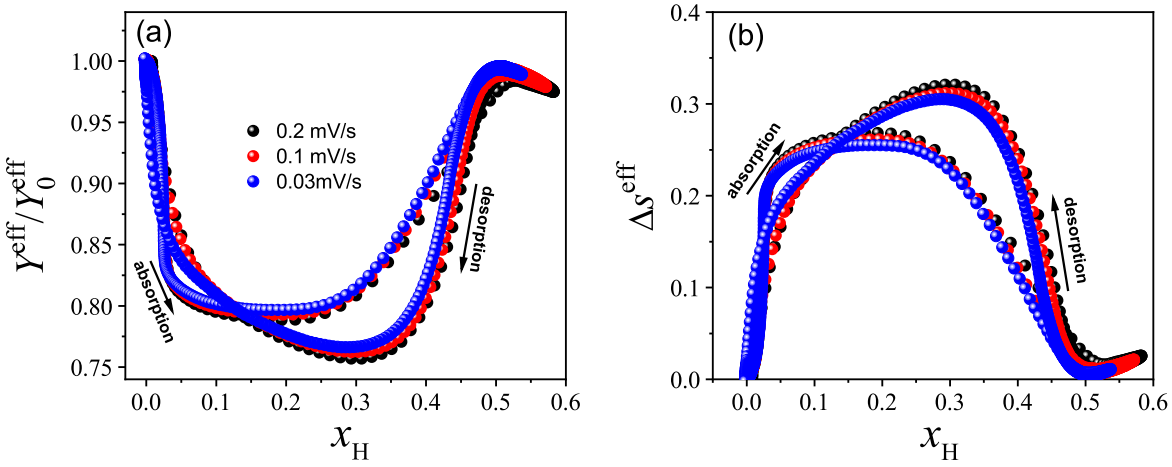

Figure 4.27: Influence of potential scan rate on H-induced elasticity variation of np-Pd-H. (a) Normalized Young's modulus ($Y^{\mathrm{eff}}/Y_0^{\mathrm{eff}}$) versus hydrogen fraction, (b) Relative compliance change (Δs^{eff}) versus hydrogen fraction (x_{H}). Frequency of dynamic strain: 1 Hz.

Figure 4.27b shows the relative compliance change, $\Delta s^{\mathrm{eff}} = \frac{Y_0^{\mathrm{eff}}}{Y^{\mathrm{eff}}} - 1$, versus hydrogen fraction at different scan rates. The relative compliance change is also irrespective of scan rate. It is remarkable that H-electrosorption leads to more than 30% increase in the relative compliance change.

As mentioned above, the potential step method could afford more time for hydrogen sorption to reach equilibrium than the low-scan CV method. Therefore, the potential step method was also used to confirm the conclusion derived from Figure 4.27: the variation of normalized Young's modulus with hydrogen fraction is independent on the scan rate. In-situ DMA measurements were performed on np-Pd during switching potential between 0.107 V, a potential near reference state, and various potentials below 0.107 V. The potentials were always held until the length expansion or contraction reached a steady state. Taking H sorption kinetics (see half-time displayed in Figure 4.16c) into account, the investigations focused on α-Pd-H phases which have fast H absorption kinetics. Figure 4.28a shows the potential-time procedures and the variation of normalized Young's modulus (here normalized to the state at 0.107 V). In the investigated potential range, the value of Young's modulus decreases with decreasing potential and returns to the initial value when the potential returns to $E = 0.107\,\mathrm{V}$. This observation is nothing surprised because the previous work has demonstrated that the

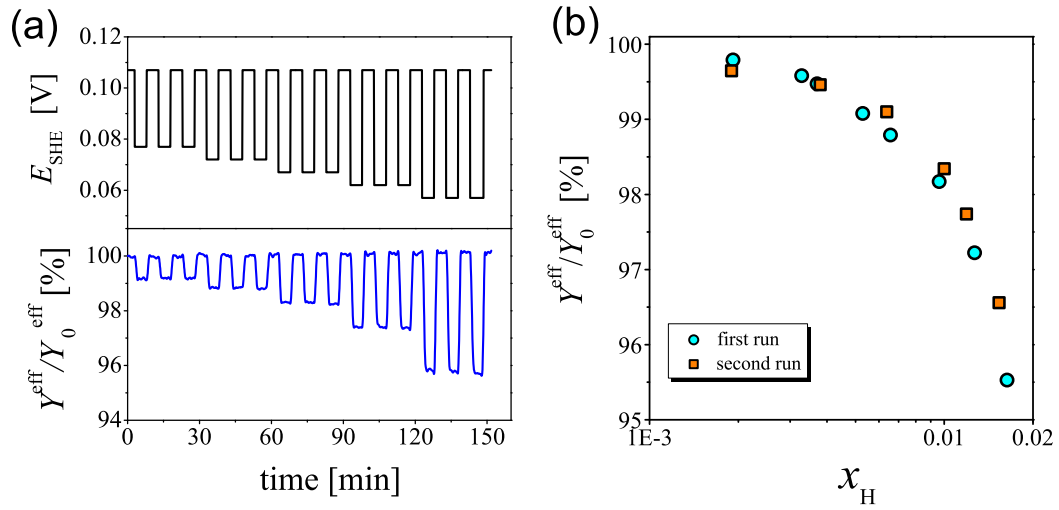

Figure 4.28: (a) Normalized Young's modulus ($Y^{\text{eff}}/Y_0^{\text{eff}}$) variation during potential steps. (b) Normalized Young's modulus versus hydrogen fraction (x_{H}) within the H-diluted regime. Frequency of dynamic strain: 1 Hz.

hydrogen fraction can be controlled by the electrode potential, see Figure 4.19. Two separate in-situ DMA tests were carried out on one np-Pd sample. The resulting normalized Young's modulus is plotted against hydrogen fraction in Figure 4.28b. The results obtained from these two tests are consistent and are in good agreement with the one obtained by using low-scan CV methods in Figure 4.27a.

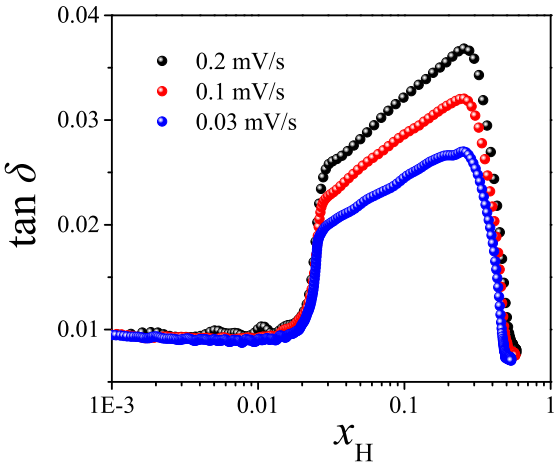

Figure 4.29: Influence of potential scan rate on loss factor (tan δ). Frequency of dynamic strain: 1 Hz.

Loss factor, $\tan\delta = Y_{\text{loss}}^{\text{eff}}/Y^{\text{eff}}$, which corresponds to the ratio of loss modulus and effective Young's modulus, is also plotted against x_{H}. The results for hydrogen absorption at three potential scan rates are showed in Figure 4.29. A small loss factor (1%) is observed in H-diluted α phase ($x_{\text{H}} < 0.02$) and H-concentrated α' phase ($x_{\text{H}} > 0.5$) regimes, regardless of scan rates. Moreover, the loss factors of single-phases α and α' are very comparable to that of the dry np-Pd sample in Figure 4.26b. By contrast, in the miscibility gap, a much larger loss factor is observed and increases with increasing potential scan rates. This behavior may be due to less time for phase transition at faster scan rates which leads to more heterogeneous samples. Based on the difference in loss factor between two-phase and single-phase regions,

the regions for α, α' and in-between two-phase are very well distinguished.

4.5 Hydrogen-induced elasticity variation in nanoporous palladium-gold

In last section, hydrogen-induced open-system elasticity variations were explored with monolithic np-Pd samples. However, the comparison of open-system elasticity between experimental and Larché-Cahn theory prediction is restricted to single α phase for np-Pd, which has a very low hydrogen fraction ($x_H < 0.02$). Because there is a wide miscibility gap in Pd-H alloy phase diagram at room temperature [141], the heterogeneity of np-Pd-H arises when phase transition takes place. Yet it has been reported that alloying palladium with other fcc metals of lesser solubility for H, such as gold, platinum, rhodium can depress T_C, thereby narrowing or even closing the miscibility gap at room temperature [141–145]. In this way, it is possible to prepare homogeneous Pd-based solid solutions which has a continuous solubility for H, avoiding phase transformation during H absorption and exhibiting a critical point at or near room temperature. For instance, Luo *et al.* demonstrated that when adding more than 15% gold in atomic percent, there was no observation of phase transition plateau near room temperature [145]. Therefore, nanoporous palladium-gold (np-Pd-Au) was chose as the research candidate in this section.

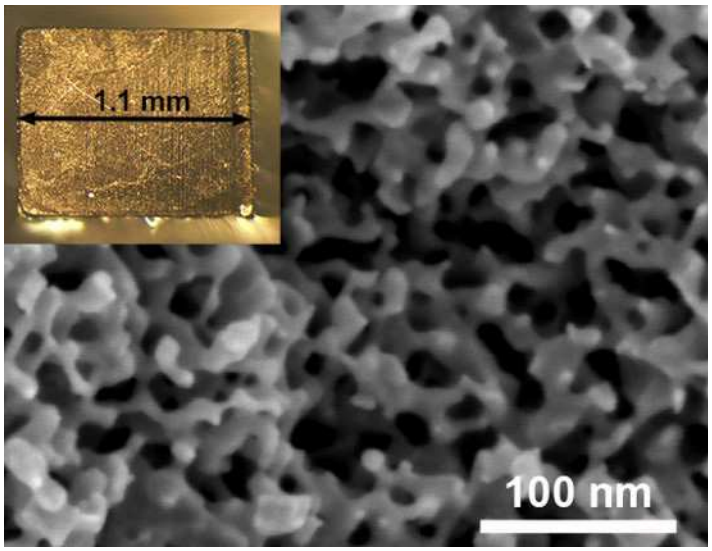

Figure 4.30: Scanning electron micrograph and optical micrograph (insert) of np-Pd-Au

Nanoporous palladium-gold was prepared by dealloying $Cu_{85}Pd_{12.5}Au_{2.5}$ in 1.0 M H_2SO_4 at 80 °C. A constant potential of 0.78 V was applied on the master alloy during the dealloying process. Afterwards, ten successive potential cycles between 0.4 and 0.77 V with a scan rate of 10 mV/s were imposed on as-dealloyed samples in 1.0 M H_2SO_4 at room temperature in order to further remove Cu residues. EDX analysis on three samples determined the average chemical composition $Pd_{77}Au_{15.5}Cu_{7.5}$. Figure 4.30 shows the microstructure of np-Pd-Au characterized by SEM and an optical microscope. It shows a bicontinuous porous structure with the ligament size of 7 nm. Moreover, inset image for the overview on outer surface show no cracks in the monolithic np-Pd-Au sample.

In-situ dilatometry and in-situ DMA tests were carried out on np-PdAu samples in 1.0 M H_2SO_4 at room temperature. The strategies for exploring H-sorption isotherms and H-induced elasticity variation in np-Pd in section 4.4 were also used in this section.

Figure 4.31a shows the interstitial hydrogen fraction versus the electrode potential at different scan rates. The results indicate that there is still a hysteresis during hydrogen ab-

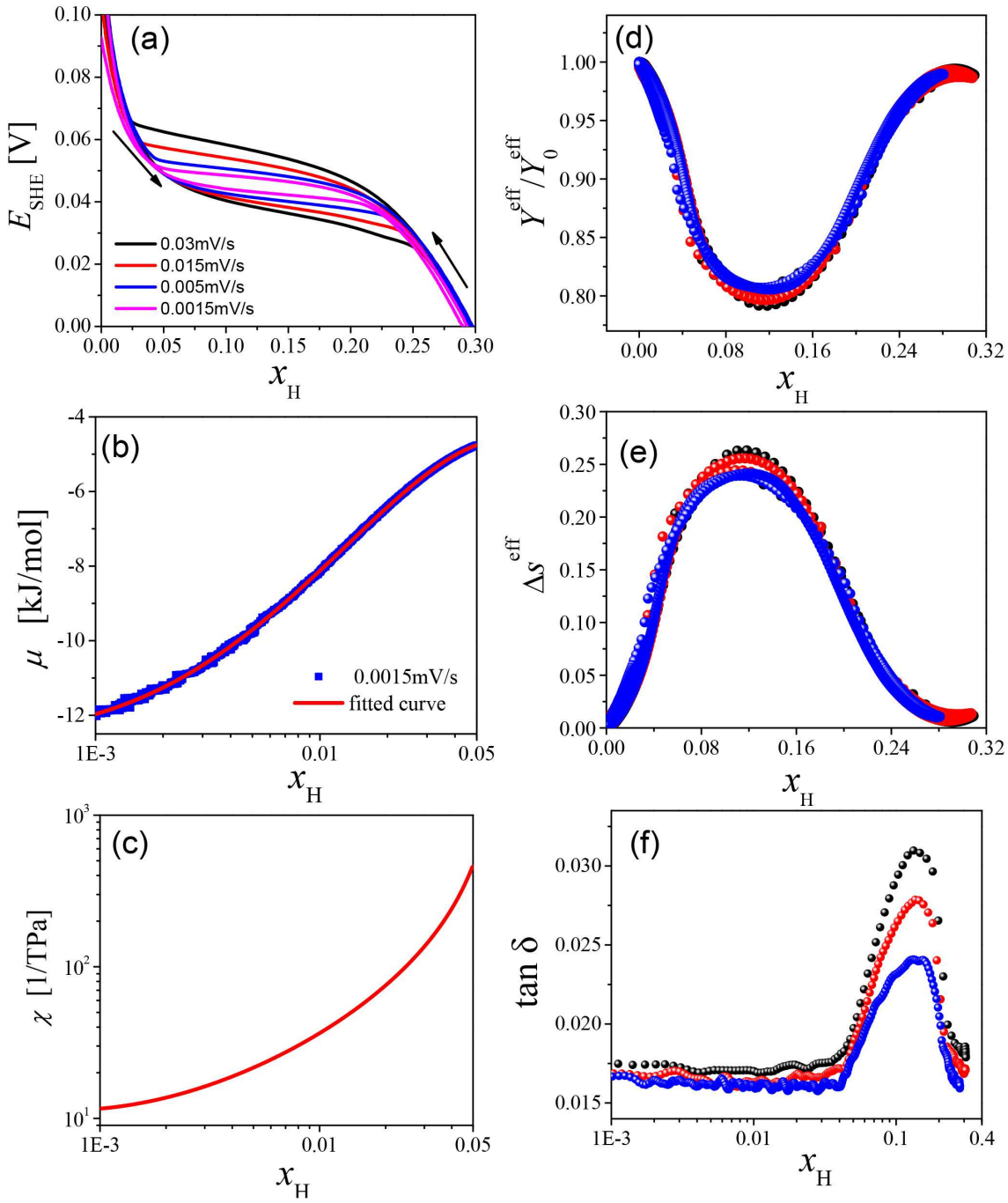

Figure 4.31: Chemo-mechanical coupling characterization of np-PdAu in 1.0 M H_2SO_4 aqueous solution. (a) Electrode potential (E_{SHE}) versus bulk hydrogen fraction (x_H) measured by in-situ dilatometer by evaluation of the strain during cyclic voltammetry. (b) Hydrogen chemical potential (μ_H) and (c) solute susceptibility parameter (χ) versus x_H in H-diluted region. (d) Normalized Young's modulus (Y_0^{eff}), (e) relative compliance change (Δs^{eff}) and (f) loss factor (tan δ)) versus x_H at different scan rates. Scan rates in (d-f): 0.03 mV/s (black), 0.015 mV/s (red) and 0.005 mV/s (blue).

sorption/desorption in np-Pd-Au, but the hysteresis decreases with decreasing scan rate. The small miscibility gap of np-Pd-Au is compatible with that of $Pd_{85}Au_{15}$ in Ref [145]. Based on the data from the lowest scan rate 0.0015 mV/s in Figure 4.31a, the two parameters, chemical potential (μ_H) and solute susceptibility ($\chi(x_H)$), are estimated according to equations 4.4 and 4.5, respectively. As shown in Figures 4.31b-c, both μ_H and $\chi(x_H)$ increase with increasing hydrogen fraction in the H-diluted regime.

Figures 4.31d-e show the normalized Young's modulus and relative compliance change of np-PdAu-H alloys in open system at different potential scan rates. Consistent elastic coefficients are observed at scan rates of 0.2, 0.1, and 0.03 mV/s. The coincidence of adsorption- and desorption branches indicates that miscibility gap is highly suppressed. Moreover, Figure 4.31e shows that H absorption in np-Pd-Au results in as large as 25% increase in compliance. Figure 4.31f shows loss factor ($\tan\delta = Y^{\text{eff}}_{\text{loss}}/Y^{\text{eff}}$) as a function of x_H during hydrogen absorption at different scan rates. Similar to np-Pd, np-PdAu-H also shows small loss factors (<2%) in the H-diluted ($x_H < 0.04$) and H-concentrated ($x_H > 0.26$) regimes, and increasing loss factors with increased scan rates at heterogeneous regimes.

4.6 Comparison between experimental result and Larché-Cahn theory prediction

The comparison between experiment and theory starts out with inspecting the elastic behavior within the regime of H-diluted solid solutions (α-Pd-H and α-Pd-Au-H). The experimental measurements on the elasticity of np-Pd and np-Pd-Au were carried out at a scan rate of 0.2 mV/s at frequencies of dynamic strain of 1 and 3 Hz. The relative compliance variations at these two frequencies for np-Pd and np-Pd-Au are shown in Figure 4.32a and b, respectively. For each material, experimental data sets for these two frequencies are consistent.

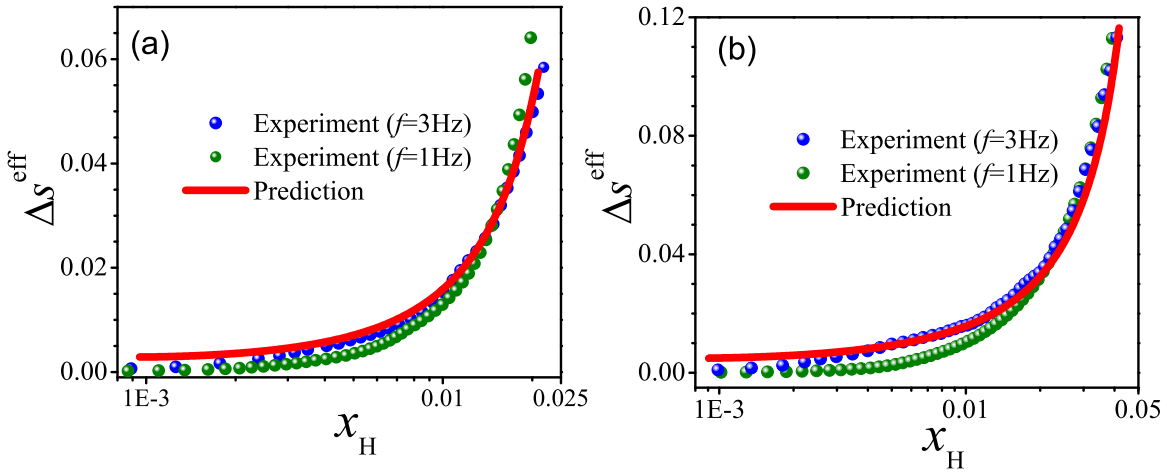

Figure 4.32: Experiment and Larché-Cahn theory prediction for relative compliance change (Δs^{eff}) as a function of interstitial hydrogen fraction (x_H) in (a) np-Pd-H and (b) np-PdAu-H. f denotes the frequency of dynamic strain.

The relative compliance variations for np-Pd and np-Pd-Au are also predicted by Larché-Cahn theory, according to in equation 2.14. In the prediction χ is taken from the experimental near-equilibrium isotherm in Figure 4.23 and η is 0.06, a value determined in Section 4.3.2. Finite Element Method simulations on the elasticity of nanoporous gold has demonstrated that Young's modulus of nanoporous metals scales with their polycrystalline massive metals [146]. Therefore, Young's modulus of polycrystalline massive palladium $Y = 120$ GPa (Ref [147]) is used in the prediction. The final results by Larché-Cahn theory prediction for np-Pd and

np-Pd-Au are shown in Figure 4.32a and b (denoted as Prediction, red lines), respectively. For each material, an excellent agreement is observed between experimental result and prediction, excluding at extremely low hydrogen fraction.

Chapter 5

Discussion

The key findings of this work include (1) the synthesis of high-quality monolithic nanoporous palladium with good mechanical stability and tunable structures, (2) the application of np-Pd-H as an excellent actuation material, (3) the observation of hydrogen-induced large stiffness tunability of np-Pd, and (4) the experimental verification of Larché-Cahn open-system elasticity theory.

5.1 Formation of hierarchical porous structure

It is found that a single-step dealloying of $Cu_{85}Pd_{15}$ alloy in 1.0 M H_2SO_4 at 25-80 °C produces hierarchical nanoporous palladium. The resulting samples have homogeneous composition distribution throughout the millimeter-sized body and show no macroscopical cracks. In particular, the microstructure formed at a dealloying temperature of 60 °C is very uniform and shows two well-defined length scales. As resolved by SEM, the upper-level ligament size is around 35 nm and the upper-level ligament size is < 10 nm). This hierarchical structure is very different from the classic unimodal porous structures that are produced by single-step dealloying single phase alloys such as silver-gold alloys, but looks similar to the nested network structure in np gold that are synthesized via a multi-step dealloying-coarsening-dealloying approach by Qi *et al.* [23, 24]. Additionally, dealloying two-phase precursor alloy such as Al+Al_3Pd can also produce np-Pd with several length scales, but the resulting np-Pd materials usually show non-uniform pores at upper hierarchical [27, 28]. It is believed that those pores are originated from the corrosion of active phase Al, in other words, the non-uniformity of upper-level pores is caused by the inhomogeneous distribution of Al phase in master alloy. When these np materials are under stresses, their non-uniform pores may result in cracks, severely compromising sample's mechanical performances. Differently, the nanoporous palladium materials synthesized in current thesis show uniform microstructures and excellent deformabilities.

The uniform hierarchical nanoporous structure of np-Pd produced by single-step dealloying process is unexpected. As shown in in Figure 5.1, the Pd-Cu phase diagram indicates that Cu and Pd can form single-phase alloy in the whole composition range [148]. The homogenization annealing treatment on as-casted $Cu_{85}Pd_{15}$ ingots at 800-900 °C ensures the formation of a single-phase alloy. The fast cooling procedure, quenching in water, also prevents the undesired disorder-order transformations which may produce $L1_2$-Cu_3Pd at low temperatures. Therefore, the hierarchical structure is not originated from the microstructure of master alloy, but forms during the corrosion process.

In literature, similar hierarchical morphologies have also been observed on the surface of np-Au films made by dealloying single phase Cu_3Au (1 1 1) when adding 1 mM potassium iodide into 0.1 M H_2SO_4 electrolyte [149]. The author found that copper iodide products precipitate on the primarily formed ultra-small ligaments in some regions at the outer surface

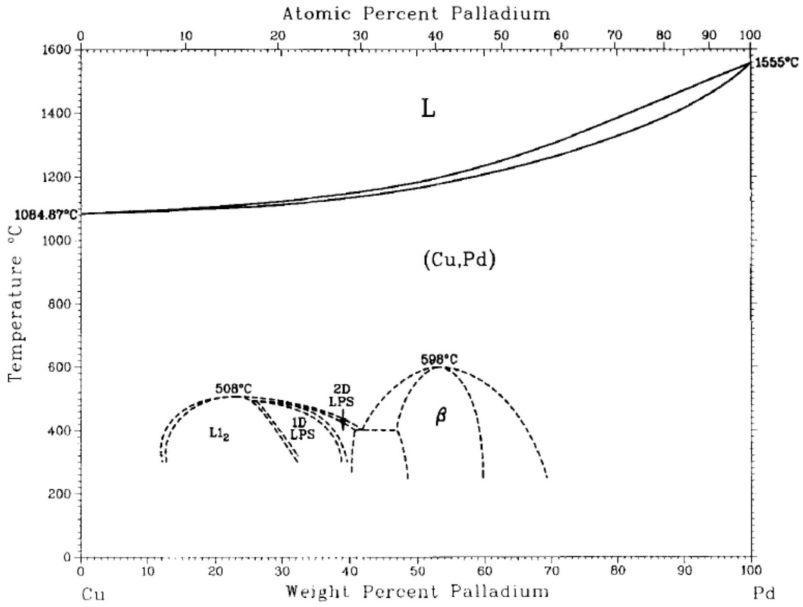

Figure 5.1: Pd-Cu phase diagram, taken from Ref [148]

layer. In the regions that covered with copper iodide precipitates, further coarsening of primarily formed ultra-small ligament/pores is inhibited. Instead, in the regions without copper iodide precipitates, the ligaments/pores coarsen gradually during the secondary dealloying process, resulting in a distinguished length scale in comparison to that in precipitates-covered region. However, this mechanism looks not applicable in the current situation. The reason is that during the corrosion of $Cu_{85}Pd_{15}$alloy in 1.0 M sulfuric acid, the possible chemical product, $CuSO_4$, is very soluble in aqueous solutions. Hierarchical porous structure has ever been observed in nanoporous palladium that was prepared by single-step dealloying a multicomponent metallic glass $Pd_{30}Ni_{50}P_{20}$ in 1.0 M sulfuric acid solution due to the different corrosion potential and rate between P and Ni [26]. Obviously, this mechanism is also not applicable in the current bimetallic alloy corrosion, because only one less noble metal (Cu) is corroded under the investigated potential range 780-820 mV.

Recently, according to systematic investigations on the electrochemical dealloying of single-phase Ag-Au(-Pt) alloys, Ye *et al.* proposed that the single step dealloying process for nanoporous np Au(-Pt) materials preparation includes a primary dealloying and a successively secondary dealloying [150]. Ag is gradually dissolved into electrolyte during the primary dealloying process, leading to a unimodal and ultra-small np Ag-Au(-Pt) material which still contains abundant Ag. The residual Ag inside the ultra-small ligaments can be substantially removed during the secondary dealloying process, leading to a np Au(-Pt) material with small amount of Ag. It is known that the dealloying process also involves a coarsening effect. This point promotes the assumption that the hierarchical structure in the current thesis may be the outcome of "primary dealloying→coarsening→secondary dealloying" during the corrosion process. As shown in Figure 4.12b, the abundant Cu residues and ultrafine porous structure of a partially dealloyed np-Pd sample at the center region (P1) looks like this region is just after primary dealloying process. However, the existence of the second type pore with significantly large length scale in the center region can not be explained by the cursory assumption. This phenomenon suggests that the hierarchical structure has already generated during or shortly after the primary dealloying process. Then another obvious assumption is promoted on the basis of Sieradzki's percolating cluster concept *et al.* [1]. In a Cu-Pd FCC lattice, regarding a Cu atom as the center of a local cluster where i denotes the number of nearest neighbor Pd atoms and ignoring surface and defects in the lattice, the number of nearest

neighbor Cu atoms becomes 12-i (12 is the coordination number of the FCC lattice). Cu-rich clusters featured with smaller i values are more active, therefore, the more active clusters may be preferentially corroded and generate the type II pores, around a few tens of nm in diameter (Figure 4.12). The heterogeneity of copper distribution in a master alloy would expect an incipient (spinodal?) demixing effect. However, as shown in the Pd-Cu phase diagram Figure 5.1, there is no evidence for demixing. By contrast, the ordering that occured at low temperature shows a negative mixing enthalpy. Therefore, the assumption of copper-rich clusters is also improbable.

A more possible mechanism is inspired by the structure instability at low solid fractions that was reported by Soyarslan *et al.* [146]. Their studies generate random-field and spinodal-like structures with various solid fraction. The spinodal-like structures not only look similar to the morphologies of dealloying-made nanoporous metals but also have very consistent results with regard to the influence of solid fraction on elastic properties. A more thorough consideration of that aspect is plausible because the solid fraction of the mostly investigated hierarchical np-Pd is around 17%, which value is very close to the solid percolation threshold (16%) for maintaining a continuous, three-dimensional scaffold [146]. However, in the present thesis, the dealloying-made np-Pd has a low solid fraction but shows a well-connected hierarchical porous network throughout the entire body (Figure 4.9). Only considering the dissolution of less noble metals and surface diffusion of noble metals in a conventional way can not explain the evolution of a hierarchical porous structure.

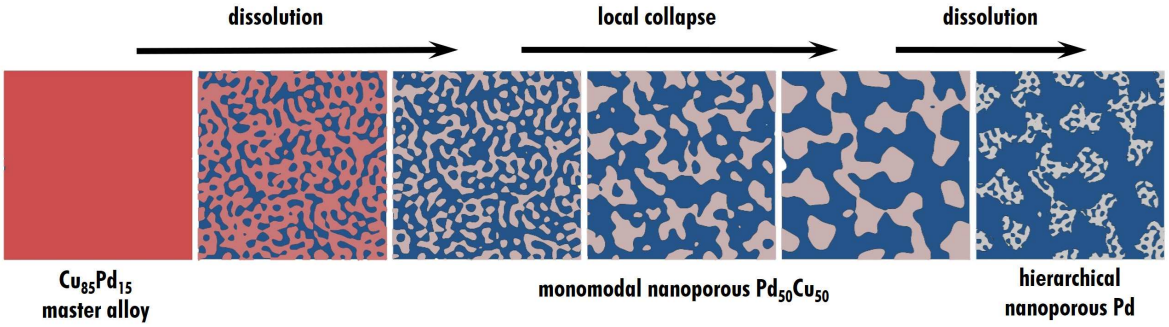

Figure 5.2: Schematic diagram for hierarchical pore evolution during dealloying a $Cu_{85}Pd_{15}$ alloy. Cu dissolution reduces the solid fraction and connectivity. During coarsening, weakly connected parts agglomerates, leading to large pores (upper level). Continuing corrosion of Cu further decreases the solid fraction, leading to the formation of fine lower-level pores. Solid: grayish color; pore: blue color.

The schematic for a hypothesized dealloying mechanism is presented in Figure 5.2. At the initial dealloying stage, the dissolution of less noble metal decreases the solid faction and then some parts locally lose connection and mechanical stability. As dissolution continues, solid fraction becomes lower, more and more parts lose connection. The instability leads a local densification and coalescence of collapsed solid parts. Ligaments coarsen and pore sizes become even larger. Those large pores correspond to the upper-level Type II pores in Figure 4.12. In middle stage of the dealloying process, further removal of Cu decreases solid fraction seriously which then induces local collapse and increase of Type II pore size. With dealloying proceeding, copper residues inside the large ligaments are further removed, generating ultrasmall pores, corresponding to the Type I pores (lower level) in Figure 4.12. The schematic for hypothesized dealloying mechanism in Figure 5.2 is compatible with the structure transition with increasing corrosion time, see P1-P4 in Figure 4.12. Briefly, the formation mechanism for hierarchical nanoporous palladium synthesized by single-step dealloying is supposed to relate to the low solid fraction induced local collapses.

5.2 Formation of unimodal porous structure by annealing

Importantly, it is observed that the as-prepared hierarchical np-Pd can be turned into classic unimodal np-Pd by annealing (Figure 4.13). By adjusting the annealing temperature, the ligament size can be tuned from a few tens of nm to a few hundreds of nm. The annealing strategy has ever been frequently used to vary ligament/pore sizes of many other nanoporous metals [14, 16–21]. The structure modulation of np materials by annealing generally involves surface diffusion, coalescence growth and disappearance of high energy small pores. The coarsening effect is believed to relate to many parameters like length scale of starting material, annealing environments such as atmosphere, temperature and duration [20, 151–153]. This explains the observation in Figure 4.13: as annealing temperature increases, diffusion is enhanced, which then leads to the increase of ligament size.

During annealing processes, the transition from hierarchical np structure into classic unimodal porous structure or the vanishment of lower level ligaments/pores is also an interesting observation. A growth scaling law has ever been proposed in the studies of solid particle sintering processes, describing the relationships between the time scale required for two solid particles' growth at the same sintering temperature [154]. In his study, a general equation: $\Delta t_2 = \lambda^n \Delta t_1$ is proposed. λ denotes the length scale ratio of particles 2 and 1. Δt_1 and Δt_2 denote the sintering time scales for particles 1 and 2, respectively, at the same temperature and keeping constant λ. For surface-diffusion mediated sintering it has n = 4; for volume-diffusion it has n = 3. Although the prediction by the scaling equation is not consistent with the surface-diffusion mediated coarsening of nanoporous metals like gold and silver [57, 155], the increasing time scale with increasing ligament size has been demonstrated by many studies [57, 156, 157]. Therefore, it is speculated that the lower level pores (Type I in Figure 4.12) in present hierarchical np-Pd coarsen faster than the large pores at the upper hierarchy level (Type II in Figure 4.12) and finally vanish with annealing continues. This speculation is consistent with the morphology variation during heating hierarchical np-Pd by SEM electron beam (Figure 4.14).

5.3 Hydrogen electrosorption in nanoporous palladium

The discussion in this section focuses on as-prepared hierarchical nanoporous palladium that obtained by dealloying $Cu_{85}Pd_{15}$ alloy in 1.0 M H_2SO_4 at 60 °C.

5.3.1 Surface area and hydrogen coverage

The site density per area for a dense-packed Pd surface is given by $\Gamma_0 = 4a^{-2}/\sqrt{3}$, where a denotes the lattice parameter. If the dense-packed surface is full covered by monolayer hydrogen atoms (one H per one Pd), the adsorbed H atoms per total Pd atoms can be estimated by

$$x_{\mathrm{H}}^{\mathrm{UPD}}|_{\mathrm{fullcoverage}} = \alpha \Gamma_0 M / N_A \tag{5.1}$$

where α denotes mass-specific surface area of Pd, M denotes the molar mass of Pd and N_A is Avogadro constant. In section 4.2, electrochemical characterization on np-Pd sample reveals a typical cyclic voltammogram of nanostructured Pd in acid solutions with the indications of oxygen species adsorption/desorption redox peak. The electrochemical active surface area is estimated via oxygen adsorption/desorption method. Dividing electrochemical active surface area by mass, the mass-specific surface area is determined to be $\alpha = 14.7\,\mathrm{m}^2/\mathrm{g}$ for np-Pd. Therefore, $x_{\mathrm{H}}^{\mathrm{UPD}}|_{\mathrm{fullcoverage}} = 0.039$ is obtained according to equation 5.1.

Hydrogen surface adsorption (or under potential deposition, UPD) and bulk absorption in np-Pd are also indicated in the cyclic voltammogram. They are also very well separated on the basis of the in-situ dilatometry analysis in Chapter 4. On the basis of the data in

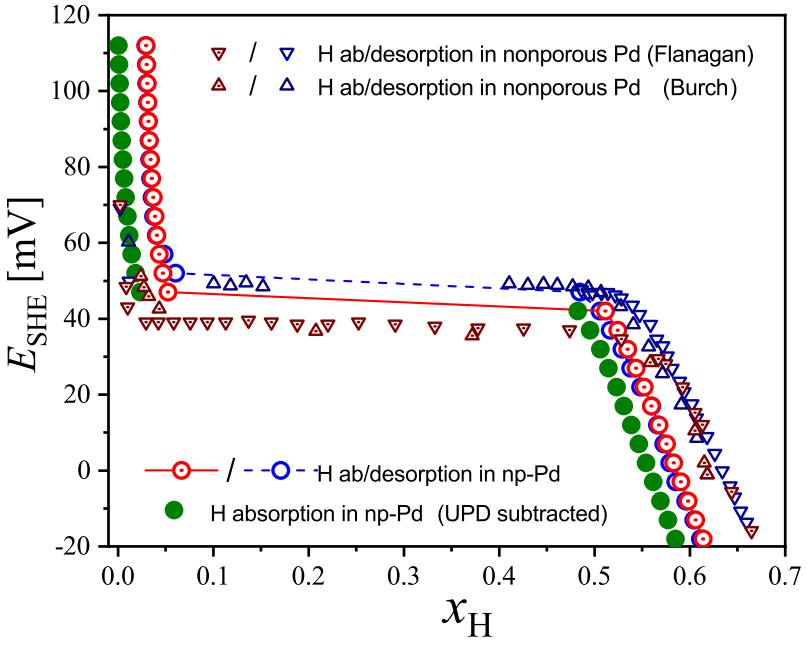

Figure 5.3: Sorption isotherms in the form of electrode potential (E_{SHE}) as a function of hydrogen fraction (x_{H}) at equilibrium near room temperature. Circles: results from hydrogen electrosorption in np-$Pd_{95}Cu_5$ at 298 K. Triangle symbols: literature results from hydrogen gas sorption in non-porous $Pd_{95}Cu_5$ at 303 K by Flanagan, Ref [162], and Burch *et al.*, Ref [163, 164].

Figure 4.18 and Figure 4.20, the potential range of H UPD is determined to occur in the potential range from 262 to 130 mV. The total H UPD atoms per metal atoms is determined to be $x_{\mathrm{H}}^{\mathrm{UPD}} = 0.029$. Therefore, H fractional coverage in np-Pd is then obtained via $\theta = x_{\mathrm{H}}^{\mathrm{UPD}}/x_{\mathrm{H}}^{\mathrm{UPD}}|_{\mathrm{fullcoverage}} = 0.74$. The value is comparable to the H fractional coverage ($\theta =$ 0.67-0.76) observed in previous studies [90, 158–161].

5.3.2 Sorption isotherms

Figure 5.3 shows hydrogen sorption isotherms in $Pd_{95}Cu_5$ near room temperature with electrode potential versus hydrogen fraction. The results for nanoporous Pd with a chemical composition of $Pd_{95}Cu_5$ are obtained by electrochemical absorption/desorption of hydrogen at room temperature 298 K. The results for nonporous sample with the same chemical composition $Pd_{95}Cu_5$, shortly non-porous Pd, are adopted from Refs [162–164], where hydrogen absorption/desorption are realized by exposing non-porous Pd in a hydrogen atmosphere under a given pressure at 303 K. For comparison, the hydrogen partial pressure p_{H_2} that is used in the investigation on non-porous Pd-H isotherm, is converted into electrode potential E using following equilibrium equation:

$$\mu_{\mathrm{H}} = {}^1\!/_2 RT \ln(p_{\mathrm{H}_2}) = -FE_{\mathrm{SHE}}\,, \tag{5.2}$$

where μ_{H} denotes chemical potential of atomic H, T denotes temperature, R is gas constant and E_{SHE} denotes electrode potential versus SHE. With attention to the α phase in Figure 5.3, it is found that there is a considerably larger net hydrogen fraction in nanoporous Pd in comparison to that in non-porous Pd at the same potential. Nanoporous Pd has obviously larger surface-to-volume ratio than non-porous one, therefore, np-Pd has more hydrogen adsorbate than non-porous Pd under the condition of a comparable UPD surface coverage fraction for the two materials. As shown in Figure 4.15, hydrogen surface adsorption takes place before the onset of substantial bulk absorption. Therefore, np-Pd having more UPD H at the surface

will contribute more to the total hydrogen fraction in compare to non-porous Pd. The contribution of hydrogen surface adsorption to the total hydrogen fraction is figured out on the basis of different strain-concentration coefficients between H UPD and interstitial H insertion, as shown in Figure 4.20. Excluding the hydrogen adsorption contribution, electrode potential as a function of interstitial hydrogen fraction is plotted and presented in Figure 5.3 (green color). It shows that the resulting $E - x_{\mathrm{H}}$ curve for nanoporous α-Pd-H phase agrees very well with that for non-porous α-Pd-H phase.

Different from the observation in np α-Pd-H, the equilibrium hydrogen fraction in the np α'-Pd-H regime is lower than that in non-porous α'-Pd-H materials under the same potential. This behavior in np-Pd is very close to the H sorption behavior in nanocrystalline Pd with a fine grain size around 10 nm [165–168]. For nanocrystalline Pd, preferential absorption of hydrogen in grain boundaries varies interface stresses in the grain boundary layers. This interface stresses in grain boundary layers lead to a pressure on the bulk (the core of nanocrystalline), which modifies hydrogen solubility and phase boundary lines. The pressure, P, as a function of bulk solute fraction, x_{H} relating to the chemical potential μ_{H} follows equation of state $\mu_{\mathrm{H}}(T, P, x_{\mathrm{H}}) = \mu_{\mathrm{H}}(T, 0, x_{\mathrm{H}}) + \Omega P$ [167]. A positive value of the pressure on the core of crystalline indicates a compression effect on the inner bulk, which thereby reduces hydrogen solubility at equilibrium. As for np-Pd materials, the saturation of hydrogen at the surface of nanoligaments induces surface stresses on the inner bulk, which then impacts the thermodynamics of hydrogen absorption. The role of surface stress in nanoligaments is believed to be similar to the role of interface stress associated with grain boundary in nano*crystalline* [90, 166, 168]. It then concludes that imposing a negative surface stress on α'-Pd-H increases hydrogen solubility and imposing a positive surface stress on α'-Pd-H reduces hydrogen solubility, very well supporting the present observations.

In the two-phase coexisted regime, nanoporous palladium shows a much smaller hysteresis in comparison to non-porous palladium. Similar phenomena has ever been observed in the studies of H sorption in kinds of nanostructured palladium materials [169–171]. Yamauchi *et al.* found that hydrogen absorption/desorption hysteresis exists even in very small-sized Pd particles (2-3 nm in diameter), but 2-3 nm Pd particles show a narrower hysteresis than 6-8 nm Pd particles at the same temperature [170].

5.4 H-assisted actuation with nanoporous palladium

This thesis demonstrates that H-assisted actuation with np-Pd exhibits excellent performance such as a large strain amplitude (up to 4%), a long-term stability as well as a fast response.

5.4.1 Large actuation amplitude and long-term stability

The large strain amplitude or large reversible expansion/contraction of Pd is induced by absorption/desorption of a large amount of hydrogen. It is found that hydrogen fraction in np-Pd can reach as high as $x_{\mathrm{H}} = 0.67$ at room temperature, resulting in up to 4% expansion (Figure 4.19).

It's well know that materials undergoing cyclic $\alpha \leftrightarrow \alpha'$ phase transition often show poor cycling performances. Failures such as cracking, buckling, and decohesion from the substrate have already been observed in Pd thin films after undergoing several times of phase transition [75, 172, 173]. With respect to non-porous Pd bulk samples, a few cycles through phase transition can even lead to drastic plastic deformation [174]. Therefore, it is amazing that np-Pd in present work shows an excellent cycling performance even though it goes through more than 1000 times of $\alpha \leftrightarrow \alpha'$ phase transformation. Such an excellent cycling stability may be related to the large amounts of uniform-distributed nanopores, which release phase transition induced misfit dislocations and reduce local stresses. Moreover, the high strength

of nanoligaments may avoid lattice deformation during phase transition.

5.4.2 Fast response

The fast response is another advantage of using np-Pd-H as actuation materials. This is mainly attributed to the fast proton mobility in sulfuric acid and the fast diffusion of H atoms in the Pd lattice. With attention to H diffusion in Pd at room temperature, $D = 3.8 \times 10^{-11} \mathrm{m}^2/\mathrm{s}$ is taken as the diffusion coefficient [72, 90, 175]. Half of the sample size, $l_1 = 0.5\,\mathrm{mm}$, and half of ligament size, $l_2 = 20\,\mathrm{nm}$, are taken as H diffusion distances for non-porous Pd and np-Pd, respectively. Assuming the diffusion coefficient D is invariable for both kinds of sample, the characterized diffusion time will scale with diffusion distance, $t \sim l^2/2D$. The hydrogen diffusion distance of np-Pd is more than 4 orders of magnitude smaller than that of non-porous Pd, therefore, the time constant for H equilibration in np-Pd is reduced by more than 10^8 times. The equilibration time of $\approx$ 1h and $\approx 5\mu$s is estimated for nonporous Pd and porous Pd, respectively. Obviously, the hydrogen diffusion in the nanoscaled ligaments is much faster. The proton transport is also a fast process in current acidic aqueous solution due to the abundant protons and high effective proton mobility [176]. This may explain the phenomenon that hydrogen absorption in present thesis using sulfuric acid electrolytes show a much faster response than hydrogen absorption in a np-Pd material with comparable structure size using alkaline electrolytes [28]. Additionally, as reported by Qi *et al.*, the hierarchy of pore structure provides large upper-level pores for fast mass transport through the electrolyte [23] and provides small lower-level ligaments for functionalization such as in our present np Pd, because small ligaments have abundant active surface sites for hydrogen sorption and short distances for hydrogen diffusion.

5.5 Open-system elasticity of nanoporous palladium-hydrogen

Two central observations from in-situ DMA measurements are: (1) H insertion in np-Pd leads to over 30% relative compliance increasement, which is highly reversible and electrochemically controllable. (2) open-system elastic coefficient, as one of the key conclusion of Larché-Cahn theory, is for the first time experimentally verified using np α-Pd-H materials.

5.5.1 In-situ DMA as a valid methodology for open-system elasticity measurement

Non-destructive methods including ultrasound pulse-echo technique or resonant ultrasounds spectroscopy (RUS) have ever been reported for in-situ measuring the variation of elasticity in Pd-H alloys with temperature or hydrogen fraction [177–179]. The sample sizes vary from several tens μm thin films to mm-sized bulk samples. The time (t) required for H diffusion through a distance (l) can be estimated with $t = l^2/2D$, where D denotes H diffusion coefficient in the media material. Taking $D = 4 \times 10^{-11}\,\mathrm{m}^2/\mathrm{s}$ for H diffusion in Pd at room temperature [72, 90, 175] and half of sample size as diffusion distance, diffusion time for $100\,\mu$m thick sample is then estimated to be around 30 s. The ultrasound frequency is above 20 kHz. It is seen that hydrogen is short of time for redistribution at such high frequency, therefore, acoustic investigation actually measures the elastic coefficients of Pd-H at fixed composition in closed system.

As for in-situ DMA strategies used in this work, hydrogen fraction was adjusted by electrochemical approaches, and elastic parameters were measured by compressing monolithic np Pd-H samples in the electrolyte within the linear elastic region. When a small uniaxial load is applied on a np-Pd-H sample under constant electrode potential or chemical potential, locally the fraction of mobile hydrogen interstitials in each ligament is actually variable. Uniform tensile or compressive stresses may lead to H exchange between ligaments and surrounding

electrolyte, altering H fraction. Stress gradient, the nonuniform-stress distribution in bent Pd ligaments, will lead to H redistribution: H atoms migrate from compressive region to dilatation region. Using the same H diffusion coefficient and equation described in proceeding section, it suggests that diffusion time for a 20 nm diameter ligament is around 1 μs. Contrast to above acoustic investigation, the time scale for hydrogen redistribution is far less than the conventional DMA frequency (<100 Hz). Therefore, in the present work, the fine ligament size (<10 nm) of np-Pd enables ultrafast H redistribution, supporting that in-situ DMA as a valid approach to measure the open system elastic parameters of np-Pd-H.

5.5.2 Large Young's modulus variation with hydrogen fraction

It has been demonstrated with nanoporous gold that the effective Young's modulus of np metal scales with the Young's modulus of corresponding massive polycrystalline metal [16, 146]. The effective Young's modulus of np-Pd is supposed to be proportional to the Young's modulus of massive polycrystalline Pd in open system. Therefore, the relative Young's modulus or compliance variation with hydrogen fraction is irrespective of the porosity. It is reasonable to do the comparison between closed-system and open-system elasticity variations with hydrogen fraction in np-Pd using the Young's modulus of massive Pd-H in Equation 2.14. Consistent with ordinary closed-system Young's modulus of massive Pd-H, the hydrogen fraction can influence the effective open-system Young's modulus of np-Pd-H in this thesis. But the relative Young's modulus variation with hydrogen fraction in open system is quantitatively different from that in closed system.

In the domain of H-diluted region ($x_H < 0.02$), more than 5% reduction in effective open-system Young's modulus of α-Pd-H is observed (Figure 4.27a). By contrast, much smaller closed-system Young's modulus change is observed within the same hydrogen fraction region. For instance, in the investigations by Salama and Ko, 0.5% closed-system Young's modulus (polycrystalline) reduction was observed when inserting 1 at% hydrogen [180]. Schwarz *et al.* studied the hydrogen insertion in single-crystalline Pd materials and demonstrated hydrogen-induced negligible decreases of two closed-system shear moduli parameters, C_{44} and $C' = (C_{11} + C_{12})/2$, within H-diluted regime [179].

In the H-concentrated α' phase, the effective open-system Young's modulus decreases with increasing H fraction (Figure 4.27a). Similar to α phase, the reduction in Young's modulus of α' phase can be explained by H-induced lattice dilatation. The same trend has also been observed in the variation of closed-system shear constant C_{44} and C' with hydrogen fraction in Schwarz's studies via a RUS approach [179].

The largest Young's modulus reduction of nanoporous Pd-H is observed in two-phase ($\alpha + \alpha'$) coexisted region, where Y^{eff}-x_H curve shows a parabolic-like shape (Figure 4.27a). The lowest effective Young's modulus is in the two-phase regime. This phenomenon is very similar to the results for elastic constant C_{44} of Pd-H in two-phase state by Schwarz and his coauthors [179]. In their studies, the elastic constant values for the coherent two-phase regime (at compositions near single phase) are measured by the RUS method and results for the incoherent two-phase coexisted region are from calculations. They estimate that largest Young's modulus reduction occurs in the middle of the incoherent two-phase coexisted region, consistent with the results for effective Young's modulus of nanoporous Pd-H. This behavior may be explained by the increased time scale for H redistribution due to increasing diffusion length scales caused by the large heterogeneity in such region. This viewpoint is supported by the observed loss factor variation in Figure 4.26: the loss factor in the two-phase region is relatively large and dependent on scan rates; the loss factor in single-phase (α or α') regions is small and independent on scan rates. The short of time for H equilibration and redistribution in the two-phase region is qualitatively similar to the situation in the high-frequency RUS experiment [179].

5.5.3 Excellent agreement between experiment and Larché-Cahn theory prediction

Due to the slow and incomplete hydrogen equilibration at the two-phase coexisted region and the lack of closed-system Young's modulus data beyond hydrogen-diluted region, the comparison between relative open-system compliance variation and Larché-Cahn theory prediction is restricted to the single-phase np α-Pd-H regime with $x_{\mathrm{H}} < 2\%$ and np α-Pd-Au-H regime with $x_{\mathrm{H}} < 4\%$. Relevant studies in literature concluded that the insertion of a small amount of hydrogen will not substantially change closed-system elastic parameters of Pd [179, 180]. Therefore, it is reasonable to replace the closed-system Young's modulus (Y^x) at $x_{\mathrm{H}} < 0.02$ with the value of pure metal in the calculation and prediction of relative open-system compliance change, Δs, using Equation 2.14. Remarkably, the result predicted by theory and that extracted directly from in-situ DMA experiments show an excellent agreement, see Figure 4.32. The comparison in-turn demonstrates mobile hydrogen interstitials lead to significant compliance increase in open system and the compliance increase with increasing hydrogen fraction in hydrogen-diluted α phase regimes.

Chapter 6

Summary and outlook

6.1 Summary

In this thesis, monolithic nanoporous palladium materials are synthesized by electrochemical dealloying Cu-Pd alloys in sulfuric acid. Systematic investigations are done to determine proper dealloying parameters. The influences of electrode potential and dealloying temperature as well as post annealing treatments on microstructure of np-Pd are also investigated. Dealloying $Cu_{85}Pd_{15}$ in 1.0 M sulfuric acid is a facile method to fabricate uniform and crack-free monolithic hierarchical nanoporous np-Pd. The excellent mechanical deformability of np-Pd testifies its microstructural uniformity and connectivity. Quite reproducibly, the single-step dealloying process at 60 °C leads to a hierarchical network structure with two well-defined ligament sizes (35 nm and <10 nm). Further annealing treatments on hierarchical np-Pd samples lead to unimodal porous structures with controllable ligament sizes. The uniformity and facile preparation of monolithic np-Pd foreordain the material as an alternative of nanoporous gold for functionalization and for the study of mechanical properties of nanostructured metals by using transitional macroscopic mechanical tests.

This thesis also explores the mechanical responses of hierarchical np palladium through electrochemically controlled hydrogen sorption. In-situ dilatometry is used to record samples' expansion/contraction during hydrogen absorption/desorption processes; in-situ DMA is used to measure samples' elasticity variation with hydrogen content. Hydrogen electrosorption in np palladium results in (1) large reversible strain variations (up to 4%), which are stable even after more than 1000 cycles, and (2) large reversible elasticity variations (more than 30% increase in compliance).

Several scientific issues in relation to the above observations are then discussed. Based on experimental results from a partially dealloyed sample, a percolating cluster and low solid fraction induced structure instability concept is considered for explaining the evolution mechanism of hierarchical nanoporous structure during a single-step dealloying process. With respect to chemo-mechanical coupling in nanoporous palladium-hydrogen, the results of hydrogen sorption isotherms and the composition-strain coupling demonstrate that the behavior of nanoporous palladium-hydrogen can be quantitatively understood in terms of the established behavior of non-porous palladium-based hydrides and of hydrogen underpotential deposition on planar palladium surfaces.

Another important findings of this thesis is that the experimentally measured effective open system elasticity of np palladium-hydrogen and np palladium-gold-hydrogen shows very well agreement with Larché-Cahn theory prediction. Larché-Cahn theory of open-system elasticity, as one significant advance in thermodynamics of the 20th century, is experimentally verified.

6.2 Outlook

This thesis focuses on the synthesis of nanoporous palladium and the utilization of np-Pd-H as a probe for chemo-mechanical coupling studies, from which np-Pd-H is developed as an actuation material and as a model system to verify Larché-Cahn open-system elasticity theory. Besides the observations in this thesis, there are several open questions arising from this thesis.

The first question, which follows from section 4.3, is to investigate the reason for the excellent stability of np-Pd-H after more than 1000 cycles phase transition. Despite the stable morphology of a np-Pd sample after cycling which has already been done in the present thesis, the lattice structure variation before, after and even during the phase transition should be explored via in-situ X-ray diffraction or other techniques for a deeper understanding of the stability after more than 1000 cycles of phase transition.

The second question is to study the impact of ligament size on the elasticity of nanoporous palladium-hydrogen. This thesis confirms that in-situ DMA is a valid method to measure open-system Young's modulus of nanoporous-palladium-hydrogen. All the in-situ DMA measurements are carried out on hierarchical nanoporous palladium which has a lower-level ligament size below 10 nm. The small size enables a fast diffusion and equilibration. Different ligament sizes will lead to different hydrogen diffusion distances and then lead to a difference in hydrogen diffusion or redistribution under stresses. Therefore, studies regarding the role of ligament sizes would be worthwhile.

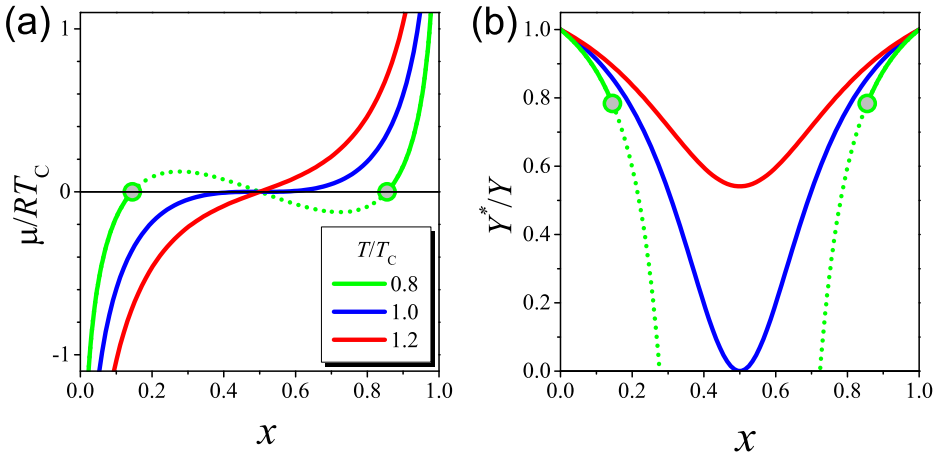

Figure 6.1: (a) Chemical potential (μ) variation with solid fraction (x) in a regular solution at different temperatures. T_C - the critical temperature. (b) Open-system Young's modulus normalized to the closed-system Young's modulus (Y^*/Y) in response to solute fraction. Dashed lines: miscibility gap.

The third question, which follows from section 4.5, is the possibility of synthesizing a nanoporous Pd-based material which has a continuous solubility for hydrogen at or near room temperature and can reach "zero Young's modulus" during hydrogen sorption in open system. The expectation of "zero Young's modulus" is illustrated with a regular interstitial solution. In a regular interstitial solution, the chemical potential of solid can be expressed as $\mu = RT_C\left((2-4x)+\tau ln(x/(1-x))\right)$, where x is the atomic fraction and $\tau = T/T_C$ is defined as the temperature (T) per critical temperature (T_C) for a continuous solubility. Corresponding chemical potential-composition isotherms below, at and above the critical temperature are shown in Figure 6.1a. Taking Pd-H as an example and without considering the closed-system Young's modulus variation with H fraction, open-system Young's modulus Y^* is estimated according to equation 2.13 based on materials parameter in Ref [168]. Y^* normalized to

the closed-system Young's modulus Y as a function of hydrogen fraction is displayed in Figure 6.1b. It shows that H-induced drastically decrease of the open-system Young's modulus at all temperatures. Amazingly, zero open-system Young's modulus is reached at the critical point. Therefore, it is certainly of great interest to explore the possibility in experiments. In this thesis, a larger reduction in open-system compliance is demonstrated by using np-Pd-Au which has a double-wide H-diluted region (x_{H} <0.04) than np-Pd (Figure 4.32). The alloying of Au highly narrows the miscibility gap, which is one big step to reaching the critical point. Therefore, further research should be undertaken to explore the possibility of reaching zero Young's modulus in open system.

References

[1] K. Sieradzki, R. Corderman, K. Shukla, R. Newman, Computer simulations of corrosion: selective dissolution of binary alloys, Philosophical Magazine A 59 (1989) 713–746.

[2] J. Erlebacher, M. J. Aziz, A. Karma, N. Dimitrov, K. Sieradzki, Evolution of nanoporosity in dealloying, Nature 410 (2001) 450.

[3] J. Weissmüller, R. C. Newman, H. Jin, A. M. Hodge, J. W. Kysar, Nanoporous metals by alloy corrosion: formation and mechanical properties, MRS Bulletin 34 (2009) 577–586.

[4] B. C. Tappan, S. A. Steiner III, E. P. Luther, Nanoporous metal foams, Angewandte Chemie International Edition 49 (2010) 4544–4565.

[5] J. Weissmüller, K. Sieradzki, Dealloyed nanoporous materials with interface-controlled behavior, MRS Bulletin 43 (2018) 14–19.

[6] H. Jin, J. Weissmüller, D. Farkas, Mechanical response of nanoporous metals: A story of size, surface stress, and severed struts, MRS Bulletin 43 (2018) 35–42.

[7] E. Şeker, W. Shih, K. J. Stine, Nanoporous metals by alloy corrosion: Bioanalytical and biomedical applications, MRS Bulletin 43 (2018) 49–56.

[8] I. McCue, A. Karma, J. Erlebacher, Pattern formation during electrochemical and liquid metal dealloying, MRS Bulletin 43 (2018) 27–34.

[9] Q. Chen, Y. Ding, M. Chen, Nanoporous metal by dealloying for electrochemical energy conversion and storage, MRS Bulletin 43 (2018) 43–48.

[10] S. Parida, D. Kramer, C. A. Volkert, H. Rösner, J. Erlebacher, J. Weissmüller, Volume change during the formation of nanoporous gold by dealloying, Physical Review Letters 97 (2006) 035504.

[11] Y. Zhong, J. Markmann, H. Jin, Y. Ivanisenko, L. Kurmanaeva, J. Weissmüller, Crack mitigation during dealloying of $Au_{25}Cu_{75}$, Advanced Engineering Materials 16 (2014) 389–398.

[12] A. Dursun, D. V. Pugh, S. G. Corcoran, Dealloying of Ag-Au alloys in halide-containing electrolytes affect on critical potential and pore size, Journal of the Electrochemical Society 150 (2003) B355–B360.

[13] L. Qian, M. Chen, Ultrafine nanoporous gold by low-temperature dealloying and kinetics of nanopore formation, Applied Physics Letters 91 (2007) 083105.

[14] M. Hakamada, M. Mabuchi, Nanoporous gold prism microassembly through a self-organizing route, Nano Letters 6 (2006) 882–885.

[15] N. Mameka, Surface-controlled mechanical properties of bulk nanoporous gold, Ph.D. thesis, Technische Universität Hamburg-Harburg, 2016.

[16] L. Liu, X. Ye, H. Jin, Interpreting anomalous low-strength and low-stiffness of nanoporous gold: Quantification of network connectivity, Acta Materialia 118 (2016) 77–87.

[17] L. Qian, X. Yan, T. Fujita, A. Inoue, M. Chen, Surface enhanced raman scattering of nanoporous gold: Smaller pore sizes stronger enhancements, Applied Physics Letters 90 (2007) 153120.

[18] Y. K. Chen-Wiegart, S. Wang, Y. S. Chu, W. Liu, I. McNulty, P. W. Voorhees, D. C. Dunand, Structural evolution of nanoporous gold during thermal coarsening, Acta Materialia 60 (2012) 4972–4981.

[19] K. Wang, J. Weissmüller, Composites of nanoporous gold and polymer, Advanced Materials 25 (2013) 1280–1284.

[20] A. Chen, S. Shi, F. Liu, Y. Wang, X. Li, J. Gu, X. Xie, Effect of annealing atmosphere on the thermal coarsening of nanoporous gold films, Applied Surface Science 355 (2015) 133–138.

[21] S. Baier, A. Wittstock, C. D. Damsgaard, A. Diaz, J. Reinhardt, F. Benzi, J. Shi, T. Scherer, D. Wang, C. Kübel, et al., Influence of gas atmospheres and ceria on the stability of nanoporous gold studied by environmental electron microscopy and in situ ptychography, RSC Advances 6 (2016) 83031–83043.

[22] Y. Ding, J. Erlebacher, Nanoporous metals with controlled multimodal pore size distribution, Journal of the American Chemical Society 125 (2003) 7772–7773.

[23] Z. Qi, J. Weissmüller, Hierarchical nested-network nanostructure by dealloying, Acs Nano 7 (2013) 5948–5954.

[24] Z. Qi, U. Vainio, A. Kornowski, M. Ritter, H. Weller, H. Jin, J. Weissmüller, Porous gold with a nested-network architecture and ultrafine structure, Advanced Functional Materials 25 (2015) 2530–2536.

[25] H. Duan, Q. Hao, C. Xu, Hierarchical nanoporous PtTi alloy as highly active and durable electrocatalyst toward oxygen reduction reaction, Journal of Power Sources 280 (2015) 483–490.

[26] J. Yu, Y. Ding, C. Xu, A. Inoue, T. Sakurai, M. Chen, Nanoporous metals by dealloying multicomponent metallic glasses, Chemistry of Materials 20 (2008) 4548–4550.

[27] Q. Kong, L. Lian, Y. Liu, J. Zhang, L. Wang, W. Feng, Bulk hierarchical nanoporous palladium prepared by dealloying PdAl alloys and its electrochemical properties, Microporous and Mesoporous Materials 208 (2015) 152–159.

[28] J. Zhang, Q. Bai, Z. Zhang, Dealloying-driven nanoporous palladium with superior electrochemical actuation performance, Nanoscale 8 (2016) 7287–7295.

[29] Q. Kong, L. Lian, Y. Liu, J. Zhang, Fabrication and compression properties of bulk hierarchical nanoporous copper with fine ligament, Materials Letters 127 (2014) 59–62.

[30] H. Qiu, Y. Ito, M. Chen, Hierarchical nanoporous nickel alloy as three-dimensional electrodes for high-efficiency energy storage, Scripta Materialia 89 (2014) 69–72.

[31] X. Li, B. Huang, C. Qiu, Z. Li, L. Shao, H. Liu, Hierarchical nested-network porous copper fabricated by one-step dealloying for glucose sensing, Journal of Alloys and Compounds 681 (2016) 109–114.

[32] T. Fujita, Hierarchical nanoporous metals as a path toward the ultimate three-dimensional functionality, Science and Technology of Advanced Materials 18 (2017) 724–740.

[33] V. Zielasek, B. Jürgens, C. Schulz, J. Biener, M. M. Biener, A. V. Hamza, M. Bäumer, Gold catalysts: nanoporous gold foams, Angewandte Chemie International Edition 45 (2006) 8241–8244.

[34] C. Xu, J. Su, X. Xu, P. Liu, H. Zhao, F. Tian, Y. Ding, Low temperature CO oxidation over unsupported nanoporous gold, Journal of the American Chemical Society 129 (2007) 42–43.

[35] Y. Ding, M. Chen, Nanoporous metals for catalytic and optical applications, MRS Bulletin 34 (2009) 569–576.

[36] S. Kucheyev, J. Hayes, J. Biener, T. Huser, C. Talley, A. Hamza, Surface-enhanced raman scattering on nanoporous Au, Applied Physics Letters 89 (2006) 053102.

[37] H. Liu, L. Zhang, X. Lang, Y. Yamaguchi, H. Iwasaki, Y. Inouye, Q. Xue, M. Chen, Single molecule detection from a large-scale sers-active $Au_{79}Ag_{21}$ substrate, Scientific Reports 1 (2011) 112.

[38] C. Stenner, L. Shao, N. Mameka, J. Weissmüller, Piezoelectric gold: Strong charge-load response in a metal-based hybrid nanomaterial, Advanced Functional Materials 26 (2016) 5174–5181.

[39] D. Kramer, R. N. Viswanath, J. Weissmüller, Surface-stress induced macroscopic bending of nanoporous gold cantilevers, Nano Letters 4 (2004) 793–796.

[40] H. Jin, X. Wang, S. Parida, K. Wang, M. Seo, J. Weissmüller, Nanoporous Au-Pt alloys as large strain electrochemical actuators, Nano Letters 10 (2009) 187–194.

[41] E. Detsi, S. Punzhin, J. Rao, P. R. Onck, J. T. M. De Hosson, Enhanced strain in functional nanoporous gold with a dual microscopic length scale structure, Acs Nano 6 (2012) 3734–3744.

[42] S. Shi, J. Markmann, J. Weissmüller, Actuation by hydrogen electrosorption in hierarchical nanoporous palladium, Philosophical Magazine 97 (2017) 1571–1587.

[43] C. Cheng, L. Lührs, T. Krekeler, M. Ritter, J. Weissmüller, Semiordered hierarchical metallic network for fast and large charge-induced strain, Nano Letters 17 (2017) 4774–4780.

[44] T. Juarez, J. Biener, J. Weissmüller, A. M. Hodge, Nanoporous metals with structural hierarchy: A review, Advanced Engineering Materials (2017).

[45] R. Li, K. Sieradzki, Ductile-brittle transition in random porous Au, Physical Review Letters 68 (1992) 1168.

[46] N. Senior, R. Newman, Synthesis of tough nanoporous metals by controlled electrolytic dealloying, Nanotechnology 17 (2006) 2311.

[47] H. Jin, L. Kurmanaeva, J. Schmauch, H. Rösner, Y. Ivanisenko, J. Weissmüller, Deforming nanoporous metal: Role of lattice coherency, Acta Materialia 57 (2009) 2665–2672.

[48] N. J. Briot, T. Kennerknecht, C. Eberl, T. J. Balk, Mechanical properties of bulk single crystalline nanoporous gold investigated by millimetre-scale tension and compression testing, Philosophical Magazine 94 (2014) 847–866.

[49] N. Mameka, K. Wang, J. Markmann, E. T. Lilleodden, J. Weissmüller, Nanoporous gold-testing macro-scale samples to probe small-scale mechanical behavior, Materials Research Letters 4 (2016) 27–36.

[50] N. Badwe, X. Chen, K. Sieradzki, Mechanical properties of nanoporous gold in tension, Acta Materialia 129 (2017) 251–258.

[51] H. Jin, J. Weissmüller, A material with electrically tunable strength and flow stress, Science 332 (2011) 1179–1182.

[52] S. Sun, X. Chen, N. Badwe, K. Sieradzki, Potential-dependent dynamic fracture of nanoporous gold, Nature Materials 14 (2015) 894.

[53] N. Mameka, J. Markmann, H. Jin, J. Weissmüller, Electrical stiffness modulation-confirming the impact of surface excess elasticity on the mechanics of nanomaterials, Acta Materialia 76 (2014) 272–280.

[54] T. Wada, H. Kato, Three-dimensional open-cell macroporous iron, chromium and ferritic stainless steel, Scripta Materialia 68 (2013) 723–726.

[55] J. W. Kim, M. Tsuda, T. Wada, K. Yubuta, S. G. Kim, H. Kato, Optimizing niobium dealloying with metallic melt to fabricate porous structure for electrolytic capacitors, Acta Materialia 84 (2015) 497–505.

[56] I. Okulov, A. Okulov, I. Soldatov, B. Luthringer, R. Willumeit-Römer, T. Wada, H. Kato, J. Weissmüller, J. Markmann, Open porous dealloying-based biomaterials as a novel biomaterial platform, Materials Science and Engineering: C 88 (2018) 95–103.

[57] C. Wang, Q. Chen, Reduction-induced decomposition: Spontaneous formation of monolithic nanoporous metals of tunable structural hierarchy and porosity, Chemistry of Materials 30 (2018) 3894–3900.

[58] W. Yang, X. Zheng, S. Wang, H. Jin, Nanoporous aluminum by galvanic replacement: Dealloying and inward-growth plating, Journal of The Electrochemical Society 165 (2018) C492–C496.

[59] J. J. Dosch, D. J. Inman, E. Garcia, A self-sensing piezoelectric actuator for collocated control, Journal of Intelligent Material Systems and Structures 3 (1992) 166–185.

[60] K. Uchino, Piezoelectric actuators and ultrasonic motors, volume 1, Springer Science & Business Media, 1996.

[61] Q. Zhang, V. Bharti, X. Zhao, Giant electrostriction and relaxor ferroelectric behavior in electron-irradiated poly (vinylidene fluoride-trifluoroethylene) copolymer, Science 280 (1998) 2101–2104.

[62] R. H. Baughman, Conducting polymer artificial muscles, Synthetic Metals 78 (1996) 339–353.

[63] R. H. Baughman, Playing nature's game with artificial muscles, Science 308 (2005) 63–65.

[64] T. Mirfakhrai, J. D. Madden, R. H. Baughman, Polymer artificial muscles, Materials Today 10 (2007) 30–38.

[65] Y. Bar-Cohen, Q. Zhang, Electroactive polymer actuators and sensors, MRS Bulletin 33 (2008) 173–181.

[66] R. H. Baughman, C. Cui, A. A. Zakhidov, Z. Iqbal, J. N. Barisci, G. M. Spinks, G. G. Wallace, A. Mazzoldi, D. De Rossi, A. G. Rinzler, et al., Carbon nanotube actuators, Science 284 (1999) 1340–1344.

[67] L. Shao, J. Biener, H. Jin, M. M. Biener, T. F. Baumann, J. Weissmüller, Electrically tunable nanoporous carbon hybrid actuators, Advanced Functional Materials 22 (2012) 3029–3034.

[68] J. Weissmüller, R. Viswanath, D. Kramer, P. Zimmer, R. Würschum, H. Gleiter, Charge-induced reversible strain in a metal, Science 300 (2003) 312–315.

[69] H. Jin, J. Weissmüller, Bulk nanoporous metal for actuation, Advanced Engineering Materials 12 (2010) 714–723.

[70] M. Mizumoto, T. Ohgai, A. Kagawa, Bending behavior of Cu-plated Pd–Ni alloys ribbon driven by hydrogenation, Journal of Alloys and Compounds 482 (2009) 416–419.

[71] F. Favier, E. C. Walter, M. P. Zach, T. Benter, R. M. Penner, Hydrogen sensors and switches from electrodeposited palladium mesowire arrays, Science 293 (2001) 2227–2231.

[72] H. Peisl, Lattice strains due to hydrogen in metals, in: Hydrogen in Metals I, Springer, 1978, pp. 53–74.

[73] E. Wicke, H. Brodowsky, H. Züchner, Hydrogen in palladium and palladium alloys, in: Hydrogen in Metals II, Springer, 1978, pp. 73–155.

[74] B. Baranowski, S. Majchrzak, T. Flanagan, The volume increase of fcc metals and alloys due to interstitial hydrogen over a wide range of hydrogen contents, Journal of Physics F: Metal Physics 1 (1971) 258.

[75] F. Schoofs, L. Stappers, J. Van Humbeeck, J. Fransaer, Pd–H as an actuator material, Functional Materials Letters 2 (2009) 107–112.

[76] J. Zhang, Y. Wang, C. Si, Q. Bai, W. Ma, H. Gao, Z. Zhang, Electrochemical actuation behaviors of bulk nanoporous palladium in acid and alkaline solutions, Electrochimica Acta 220 (2016) 91–97.

[77] E.-M. Steyskal, C. Wiednig, N. Enzinger, R. Würschum, In situ characterization of hydrogen absorption in nanoporous palladium produced by dealloying, Beilstein Journal of Nanotechnology 7 (2016) 1197.

[78] M. Hakamada, M. Mabuchi, Fabrication of nanoporous palladium by dealloying and its thermal coarsening, Journal of Alloys and Compounds 479 (2009) 326–329.

[79] M. Hakamada, H. Nakano, T. Furukawa, M. Takahashi, M. Mabuchi, Hydrogen storage properties of nanoporous palladium fabricated by dealloying, The Journal of Physical Chemistry C 114 (2009) 868–873.

[80] M. Łukaszewski, K. Klimek, A. Żurowski, T. Kędra, A. Czerwiński, Kinetics and mechanism of hydrogen electrosorption in palladium-based alloys, Solid State Ionics 190 (2011) 18–24.

[81] V. A. Sethuraman, V. Srinivasan, A. F. Bower, P. R. Guduru, In situ measurements of stress-potential coupling in lithiated silicon, Journal of The Electrochemical Society 157 (2010) A1253–A1261.

[82] Z. Cui, F. Gao, J. Qu, A finite deformation stress-dependent chemical potential and its applications to lithium ion batteries, Journal of the Mechanics and Physics of Solids 60 (2012) 1280–1295.

[83] M. Gururajan, A. Lahiri, Elastic stress effects on microstructural instabilities, ArXiv preprint arXiv:1607.00599 (2016).

[84] N. Muralidharan, C. N. Brock, A. P. Cohn, D. Schauben, R. E. Carter, L. Oakes, D. G. Walker, C. L. Pint, Tunable mechanochemistry of lithium battery electrodes, ACS Nano 11 (2017) 6243–6251.

[85] T. Kitzler, E. Maawad, D. M. Többens, M. Ziehmer, J. Markmann, The electro-chemo-mechanical coupling in lithium alloy electrodes and its origins, Journal of The Electrochemical Society 162 (2015) A2684–A2691.

[86] L. A. Kibler, A. M. El-Aziz, R. Hoyer, D. M. Kolb, Tuning reaction rates by lateral strain in a palladium monolayer, Angewandte Chemie International Edition 44 (2005) 2080–2084.

[87] P. Strasser, S. Koh, T. Anniyev, J. Greeley, K. More, C. Yu, Z. Liu, S. Kaya, D. Nordlund, H. Ogasawara, et al., Lattice-strain control of the activity in dealloyed core–shell fuel cell catalysts, Nature Chemistry 2 (2010) 454.

[88] X. Wang, Y. Orikasa, Y. Takesue, H. Inoue, M. Nakamura, T. Minato, N. Hoshi, Y. Uchimoto, Quantitating the lattice strain dependence of monolayer Pt shell activity toward oxygen reduction, Journal of the American Chemical Society 135 (2013) 5938–5941.

[89] Q. Deng, M. Smetanin, J. Weissmüller, Mechanical modulation of reaction rates in electrocatalysis, Journal of Catalysis 309 (2014) 351–361.

[90] R. Viswanath, J. Weissmüller, Electrocapillary coupling coefficients for hydrogen electrosorption on palladium, Acta Materialia 61 (2013) 6301–6309.

[91] S. Morito, H. Tanaka, R. Konishi, T. Furuhara, T. Maki, The morphology and crystallography of lath martensite in Fe-C alloys, Acta Materialia 51 (2003) 1789–1799.

[92] T. Grosdidier, A. Hazotte, A. Simon, Precipitation and dissolution processes in γ/γ' single crystal nickel-based superalloys, Materials Science and Engineering: A 256 (1998) 183–196.

[93] T. M. Pollock, S. Tin, Nickel-based superalloys for advanced turbine engines: chemistry, microstructure and properties, Journal of Propulsion and Power 22 (2006) 361–374.

[94] R. C. Reed, The superalloys: fundamentals and applications, Cambridge university press, 2008.

[95] F. Lewis, J. Magennis, S. McKee, P. Ssebuwufu, Hydrogen chemical potentials and diffusion coefficients in hydrogen diffusion membranes, Nature 306 (1983) 673.

[96] J. Völkl, G. Alefeld, Diffusion of hydrogen in metals, in: Hydrogen in Metals I, Springer, 1978, pp. 321–348.

[97] A. Eshghinejad, Coupled diusion and mechanics in battery electrodes, Ph.D. thesis, University of Washington, 2016.

[98] J. Waisman, G. Sines, L. Robinson, Diffusion of hydrogen in titanium alloys due to composition, temperature, and stress gradients, Metallurgical Transactions 4 (1973) 291–302.

[99] W. Gorsky, Theorie der elastischen Nachwirkung in ungeordneten Mischkristallen (elastische Nachwirkung zweiter Art), Physikalische Zeitschrift der Sowjetunion 8 (1935) 457–471.

[100] O. Hardouin Duparc, A. Krajnikov, Vadim gorsky, a forgotten physics pioneer, Physics Today Online DOI 10.1063/PT.6.4.20170713a (2017) http://physicstoday.scitation.org/do/10.1063/PT.6.4.20170713a/full/.

[101] G. Alefeld, G. Schaumann, J. Tretkowski, J. Völkl, Ferroelasticity of niobium due to hydrogen as a lattice gas, Physical Review Letters 22 (1969) 697.

[102] J. Völkl, The gorsky effect, Berichte der Bunsengesellschaft für Physikalische Chemie 76 (1972) 797–805.

[103] K. Kandasamy, F. Lewis, Important gorsky effect influences on diffusion coefficients in metal–hydrogen systems, International Journal of Hydrogen Energy 24 (1999) 763–769.

[104] F. Larché, J. W. Cahn, A linear theory of thermochemical equilibrium of solids under stress, Acta Metallurgica 21 (1973) 1051–1063.

[105] Y. Mishin, Calculation of open and closed system elastic coefficients for multicomponent solids, Physical Review B 91 (2015) 224107.

[106] P. H. Leo, R. Sekerka, The effect of elastic fields on the morphological stability of a precipitate grown from solid solution, Acta Metallurgica 37 (1989) 3139–3149.

[107] M. Thompson, C. Su, P. Voorhees, The equilibrium shape of a misfitting precipitate, Acta Metallurgica et Materialia 42 (1994) 2107–2122.

[108] P. Fratzl, O. Penrose, J. L. Lebowitz, Modeling of phase separation in alloys with coherent elastic misfit, Journal of Statistical Physics 95 (1999) 1429–1503.

[109] R. Mukherjee, T. Abinandanan, M. Gururajan, Phase field study of precipitate growth: Effect of misfit strain and interface curvature, Acta Materialia 57 (2009) 3947–3954.

[110] M. T. McDowell, S. W. Lee, W. D. Nix, Y. Cui, 25th anniversary article: Understanding the lithiation of silicon and other alloying anodes for lithium-ion batteries, Advanced Materials 25 (2013) 4966–4985.

[111] L. Chen, F. Fan, L. Hong, J. Chen, Y. Ji, S. Zhang, T. Zhu, L. Chen, A phase-field model coupled with large elasto-plastic deformation: application to lithiated silicon electrodes, Journal of The Electrochemical Society 161 (2014) F3164–F3172.

[112] J. W. Cahn, Thermodynamic aspects of cottrell atmospheres, Philosophical Magazine 93 (2013) 3741–3746.

[113] J. P. Hirth, On definitions and assumptions in the dislocation theory for solid solutions, Philosophical Magazine 94 (2014) 3162–3169.

[114] J. P. Hirth, Response to comments, Philosophical Magazine 94 (2014) 3177–3182.

[115] J. P. Hirth, D. M. Barnett, R. G. Hoagland, Solute atmospheres at dislocations, Acta Materialia 131 (2017) 574–593.

[116] Y. Ding, Y.-J. Kim, J. Erlebacher, Nanoporous gold leaf:"ancient technology"/advanced material, Advanced Materials 16 (2004) 1897–1900.

[117] G. Tammann, Zum Gedächtnis der Entdeckung des Isomorphismus vor 100 Jahren. Die chemischen und galvanischen Eigenschaften von Mischkristallreihen und ihre Atomverteilung, Zeitschrift für Anorganische und Allgemeine Chemie 107 (1919) 1–239.

[118] K. Sieradzki, J. Kim, A. Cole, R. Newman, The relationship between dealloying and transgranular stress-corrosion cracking of Cu-Zn and Cu-Al alloys, Journal of The Electrochemical Society 134 (1987) 1635–1639.

[119] D. Artymowicz, J. Erlebacher, R. Newman, Relationship between the parting limit for de-alloying and a particular geometric high-density site percolation threshold, Philosophical Magazine 89 (2009) 1663–1693.

[120] Z. Qi, Bulk nested-network nanoporous gold via dealloying, Dissertation thesis, Technische Universität Hamburg, 2015.

[121] K. Sieradzki, N. Dimitrov, D. Movrin, C. McCall, N. Vasiljevic, J. Erlebacher, The dealloying critical potential, Journal of the Electrochemical Society 149 (2002) B370–B377.

[122] K. Sieradzki, Curvature effects in alloy dissolution, Journal of The Electrochemical Society 140 (1993) 2868–2872.

[123] R. B. Abrams, The dezincification of brass, Transactions of the American Electrochemical Society 42 (1922) 39–54.

[124] H. Pickering, C. Wagner, Electrolytic dissolution of binary alloys containing a noble metal, Journal of the Electrochemical Society 114 (1967) 698–706.

[125] A. Forty, P. Durkin, A micromorphological study of the dissolution of silver-gold alloys in nitric acid, Philosophical Magazine A 42 (1980) 295–318.

[126] A. Forty, G. Rowlands, A possible model for corrosion pitting and tunneling in noble-metal alloys, Philosophical Magazine A 43 (1981) 171–188.

[127] I. McCue, E. Benn, B. Gaskey, J. Erlebacher, Dealloying and dealloyed materials, Annual Review of Materials Research 46 (2016) 263–286.

[128] G. D. Bengough, R. May, Seventh report to the corrosion research committee of the institute of metals, The Journal of the Institute of Metals 32 (1924) 81.

[129] F. Larché, J. W. Cahn, Overview no. 41 the interactions of composition and stress in crystalline solids, Acta Metallurgica 33 (1985) 331–357.

[130] T. B. Massalski, H. Okamoto, P. Subramanian, L. Kacprzak, Binary alloy phase diagrams. vol. 3, ASM International, Materials Park, Ohio (1990) 1485.

[131] Q. Xu, Nanoporous materials: synthesis and applications, CRC Press, 2013.

[132] E. Detsi, M. Van De Schootbrugge, S. Punzhin, P. Onck, J. De Hosson, On tuning the morphology of nanoporous gold, Scripta Materialia 64 (2011) 319–322.

[133] B. Beverskog, I. Puigdomenech, Revised pourbaix diagrams for copper at 25 to 300 C, Journal of The Electrochemical Society 144 (1997) 3476–3483.

[134] C. Xu, A. Liu, H. Qiu, Y. Liu, Nanoporous PdCu alloy with enhanced electrocatalytic performance, Electrochemistry Communications 13 (2011) 766–769.

[135] A. Liu, H. Geng, C. Xu, H. Qiu, A three-dimensional hierarchical nanoporous PdCu alloy for enhanced electrocatalysis and biosensing, Analytica Chimica Acta 703 (2011) 172–178.

[136] C. Xu, Y. Liu, J. Wang, H. Geng, H. Qiu, Nanoporous PdCu alloy for formic acid electro-oxidation, Journal of Power Sources 199 (2012) 124–131.

[137] L. Liu, H. Jin, Scaling equation for the elastic modulus of nanoporous gold with "fixed" network connectivity, Applied Physics Letters 110 (2017) 211902.

[138] S. Trasatti, O. Petrii, Real surface area measurements in electrochemistry, Pure and Applied Chemistry 63 (1991) 711–734.

[139] B. Rezaei, E. Havakeshian, A. A. Ensafi, Fabrication of a porous Pd film on nanoporous stainless steel using galvanic replacement as a novel electrocatalyst/electrode design for glycerol oxidation, Electrochimica Acta 136 (2014) 89–96.

[140] M. Łukaszewski, M. Grdeń, A. Czerwiński, Hydrogen electrosorption in Pd–Pt–Rh alloys, Journal of Electroanalytical Chemistry 573 (2004) 87–98.

[141] H. Brodowsky, E. Poeschel, Wasserstoff in palladium/silber-legierungen, Zeitschrift für Physikalische Chemie 44 (1965) 143–159.

[142] Y. Sakamoto, N. Ishimaru, Y. Mukai, Thermodynamics of solution of hydrogen in Pd-Cu and Pd-Cu-Au solid solution alloys, Berichte der Bunsengesellschaft für Physikalische Chemie 95 (1991) 680–688.

[143] W. Huang, S. M. Opalka, D. Wang, T. B. Flanagan, Thermodynamic modelling of the Cu–Pd–H system, Calphad 31 (2007) 315–329.

[144] T. B. Flanagan, D. Wang, S. Luo, Thermodynamics of H in disordered Pd-Ag alloys from calorimetric and equilibrium pressure-composition-temperature measurements, The Journal of Physical Chemistry B 111 (2007) 10723–10735.

[145] S. Luo, D. Wang, T. B. Flanagan, Thermodynamics of hydrogen in fcc Pd-Au alloys, The Journal of Physical Chemistry B 114 (2010) 6117–6125.

[146] C. Soyarslan, S. Bargmann, M. Pradas, J. Weissmüller, 3D stochastic bicontinuous microstructures: Generation, topology and elasticity, Acta Materialia 149 (2018) 326–340.

[147] E. Brandes, G. Brook, Smithells Metals Reference Book, Elsevier, Butterworth-Heinemann, Oxford, 2013.

[148] P. Subramanian, D. Laughlin, Cu-Pd (copper-palladium), Journal of Phase Equilibria 12 (1991) 231–243.

[149] G. N. Ankah, A. Pareek, S. Cherevko, A. A. Topalov, M. Rohwerder, F. U. Renner, The influence of halides on the initial selective dissolution of Cu_3Au (111), Electrochimica Acta 85 (2012) 384–392.

[150] X. Ye, N. Lu, X. Li, K. Du, J. Tan, H. Jin, Primary and secondary dealloying of Au (Pt)-Ag: structural and compositional evolutions, and volume shrinkage, Journal of The Electrochemical Society 161 (2014) C517–C526.

[151] S. Kuwano-Nakatani, T. Fujita, K. Uchisawa, D. Umetsu, Y. Kase, Y. Kowata, K. Chiba, T. Tokunaga, S. Arai, Y. Yamamoto, et al., Environment-sensitive thermal coarsening of nanoporous gold, Materials Transactions 56 (2015) 468–472.

[152] A. Kosinova, D. Wang, P. Schaaf, O. Kovalenko, L. Klinger, E. Rabkin, Fabrication of hollow gold nanoparticles by dewetting, dealloying and coarsening, Acta Materialia 102 (2016) 108–115.

[153] P. Nsimama, Morphological and structural properties of silver nanofilms annealed by RTP in different atmospheres, American Journal of Nano Research and Applications 3 (2015) 99–104.

[154] C. Herring, Effect of change of scale on sintering phenomena, Journal of Applied Physics 21 (1950) 301–303.

[155] Y. K. Chen-Wiegart, S. Wang, Y. S. Chu, W. Liu, I. McNulty, P. W. Voorhees, D. C. Dunand, Structural evolution of nanoporous gold during thermal coarsening, Acta Materialia 60 (2012) 4972–4981.

[156] S. Kuwano-Nakatani, T. Fujita, K. Uchisawa, D. Umetsu, Y. Kase, Y. Kowata, K. Chiba, T. Tokunaga, S. Arai, Y. Yamamoto, N. Tanaka, M. W. Chen, Environment-sensitive thermal coarsening of nanoporous gold, Materials Transactions 56 (2015) 468–472.

[157] I. McCue, J. Stuckner, M. Murayama, M. J. Demkowicz, Gaining new insights into nanoporous gold by mining and analysis of published images, Scientific Reports 8 (2018) 6761.

[158] M. Baldauf, D. Kolb, A hydrogen adsorption and absorption study with ultrathin Pd overlayers on Au (111) and Au (100), Electrochimica Acta 38 (1993) 2145–2153.

[159] S. Stankovich, D. A. Dikin, R. D. Piner, K. A. Kohlhaas, A. Kleinhammes, Y. Jia, Y. Wu, S. T. Nguyen, R. S. Ruoff, Synthesis of graphene-based nanosheets via chemical reduction of exfoliated graphite oxide, Carbon 45 (2007) 1558–1565.

[160] H. Duncan, A. Lasia, Mechanism of hydrogen adsorption/absorption at thin Pd layers on Au (1 1 1), Electrochimica Acta 52 (2007) 6195–6205.

[161] H. Duncan, A. Lasia, Separation of hydrogen adsorption and absorption on Pd thin films, Electrochimica Acta 53 (2008) 6845–6850.

[162] T. B. Flanagan, S. Luo, J. D. Clewley, Calorimetric enthalpies for the reaction of H_2 with PdCu alloys at 303 k, Journal of Alloys and Compounds 356 (2003) 13–16.

[163] R. Burch, R. Buss, Pressure-composition isotherms in the palladium-copper-hydrogen system, Solid State Communications 15 (1974) 407–409.

[164] R. Burch, R. Buss, Absorption of hydrogen by palladium–copper alloys. part 1.-experimental measurements, Journal of the Chemical Society, Faraday Transactions 1: Physical Chemistry in Condensed Phases 71 (1975) 913–921.

[165] T. Mütschele, R. Kirchheim, Segregation and diffusion of hydrogen in grain boundaries of palladium, Scripta Metallurgica 21 (1987) 135–140.

[166] J. Weissmüller, C. Lemier, Lattice constants of solid solution microstructures: the case of nanocrystalline Pd-H, Physical Review Letters 82 (1999) 213.

[167] J. Weissmüller, C. Lemier, On the size dependence of the critical point of nanoscale interstitial solid solutions, Philosophical Magazine Letters 80 (2000) 411–418.

[168] C. Lemier, J. Weissmüller, Grain boundary segregation, stress and stretch: Effects on hydrogen absorption in nanocrystalline palladium, Acta Materialia 55 (2007) 1241–1254.

[169] T. Kuji, Y. Matsumura, H. Uchida, T. Aizawa, Hydrogen absorption of nanocrystalline palladium, Journal of Alloys and Compounds 330 (2002) 718–722.

[170] M. Yamauchi, R. Ikeda, H. Kitagawa, M. Takata, Nanosize effects on hydrogen storage in palladium, The Journal of Physical Chemistry C 112 (2008) 3294–3299.

[171] A. Baldi, T. C. Narayan, A. L. Koh, J. A. Dionne, In situ detection of hydrogen-induced phase transitions in individual palladium nanocrystals, Nature Materials 13 (2014) 1143.

[172] J. Cizek, I. Prochazka, M. Vlach, N. Zaludova, P. Dobron, F. Chmelik, G. Brauer, W. Anwand, A. Mücklich, E. Nikitin, et al., Multi-scale analysis of hydrogen-induced buckling in Pd films, Procedia Engineering 1 (2009) 99–103.

[173] J. Čížek, M. Vlček, F. Lukáč, M. Vlach, I. Procházka, G. Brauer, W. Anwand, A. Mücklich, S. Wagner, H. Uchida, et al., Structural studies of nanocrystalline thin Pd films electrochemically doped with hydrogen, in: Defect and Diffusion Forum, volume 331, Trans Tech Publ, 2012, pp. 137–147.

[174] T. Yamazaki, M. Sato, S. Itoh, Discovery of spontaneous deformation of Pd metal during hydrogen absorption/desorption cycles, Proceedings of the Japan Academy. Series B, Physical and Biological Sciences 85 (2009) 183.

[175] J. Völkl, G. Wollenweber, K.-H. Klatt, G. Alefeld, Notizen: Reversed isotope dependence for hydrogen diffusion in palladium, Zeitschrift für Naturforschung A 26 (1971) 922–923.

[176] A. B. Duso, D. D. Chen, Proton and hydroxide ion mobility in capillary electrophoresis, Analytical chemistry 74 (2002) 2938–2942.

[177] A. Migliori, J. Sarrao, W. Visscher, T. Bell, M. Lei, Z. Fisk, R. Leisure, Resonant ultrasound spectroscopic techniques for measurement of the elastic moduli of solids, Physica B: Condensed Matter 183 (1993) 1–24.

[178] A. Fabre, E. Finot, J. Demoment, S. Contreras, Monitoring the chemical changes in Pd induced by hydrogen absorption using microcantilevers, Ultramicroscopy 97 (2003) 425–432.

[179] R. Schwarz, H. Bach, U. Harms, D. Tuggle, Elastic properties of Pd–hydrogen, Pd–deuterium, and Pd–tritium single crystals, Acta Materialia 53 (2005) 569–580.

[180] K. Salama, C. Ko, Effect of hydrogen on the temperature dependence of the elastic constants of palladium single crystals, Journal of Applied Physics 51 (1980) 6202–6209.

Publications & Conferences

Publications

1. S Shi, J Markmann, J Weissmüller*. Verifying Larché–Cahn elasticity, a milestone of 20th-century thermodynamics, *Proceedings of the National Academy of Sciences* , 2018, 115 (43) 10914-10919.

2. S Shi*, J Markmann, J Weissmüller. Synthesis of uniform bulk nanoporous palladium with tunable structure, *Electrochimica Acta*, 2018, 285: 60-69.

3. S Shi*, J Markmann, J Weissmüller. Actuation by hydrogen electrosorption in hierarchical nanoporous palladium, *Philosophical Magazine*, 2017, 97(19): 1571-1587.

Conference contributions

1. S Shi, J Markmann, and J Weissmüller. Verifying Larché–Cahn theory by measuring open-system elasticity of nanoporous palladium(-gold)-hydrogen, 3nd International Symposium on Nanoporous Materials by Alloy Corrosion, 24-28 February 2019, Philadelphia, PA, USA. (*Oral presentation and Poster*)

2. S Shi, J Markmann, and J Weissmüller. Uniform nanoporous Pd by dealloying-synthesis and hydrogen driven actuation performance, Chinese Materials Conference, 12-16 July 2018, Xiamen, China. (*Invited talk*)

3. S Shi, J Markmann, and J Weissmüller. Tunable elasticity of nanoporous palladium by hydrogen insertion, DPG Spring Meeting (German Physical Society), 11-16 March 2018, Berlin, Germany. (*Oral presentation*)

4. S Shi, J Markmann, and J Weissmüller. Uniform hierarchical nanoporous Pd by dealloying-synthesis and hydrogen driven actuation performance, The 68th Annual Meeting of the International Society of Electrochemistry, 27 August-01 September 2017, Providence, RI, USA. (*Oral presentation*)

5. S Shi, J Markmann, and J Weissmüller. Size effects on hydrogen electrosorption in nanoporous Pd-Cu alloys, DPG Spring Meeting (German Physical Society), 19-24 March 2017, Dresden, Germany. (*Oral presentation*)

6. S Shi, J Markmann, and J Weissmüller. Hydrogen induced actuation in nanoporous palladium, 2nd International Symposium on Nanoporous Materials by Alloy Corrosion, 23-27 September 2016, Lake Bostal, Germany. (*Invited talk*)

7. S Shi, J Markmann, and J Weissmüller. Hydrogen-assisted actuation with nanoporous palladium, DPG Spring Meeting (German Physical Society), 06-11 March 2016, Regensburg, Germany. (*Oral presentation*)

8. S Shi, T Kitzler, Q Deng, J Markmann, and J Weissmüller. Potential-strain coupling during hydrogen electrosorption, DPG Spring Meeting (German Physical Society), 15-20 March 2015, Berlin, Germany. (*Poster*)